DEUTSCHES ELEKTRONEN-SYNCHROTRON DESY

DESY 87-175
December 1987

TWO-PHOTON PHYSICS

by

H. Kolanoski

Institut für Physik, Universität Dortmund

P. Zerwas

Institut für Theoretische Physik, RWTH Aachen

ISSN 0418-9833

NOTKESTRASSE 85 · 2 HAMBURG 52

To be sure that your preprints are promptly included in the
HIGH ENERGY PHYSICS INDEX ,
send them to the following address (if possible by air mail) :

DESY
Bibliothek
Notkestrasse 85
2 Hamburg 52
Germany

DESY 87-175
December 1987

ISSN 0418-9833

Two-Photon Physics

Hermann Kolanoski*
Institut für Physik, Universität Dortmund, Germany
and
Peter Zerwas*
Institut für Theoretische Physik, RWTH Aachen, Germany

Contents

*Work supported by the Bundesministerium für Forschung und Technologie

1 Introduction

Electron-positron storage rings offer an excellent opportunity to study photon-photon reactions in collisions of the photon clouds surrounding the beam particles. With the high energies available at PETRA and PEP two-photon processes became measurable in a large kinematical range, and the experimental results cover a wide spectrum of physical problems.

Two-photon physics is intimately related to the development of quantum chromodynamics:

(i) The $\gamma\gamma$ decay width of the neutral pion can only be reconciled with the quark picture if quarks are endowed with 3 color degrees of freedom [1].

(ii) The asymptotic form of the photon structure function [2,3] can be calculated in perturbative QCD [4]. In leading order the structure function rises uniformly in $\log Q^2$ (Q^2 being the momentum transfer), a direct consequence of asymptotic freedom. Under mild assumptions on the removal of spurious singularities [5], the scale parameter Λ can be extracted from the absolute value of the structure function if next-to-leading order contributions [6] are properly taken into account.

(iii) In the non-perturbative region, the magnitude of the $\gamma\gamma$ decay width depends crucially on the physical nature of resonances. Small widths are plausibly expected for gluonium resonances, containing no charged constituents to which the photons could couple, such as the glueball candidate $\eta(1440)$ [formerly $\iota(1460)$]. Small widths of the $a_0(980)$ and $f_0(975)$ [formerly δ^0 and S^*] favor the interpretation of these states as novel four-quark resonances [7] or pseudoscalar-pseudoscalar molecules [8]. Bound states of vector meson pairs on the other hand would have a large $\gamma\gamma$ decay width [9,10]. The observation of exotic states could indicate the formation of mixed quark-gluon hybrid resonances.

(iv) Exclusive hadron-pair production at large angles in $\gamma\gamma$ collisions is a result of the interplay between perturbative short-distance and nonperturbative large-distance QCD mechanisms [11]. The twin-nature of these processes renders the measurements an important test of a highly nontrivial algorithmic concept in QCD.

(v) Many other QCD phenomena have been investigated in recent years. First of all, the transition region between long and short-range properties of QCD is illuminated by the development of jets at large transverse momenta [12], revealing the detailed distribution of quark and gluon quanta in the femto-universe. The total cross section $\gamma\gamma \to hadrons$ is a fundamental quantity of soft hadron physics [13].

Other problems have largely been pushed into the shade by the dominating role QCD has played in high energy two-photon physics. A cut-off parameter of order

10^{-15} cm, derived from (g-2) measurements using a 6th order QED calculation, and a similiar value from direct e^+e^- annihilation, did not leave much room to carry out novel QED tests in $\gamma\gamma$ scattering. The search for fundamental scalar particles in $\gamma\gamma$ collisions, on the other hand, is of utmost general physical importance [14, 15], because they cannot be produced directly in e^+e^- collisions if they couple to fermions with a strength set by the fermion mass.

Excellent reviews have been published on $\gamma\gamma$ physics in the past years [16]. These articles provide a comprehensive survey of the very involved and rather difficult techniques, both experimental and theoretical, that have been developed to extract information on the underlying fundamental issues. These details need therefore not be repeated in the present context. But rather an attempt has been made to focus on those points in which $\gamma\gamma$ physics has contributed to the development of QCD as the microscopic theory of strong interactions.

1.1 Kinematics and Cross Sections

The proper instruments to study $\gamma\gamma$ collisions experimentally are high energy e^+e^- colliders. High energy electrons can split off photons with a lifetime of order $\tau \sim \frac{E}{m_e} \cdot p_T^{-1}$ where E is the beam energy and p_T is the γ transverse momentum relative to the beam direction (Fig.1). Time dilation renders this lifetime much longer than typical reaction times of order 10^{-23} sec so that the photons can well be treated as real particles in a scattering process. The spectrum of these photons has the familiar Weizsäcker-Williams form in the leading log approximation:

$$\frac{dN}{d\omega} = \frac{\alpha}{2\pi}\frac{1+(1-\omega)^2}{\omega}\eta. \tag{1}$$

ω is the fractional photon energy $\omega = E_\gamma/E$ and η depends on whether the photons are tagged by detecting the electrons in an angular range $\vartheta_{min} \le \vartheta \le \vartheta_{max}$ or not:

$$\eta = \begin{cases} \log(\frac{E^2}{m_e^2}) & \text{untagged} \\ \log(\frac{\vartheta_{max}}{\vartheta_{min}})^2 & \text{tagged} \end{cases} \tag{2}$$

At PETRA/PEP energies this logarithmic enhancement factor can increase up to a value of 20, compensating partly the suppression due to higher orders in α. For a given invariant mass $W_{\gamma\gamma}$, the $\gamma\gamma$ luminosity in an e^+e^- collider depends on the energy fraction $z = W_{\gamma\gamma}/\sqrt{s}$ of the total e^+e^- energy $\sqrt{s} = 2E$:

$$\begin{aligned} \frac{dL}{dz} &= (\frac{\alpha}{\pi})^2 \frac{f(z)}{z}\eta^2 \\ f(z) &= (2+z^2)^2 \log\frac{1}{z} - (1-z^2)(3+z^2). \end{aligned} \tag{3}$$

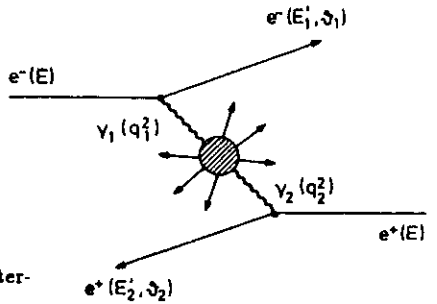

Figure 1: $\gamma\gamma$ collisions in e^+e^- scattering.

This approximate formula, derived by Low [17,18], overestimates the exact luminosity function (Fig.2) by about 10 to 20% for $z \leq 0.8$, but reproduces the shape of the function quite well. The measured e^+e^- cross section is found by folding the $\gamma\gamma$ cross section $\sigma(\gamma\gamma \to X)$ with the $\gamma\gamma$ luminosity,

$$\sigma(e^+e^- \to e^+e^-X) = (\frac{\alpha}{\pi})^2\eta^2 \int_0^1 dz \frac{f(z)}{z}\sigma(\gamma\gamma \to X; W_{\gamma\gamma} = z\sqrt{s}). \qquad (4)$$

Since Weizsäcker-Williams photons are emitted at small angles $\sim d\vartheta/\vartheta$, the $\gamma\gamma$ c.m. system moves approximately parallel to the beam pipe with a momentum $(\omega_1 - \omega_2)\vec{E}$. The luminosity function peaks at small c.m. energies $W_{\gamma\gamma}$. The c.m. motion of the event in the laboratory and the preferentially low energy of the visible final state X render $\gamma\gamma$ events characteristically different from e^+e^- annihilation events. The scale of the $\gamma\gamma$ annihilation cross section is set by the c.m. energy of X, $\sigma(\gamma\gamma \to X) \sim \alpha^2/m_X^2$. For small invariant masses, say $m_X \sim 2m_e$, the cross section $\sigma(e^+e^- \to e^+e^- X)$ can readily become 6 orders of magnitude larger than the annihilation cross section. However, these events remain hidden in the beam pipe. For $\gamma\gamma$ events with an energy $m_X \geq O(10^{-1})\sqrt{s}$ outside a fixed-angle cone around the lepton beams, the ratio of the $\gamma\gamma$ cross section to the annihilation cross section is again reduced to a value smaller than $O(1)$.

If electrons and positrons are detected at large momentum transfer the lifetime of the photons becomes so short that they cannot be treated as on-shell particles anymore, and the cross section cannot be factorized into a single $\gamma\gamma$ cross section and the $\gamma\gamma$ luminosity factor. Instead one has to sum over all transverse (T) and longitudinal (L) photon helicities, weighted with the appropriate spin-density matrix elements:

$$\sigma \propto 4\rho_1^{++}\rho_2^{++}\sigma_{TT} + 2\rho_1^{00}\rho_2^{++}\sigma_{LT} + 2\rho_1^{++}\rho_2^{00}\sigma_{TL} + \rho_1^{00}\rho_2^{00}\sigma_{LL} + 2|\rho_1^{+-}\rho_2^{+-}|\tau_{TT}\cos 2\varphi - 8|\rho_1^{+0}\rho_2^{+0}|\tau_{TL}\cos\varphi. \qquad (5)$$

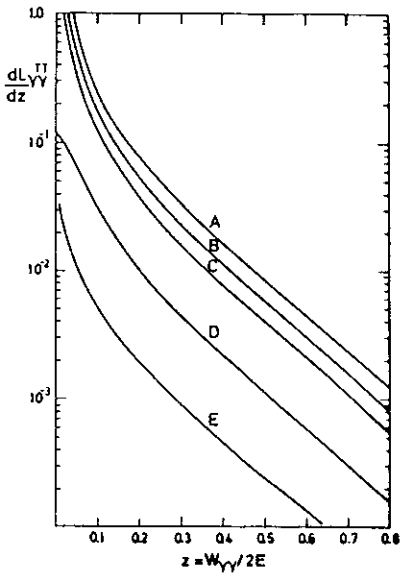

Figure 2: Differential two-photon luminosity for transverse photons [19]: Curves A, B, C give the total luminosity for E = 1000, 100, 15 GeV; curves D and E the single and double tagged luminosity for E = 15 GeV (tagging angles: $0 \leq \varphi \leq 2\pi, 20 < \vartheta < 200$ mrad).

The spin-density matrix elements ρ_i are recorded in [20,21] and φ denotes the azimuthal angle between the electron and positron scattering planes in the photon-photon center-of-mass system. The helicity cross sections and asymmetries depend on the $\gamma\gamma$ c.m. energy $W_{\gamma\gamma}$ and the photon masses: $\sigma_i(W_{\gamma\gamma}, q_1^2, q_2^2)$. In the limit $q_i^2 \to 0$, the corresponding longitudinal cross sections and asymmetries vanish and the horrible formula (5) simplifies considerably. The reaction is then interpreted as $e\gamma \to eX$ scattering that will be described in great detail in section 4. Folding the $e\gamma$ cross section with the Weizsäcker- Williams spectrum (1) gives the related e^+e^- cross section.

1.2 Experimental Techniques in Two-Photon Physics

Two-photon scattering processes have been investigated at almost all e^+e^- storage rings. Usually the same detectors are employed as for the detection of one-photon annihilation events. In most cases the only devices specific to two-photon physics are the 'tagging detectors' covering the forward regions for the detection of the scattered leptons.

There are two characteristic features of two-photon reactions which render their detection in general more difficult than the detection of one-photon reactions:

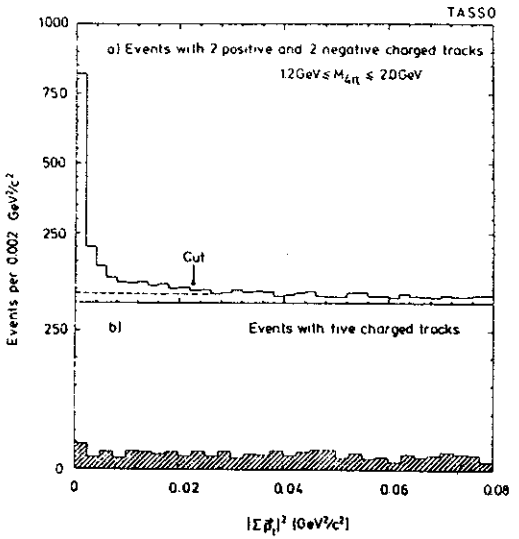

Figure 3: Distribution of the squared transverse momentum of a detected particle system: a) events with four charged particles and total charge zero; b) events with five charged particles detected, i.e. at least one particle is missing.

- Since the $\gamma\gamma$ -luminosity function (3) peaks at small $W_{\gamma\gamma}$ the final states have preferentially low multiplicities and low momenta. This makes triggering particularly in a high-energy environment quite problematic.

- The $\gamma\gamma$ system is preferentially boosted along the beam direction leading to high particle densities close to the beam where all detectors have acceptance holes.

Thus most important for two-photon physics is the capability of the detector to trigger on low multiplicities with low thresholds and to cover tightly the region around the beams. The latter requirement can best be fulfilled with specific forward spectrometers [22] as they are used by the dedicated two-photon experiments PLUTO (as installed at PETRA in 1981-82) [23] and PEP-9 which runs together with the TPC detector at PEP [24].

Tagging: Tagging of the photons is achieved by measuring energy and direction of the scattered leptons in, usually specialized, forward detectors. Typical 'small angle taggers' cover an angular range between about 20 and 100 mrad. In few cases experiments have tagging capabilities down to 0° [25,26,27], allowing to tag quasi-real photons. For tagging large-Q^2 photons a rather continuous coverage up

to the region of the central detector is desirable (as realized, e.g., in the PLUTO detector [23]).

However, if possible, tagging is avoided since the rates are reduced in this mode. In the notag mode completely reconstructed events can be selected by requiring that the total transverse momentum of the observed particles is small (see Fig.3). This method makes use of the fact that the photons are preferentially emitted with small transverse momenta.

In some cases tagging is needed, e.g., if a kinematical reconstruction is required or if background can otherwise not be suppressed. An important example is the application of the single-tag method for the measurement of the photon structure functions. In this case the tag provides the Q^2 value of the virtual photon which probes the structure of the 'target photon'. The Q^2 resolution is typically around 10%, adequate for most applications. It turns out to be much harder to achieve an adequate $W_{\gamma\gamma}$ resolution from the standard tagging devices. This problem and the reduced rates are the reasons why double-tag experiments, which in principle deliver the complete $\gamma\gamma$ kinematics, have not played as important a role as might have been expected. In most cases $W_{\gamma\gamma}$ is determined from the measured final state. Since for inclusive measurements the final state is usually incompletely detected an unfolding procedure is necessary to relate the measured invariant mass to the true $W_{\gamma\gamma}$.

2 Two-Photon Coupling of Meson Resonances

2.1 Introduction

Two-photon couplings of C-even mesons can be studied in photon-photon scattering reactions. Since photons are not directly involved in strong interactions they are well suited to explore the structure of hadrons and the properties of their basic constituents. The knowledge of the internal structure of hadrons proved to be intimately related to the progress made in our understanding of quantum chromodynamics as the fundamental theory of strong interactions. This relationship can be illuminated by four major issues in $\gamma\gamma$ physics:

- The measured two-photon width of the π^0 can theoretically only be explained if quarks come in three colors, otherwise the quark model fails by almost an order of magnitude ($\sim N_C^2 = 9$). This is one of the most direct arguments for the color degrees of freedom of quarks besides the solution of the statistics puzzle in baryon states and the size of the hadron production cross section in e^+e^- annihilation.

- QCD predicts the existence of bound gluon states, the glueballs. Such states have not yet been firmly established. An important signature for these states should be their small $\gamma\gamma$ coupling since they do not contain charged constituents. Thus comparing two-photon production of mesons with their production in gluon-gluon reactions, such as radiative J/ψ decays, allows to single out glueball candidates.

- Deficiencies in our understanding of the large distance behavior of QCD did not yet allow to prove or disprove the existence of four-quark states. Two-photon physics offers valuable experimental input for the solution of this question. For example, large $\gamma\gamma$ couplings are expected for those four-quark states which can be decomposed into $(q\bar{q})$ vector meson compounds. If in other cases these compounds are pseudoscalars, as suggested in the case of the $f_0(975)$ and the $a_0(980)$, a rather small $\gamma\gamma$ width should help discriminate $qq\bar{q}\bar{q}$ states against ordinary $q\bar{q}$ states.

- Finally, the $\gamma\gamma$ widths of heavy quark systems allow testing QCD potential models.

This list might be extended by a variety of contributions of $\gamma\gamma$ physics to the light quark spectroscopy, such as establishing the singlet-octet mixing for the pseudoscalar and tensor mesons. That a similar understanding cannot be reported for the scalar mesons may have deeper reasons that two-photon physics can help to find out.

Only resonances with spin-parity quantum numbers $J^P = 0^{\pm}, 2^{\pm}, 3^+, 4^{\pm}, 5^+, \ldots$ can couple to two real photons. Spin 1 mesons do not couple to $\gamma\gamma$ (Yang's theorem [28]). Thus the coupling to two real photons is allowed for all S and P wave $q\bar{q}$ states with even charge conjugation except for the $J^{PC} = 1^{++}$ axial vector states.

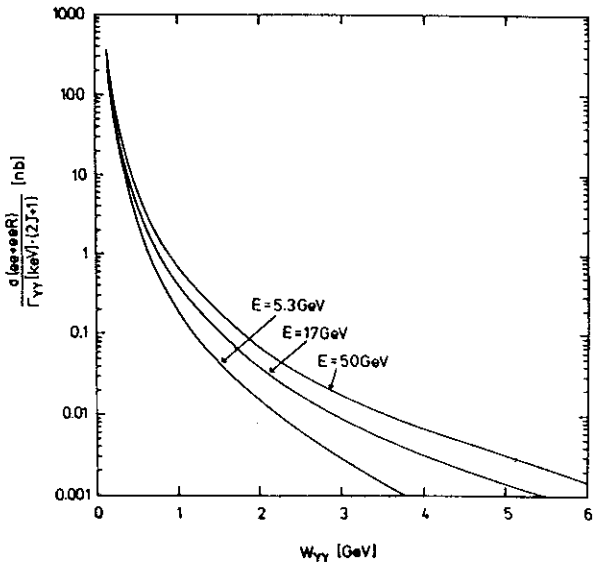

Figure 4: The e^+e^- cross section for the production of a resonance via the two-photon process (normalized to $\Gamma_{\gamma\gamma} = 1\ keV$).

2.2 Measuring Two-Photon Couplings

The $\gamma\gamma$ width of a particle can be directly measured by observing its formation in two-photon scattering reactions. The cross section for the two-photon production of a state R with spin J is given by

$$\sigma(\gamma\gamma \to R) = 8\pi(2J+1)\frac{\Gamma\Gamma_{\gamma\gamma}}{(W_{\gamma\gamma}^2 - M_R^2)^2 + \Gamma^2 M_R^2} \qquad (6)$$

where M_R is the mass, Γ the total width, and $\Gamma_{\gamma\gamma}$ the $\gamma\gamma$ width of the resonance.

At e^+e^- storage rings a C-even particle R is formed in the two-photon exchange reaction (F. Low [17]):

$$e^+e^- \to e^+e^-R. \qquad (7)$$

With the restriction to quasi-real photons the photon flux, which connects the observed rate with the two-photon cross section, can be exactly calculated in QED, see e.g. [20,21]. The restriction to quasi-real photons is sufficiently well fulfilled by using the no-tag method and requiring small transverse momenta of the two-photon system with respect to the beam direction (see Fig.3). Including also virtual photons the description of reaction (7) becomes in general very complicated.

Due to the longitudinal component of virtual photons additional cross section terms (see (5)) may arise, not connected to the $\gamma\gamma$ width by a smooth form factor behavior. This general case is discussed in detail in [29].

For quasi-real photons, the flux is calculated by including only transverse photons [20,21]. The equivalent photon approximation is conveniently used to estimate the production rate of a resonance R in the process (7) [17]:

$$\sigma(e^+e^- \to e^+e^-R) \approx 16\alpha^2 \left(log\frac{E}{m_e}\right)^2 f\left(\frac{M_R}{2E}\right) \frac{(2J+1)\Gamma_{\gamma\gamma}}{M_R^3} \qquad (8)$$

where f was given in (3).

Fig.4 shows the expected cross section for 5, 17 and 50 GeV beam energies. The cross section rises logarithmically with the beam energy. On the other hand the detection efficiencies decrease at higher beam energies because the boosts of the $\gamma\gamma$ system are on average larger, so that in practice the observed rates are not so different in the resonance region.

2.3 The Pseudoscalar Mesons

The π^0 meson

As already alluded to before, the theoretical interpretation of the $\gamma\gamma$ width of the π^0 meson is a key point for the foundation of quantum chromodynamics and has thus played a central role in the development of elementary particle physics. Applying current algebra techniques in the calculation of the $\pi^0\gamma\gamma$ coupling, the amplitude is entirely given by the Adler-Bell-Jackiw axial vector anomaly [30] in the limit of vanishing pion mass. This anomaly, being a short distance effect, can be computed from the triangular quark loop shown in Fig.5. Because the π^0 lifetime is connected

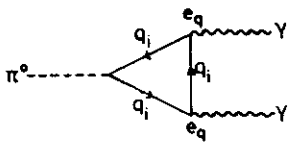

Figure 5: The triangle diagram describing the two-photon decay of the π^0.

to the behavior of the theory at short distances, it is not affected by unknown non-perturbative properties of the π^0 (which are globally summarized in the well measured π_{l_2} decay constant f_π= 95 MeV). The theoretical calculation is thus rigorous up to small PCAC corrections which generally stay below the 10% level. The connection to short-distance physics makes the π^0 lifetime therefore a valuable instrument to probe fundamental aspects of the quark theory.

Expressing the width in terms of the $\pi\gamma\gamma$ coupling constant $g_{\pi\gamma\gamma}$

$$\Gamma_{\pi\gamma\gamma} = \frac{m_\pi^3}{64\pi} g_{\pi\gamma\gamma}^2 \qquad (9)$$

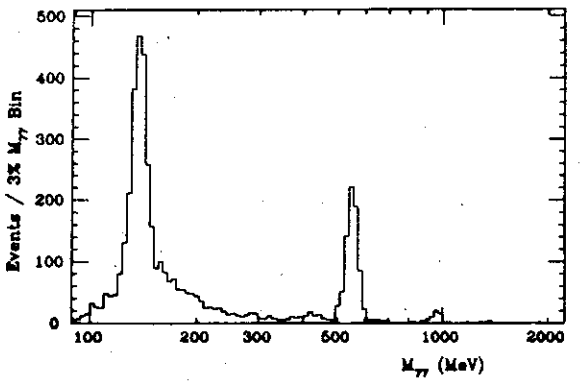

Figure 6: The spectrum of invariant $\gamma\gamma$ masses obtained with the Crystal Ball detector [34].

the axial vector anomaly yields the following expression for $g_{\pi\gamma\gamma}$

$$g_{\pi\gamma\gamma} = \frac{\alpha\sqrt{2}}{\pi f_\pi} N_c < e_q^2 >_\pi \qquad (10)$$

with

$$< e_q^2 >_\pi = \frac{1}{\sqrt{2}}(e_d^2 - e_u^2) = -\frac{1}{3\sqrt{2}}.$$

N_c is the number of different quark colors contributing to the anomaly as apparent from Fig.5. For N_c=3 the theoretical value of the $\gamma\gamma$ width of the π^0 turns out to be [30,31]

$$\Gamma_{\pi^0\gamma\gamma}^{theor.} = 7.7 \text{ eV} \qquad (11)$$

This value would be 9 times smaller if the quarks did not carry color charges. Comparing (11) with the experimental value [32]

$$\Gamma_{\pi^0\gamma\gamma} = (7.48 \pm 0.33 \pm 0.31) \text{ eV} \qquad (12)$$

it is obvious that quarks must be endowed with 3 color degrees of freedom.

The $\gamma\gamma$ width of the π^0 was first determined using the Primakoff effect and lifetime measurements [32]. Until now only the Crystal Ball measured the π^0 width in e^+e^- collisions. For most detectors it is not possible to trigger on the low energy photons of the π^0 decay. Figure 6 shows the $\gamma\gamma$ mass spectrum obtained by the Crystal Ball group at DORIS [34]. Containing the π^0, η and η' peaks this plot is a comprehensive presentation of the light pseudoscalar mesons. The Crystal Ball result for the $\gamma\gamma$ width of the π^0 (Table 1) does not yet reach the same precision as a recent lifetime measurement [35].

Meson	Decay Mode	$\Gamma_{\gamma\gamma}$ [keV]	Experiment
π^0		$(7.85 \pm 0.54) \cdot 10^{-3}$	PDG (1984)
		$(7.25 \pm 0.18 \pm 0.11) \cdot 10^{-3}$	NA30 (lifetime) [35]
		$(7.8 \pm 0.4 \pm 0.9) \cdot 10^{-3}$	Crystal Ball (prel.) [34]
π^0		$(7.48 \pm 0.33 \pm 0.31) \cdot 10^{-3}$	average[a]
η		1.00 ± 0.22	DESY (Primakoff) [38]
		0.324 ± 0.046	Cornell (Primakoff) [39]
η		$0.56 \pm 0.12 \pm 0.10$	Crystal Ball (SPEAR) [40]
		$0.53 \pm 0.04 \pm 0.04$	JADE [41]
		$0.64 \pm 0.14 \pm 0.13$	TPC/$\gamma\gamma$ [42]
		$0.51 \pm 0.02 \pm 0.06$	Crystal Ball (DORIS) (prel.) [43]
η		0.53 ± 0.04	average (e^+e^- only)
η'	miss.-mass	5.4 ± 2.1	πp scattering [44]
	$\rho\gamma$	$5.8 \pm 1.1 \pm 1.2$	Mark II (SPEAR) [45]
	$\rho\gamma$	$6.2 \pm 1.1 \pm 0.8$	CELLO [46]
	$\rho\gamma$	$5.0 \pm 0.5 \pm 0.9$	JADE [47]
	$\rho\gamma$	$5.1 \pm 0.4 \pm 0.7$	TASSO [48]
	$\rho\gamma$	$3.8 \pm 0.26 \pm 0.43$	PLUTO [49]
	$\rho\gamma$	$4.5 \pm 0.3 \pm 0.7$	TPC/$\gamma\gamma$ [51]
	$\gamma\gamma$	4.0 ± 0.9	JADE [41]
	$\rho\gamma$	3.8 ± 0.5	Mark II (PEP) (prel.) [50]
	$\eta\pi\pi(\eta \to \gamma\gamma)$	4.3 ± 0.8	Mark II (PEP) (prel.) [50]
	$\eta\pi\pi(\eta \to 3\pi)$	3.6 ± 1.0	Mark II (PEP) (prel.) [50]
η'		4.3 ± 0.3	average

[a] from [32], does not include preliminary Crystal Ball result.

Table 1: Two-photon widths of pseudoscalar mesons.

The η and η' mesons

Measurements of the $\gamma\gamma$ widths of η and η' are of interest for two reasons. Historically, the measured η' width ruled out the integer charge quark model as constructed by Han and Nambu [36], giving a value four times as large as the usual fractional charge model. More recently, attention has been paid to these measurements because they determine possible admixtures of gluonium to the SU_3 singlet $q\bar{q}$ component in the η' wave function.

The first measurements of the $\gamma\gamma$ width of the η meson employed the Primakoff

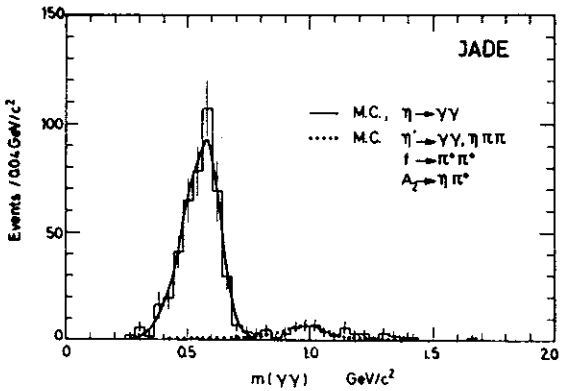

Figure 7: Two-photon invariant mass spectrum showing the η signal obtained with the JADE detector [41].

effect [37]. The value generally accepted was obtained at Cornell [39]:

$$\Gamma_{\eta\gamma\gamma} = (0.324 \pm 0.046)\ keV \qquad \text{(Primakoff)}.$$

The $\gamma\gamma$ width of the η determined at e^+e^- storage rings, first by the Crystal Ball at SPEAR [40] and then with better statistics by JADE [41] (Fig.7), turned out to be much larger than the Cornell value. Averaging all storage ring measurements (see Table 1) yields:

$$\Gamma_{\eta\gamma\gamma} = (0.53 \pm 0.04)\ keV \qquad \text{(storage ring)}.$$

The discrepancy between the Cornell result using the Primakoff effect and the storage ring measurements is not yet understood [33].

A large number of measurements is available for the $\gamma\gamma$ width of the η' (Table 1). The first measurement, done by the Mark II group at SPEAR, was also the first observation of a resonance produced in two-photon collisions in a storage ring [45]. In this experiment and in most of the others the η' was detected via the decay mode $\eta' \to \gamma\rho^0$. This radiative transition is described by a magnetic dipole matrix element, that reads in the ρ rest frame [52]:

$$|M|^2 \sim \frac{k^2 q^2 M_{\pi\pi}^2 \sin^2\theta}{(M_{\pi\pi}^2 - M_\rho^2)^2 + M_\rho^2\Gamma_\rho^2}, \tag{13}$$

where k is the photon energy, q the pion momentum and θ the angle between a pion and the photon direction (all given in the ρ rest system). The matrix element determines the decay angular distribution of the ρ and induces a downward shift of the ρ peak by about 20 MeV. Both effects may change the acceptance. Two

of the experiments [46,47] did not include the matrix element for the acceptance calculations[1]. However, in both cases the acceptance effects are claimed to be small [53] and thus there is no reason to exclude these measurements from the average over all experiments. Two measurements of the $\gamma\gamma$ width of the η' are independent of this matrix element: JADE analyzed $\eta' \to \gamma\gamma$ [41] and Mark II $\eta' \to \eta\pi^+\pi^-$ [50]. All results listed in Table 1 are in agreement within errors and yield an average value:

$$\Gamma_{\eta'\gamma\gamma} = 4.3 \pm 0.3\ keV.$$

Discussion of the results on pseudoscalar mesons

Pseudoscalar Mixing: Assuming SU(3) octet symmetry, but not explicitly nonet symmetry, one obtains the following relations between the $\gamma\gamma$ widths of the pseudoscalar mesons and the angle Θ_P which determines the $\eta - \eta'$ mixing,

$$\begin{aligned} 3 \cdot \frac{\Gamma_{\eta\gamma\gamma}}{m_\eta^3} &= \frac{\Gamma_{\pi^0\gamma\gamma}}{m_{\pi^0}^3} \cdot (\cos\Theta_P - \sqrt{8}R_P \sin\Theta_P)^2 \\ 3 \cdot \frac{\Gamma_{\eta'\gamma\gamma}}{m_{\eta'}^3} &= \frac{\Gamma_{\pi^0\gamma\gamma}}{m_{\pi^0}^3} \cdot (\sin\Theta_P + \sqrt{8}R_P \cos\Theta_P)^2. \end{aligned} \qquad (14)$$

The parameter R_P is the ratio of the singlet and octet wave functions at the origin allowing for a breaking of SU(3) nonet symmetry.

Using the average $\gamma\gamma$ widths from Table 1 (for η only the storage ring results) one obtains

$$\begin{aligned} \Theta_P &= -18.2^\circ \pm 2.5^\circ \\ R_P &= 0.93 \pm 0.03. \end{aligned}$$

The result $R_P \approx 1$ means that within this simple ansatz the octet and singlet wave functions are similar. The angle Θ_P is significantly different from the one obtained with the Gell-Mann - Okubo mass formula yielding $\Theta_P \approx -10^\circ$, but is in agreement with $\Theta_P \approx -18^\circ$ as obtained from η and η' production in hadronic reactions [55].

The above determination of the pseudoscalar mixing may be too naive. In a more general approach possible gluonic admixtures have to be included and different processes involving pseudoscalars have to fit quantitatively into the model. Including experimental results on vector-pseudoscalar radiative transitions one finds that the η is nearly entirely a $q\bar{q}$ state, while some gluonium admixture in the η' is possible [56,57]. This admixture in the η' could be fixed by a measurement of the decay $\phi \to \gamma\eta'$.

No other light pseudoscalar resonances were observed in two-photon reactions. In particular no signal was found for the $\eta(1440)$ in the $K\bar{K}\pi$ decay mode and for a

[1] Although not indicated in the paper, the first measurement by the Mark II group included the matrix element [54].

radially excited η, such as the $\eta(1275)$. The upper limits are summarized in Sect. 2.7.

The glueball connection: The $\eta(1440)$, originally called $\iota(1460)$, is copiously produced in J/ψ radiative decays. Therefore, and because it does not easily fit into a $q\bar{q}$ multiplet, it is regarded as a strong candidate for being a glueball. The non-observation in two-photon reactions, see Table 5 (Sect.2.7), supports this hypothesis.

Integer quark charges: In standard QCD all physical observables are color singlets and, in particular, photons are color blind. In early attempts to construct quark models with integer quark charges [36], however, the electromagnetic current is a mixture of a color singlet and a color octet component, the (color-flavor) decomposition being $\gamma = (8,1) \oplus (1,8)$. Since low lying hadrons are always found to be color singlets, the color octet component can only contribute to reactions involving at least two photons. The combination of two color octet photon components yields a color singlet which is at the same time a flavor singlet: $\gamma \otimes \gamma \to (8 \otimes 8, 1) = (1,1) \oplus$ color non-singlets [58]. Therefore only the two-photon couplings of flavor singlets are sensitive to fractional and integer quark charges. In the pseudoscalar multiplet the η' is mainly a flavor singlet. If nonet symmetry holds one obtains from the measured π^0 width:

$$\Gamma_{\eta'\gamma\gamma} \approx \begin{array}{ll} 6\ keV & \text{(fractional quark charges)} \\ 24\ keV & \text{(integer quark charges).} \end{array}$$

The comparison of these numbers with the measured $\gamma\gamma$ width of 4.3 keV can be taken as evidence for fractional quark charges. The assumption of nonet symmetry can be relaxed by including other decay amplitudes in the analysis [59].

2.4 The Tensor Mesons

The tensor mesons $a_2(1320)$, $f_2(1270)$, $f_2'(1525)$ and $K^*(1430)$ are P-wave quark antiquark states with aligned spins ($J^{PC} = 2^{++}$). The decay of a tensor meson into two real photons is determined by two independent amplitudes which may be taken as the $\lambda=0$ and $\lambda=2$ $\gamma\gamma$ helicity amplitudes ($\lambda=1$ does not contribute for real photons). It has been predicted that $\lambda=2$ (photons with opposite helicities) should dominate over $\lambda=0$ (photons with the same helicities). The helicity 2 dominance follows just from a Clebsch-Gordon decomposition if only the lowest multipole in the $\gamma\gamma$ system contributes and if the two matrix elements are not very different. If they are equal the intensities for $\lambda=0$ and 2 will be in the ratio 1 : 6. Helicity 2 dominance has been derived from finite energy sum rules [60,61]. So far, none of the experiments is in contradiction to this prediction. However, in most cases the experiments have not been very sensitive to different helicity contributions.

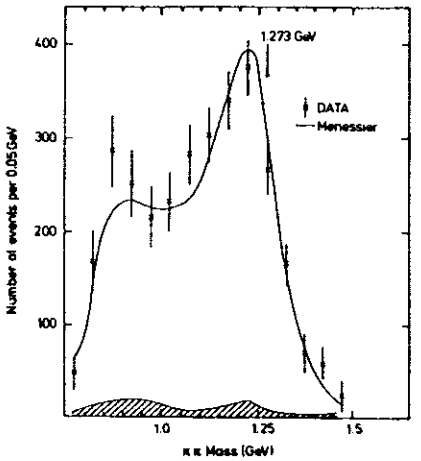

Figure 8: Two-photon production of $\pi^+\pi^-$ pairs measured by CELLO [69]. The hatched area is the estimated K^+K^- background. On the low mass side the spectrum is cut off by the acceptance.

If the tensor mesons are ideally mixed, i.e. if the f_2 is mainly $u\bar{u} + d\bar{d}$ and the f_2' mainly $s\bar{s}$, SU(3) symmetry yields for the ratios of the squared coupling constants:

$$g^2_{a_2\gamma\gamma} : g^2_{f_2\gamma\gamma} : g^2_{f_2'\gamma\gamma} = 9 : 25 : 2. \qquad (15)$$

Absolute predictions for the $\gamma\gamma$ couplings of the light tensor mesons [60,61,62] cannot be obtained from first principles as in the case of the pseudoscalars.

The $f_2(1270)$ resonance

The formation of the $f_2(1270)$ resonance by two-photons has been detected via the two dominant decay channels $f_2 \to \pi^+\pi^-$ *and* $f_2 \to \pi^0\pi^0$. The charged pion decay mode is troubled by large backgrounds from two-photon production of lepton pairs. This background has to be removed by particle identification, which is difficult at low momenta, or by a statistical subtraction using simulation programs for QED reactions [63].

The background from continuum production of $\pi^+\pi^-$ has been calculated from the Born diagrams in which the photons couple to pointlike spinless particles. Obviously there is no $\pi^0\pi^0$ continuum in this approximation. Extending the Born approximation by including resonances leads to strong interference effects between the continuum and the f_2 resonance. Note that the helicity 2 amplitude of the Born term dominates in the f_2 region as for the tensor mesons. Experimentally the interference in the two-pion mass distribution is constructive below and destructive above the f_2 peak (see Fig.8).

Various attempts have been made to improve the theoretical description of pion pair production beyond the Born approximation including resonances in a consistent way. In Mennessier's model [64] a coupled channel treatment of $\pi\pi$ and $K\overline{K}$ is pursued. The pion exchange and additional ρ and ω exchanges are unitarized by including $\pi\pi$ and $K\overline{K}$ final state interactions as given by measured phase shifts. In addition a direct coupling of the photons to resonances is introduced.

In Fig.8 the $\pi^+\pi^-$ invariant mass spectrum as measured by the CELLO group [69] is compared to the model of Mennessier. The solid curve has been calculated including only the unitarized Born term and the coupling to the f_2 resonance. In particular, a contribution from a scalar resonance was not required by the data. This Born model, with or without unitarization, explains the observed downward shift of the f_2 peak by about 40 MeV in the $\pi^+\pi^-$ channel.

The Crystal Ball is the only experiment so far that published results on the two-photon formation of the f_2 by analyzing the $\pi^0\pi^0$ decay channel [68]. The $\pi^0\pi^0$ invariant mass distribution shows a resonance enhancement in the f_2 region which is shifted downward by about 35 MeV and which is somewhat broader than expected from the standard f_2 resonance parameters. A mass shift is not expected in the $\pi^0\pi^0$ channel due to the vanishing of the Born term. The systematic error in the mass determination together with the statistical error could account for the observed shift. Preliminary results from JADE [74] and new Crystal Ball measurements at DORIS [43] do not indicate such a shift (see Fig.14 below).

The Crystal Ball group also measured the helicity structure of f_2 formation by analyzing the $\pi^0\pi^0$ angular distribution. The λ=0 and λ=1 contributions were fitted to be (12±39)% and (2±11)%, respectively, of the λ=2 component, consistent with the predicted λ=2 dominance.

In the case of virtual photons the helicity structure of f_2 formation may become very complicated. Helicity 1 is expected to be suppressed only at very low Q^2 and may even dominate at large Q^2 [75]. As long as the low statistics of single-tag data on f_2 formation do not allow for a partial wave analysis the experiments have to rely on models, e.g. [76], for calculating acceptance corrections. Therefore it is difficult to interpret the few available single-tag measurements of f_2 formation [67,71,73].

The results of the different experiments on the $\gamma\gamma$ width of the f_2 are summarized in Table 2. Helicity 2 dominance was always assumed. The average of all published results is:

$$\Gamma_{f_2\gamma\gamma} = (2.78 \pm 0.14)\ keV.$$

The $a_2(1320)$ meson

The two-photon formation of the $a_2(1320)$, the isovector member of the tensor meson multiplet, was measured via the decay modes $a_2 \to \pi^0\eta$ and $a_2 \to \rho^\pm\pi^\mp$. The $\pi^0\eta$ signal was observed by the Crystal Ball group [77,79] in the four-photon

Meson	Mode	$\Gamma_{\gamma\gamma}$ [keV]	Experiment	Ref
$f_2(1270)$	$\pi\pi$	$2.3 \pm 0.5 \pm 0.35$	PLUTO	[65]
	$\pi\pi$	$3.6 \pm 0.3 \pm 0.5$	MARK II/SPEAR	[66]
	$\pi\pi$	$3.2 \pm 0.2 \pm 0.6$	TASSO	[67]
	$\pi\pi$	$2.7 \pm 0.2 \pm 0.6$	Crystal Ball/SPEAR	[68]
	$\pi\pi$	$2.5 \pm 0.1 \pm 0.5$	CELLO	[69]
	$\pi\pi$	$2.70 \pm 0.05 \pm 0.2$	DELCO	[70]
	$\pi\pi$	$2.52 \pm 0.13 \pm 0.38$	Mark II	[71]
	$\pi\pi$	$2.85 \pm 0.25 \pm 0.5$	PLUTO	[72]
	$\pi\pi$	$3.2 \pm 0.1 \pm 0.4$	TPC/$\gamma\gamma$	[73]
$f_2(1270)$		2.78 ± 0.14	average	
$a_2(1320)$	$\eta\pi$	$0.77 \pm 0.18 \pm 0.27$	Crystal Ball (SPEAR)	[77]
	$\rho\pi$	$0.81 \pm 0.19^{+0.42}_{-0.11}$	CELLO	[46]
	$\rho\pi$	$1.06 \pm 0.18 \pm 0.19$	PLUTO	[78]
	$\eta\pi$	$1.14 \pm 0.20 \pm 0.26$	Crystal Ball (DORIS)	[79]
	$\rho\pi$	$0.90 \pm 0.27 \pm 0.16$	TASSO	[80]
$a_2(1320)$		0.95 ± 0.14	average	
$f_2'(1525)$	KK	$(0.11 \pm 0.02 \pm 0.04)$	TASSO	[81]
$\times$ Br($f_2' \to K\overline{K}$)	KK	$(0.12 \pm 0.07 \pm 0.04)$	TPC/$\gamma\gamma$	[73]
	KK	$(0.07 \pm 0.015 \pm 0.035)$	DELCO	[83]
	KK	(0.10 ± 0.04)	Mark II (prelim.)	[84]
$f_2'(1525)$	$K\overline{K}$	(0.094 ± 0.023)	average	
$\times$ Br($f_2' \to K\overline{K}$)				

Table 2: Two-photon widths of tensor mesons.

final state. The $\pi^0\eta$ mass distribution in Fig.10 exhibits a two peak structure which can be described by the $a_2(1320)$ and the $a_0(975)$.

All other experiments analyzed the decay mode $a_2 \to \rho^{\pm}\pi^{\mp} \to \pi^+\pi^-\pi^0$. The analysis of this channel has to account for correlations in the three pion final state arising from angular momentum conservation and the interference between the a_2 decay channels $\rho^+\pi^-$ and $\rho^-\pi^+$. The matrix elements describing the a_2 decay in different $\gamma\gamma$ helicity states can be found in [80].

The results of the various experiments on the $\gamma\gamma$ width of the a_2 are listed in Table 2. In all experiments λ=2 was assumed. The average value is:

$$\Gamma_{a_2\gamma\gamma} = (0.95 \pm 0.14)\ keV.$$

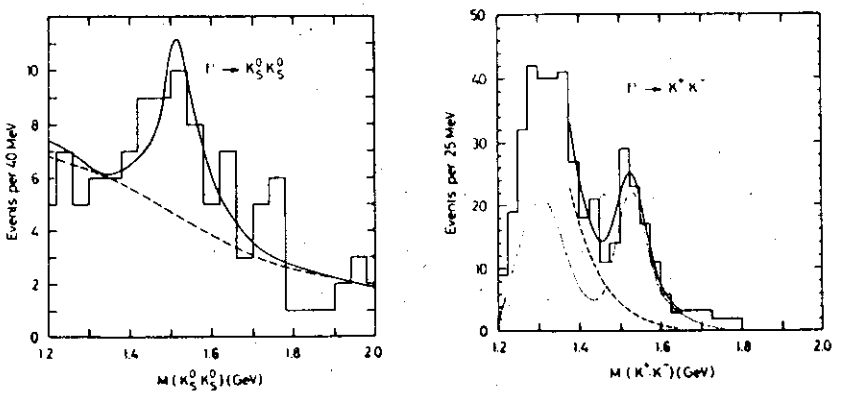

Figure 9: Two-photon production of $K\overline{K}$ pairs measured by TASSO [81].

The $f_2'(1525)$ meson

The third member of the tensor meson multiplet for which a $\gamma\gamma$ width was measured is the $f_2'(1525)$ meson. It decays dominantly into $K\overline{K}$ indicating that it mainly contains strange quarks.

The TASSO group observed the f_2' in the two decay channels [81]: $f_2' \to K^+K^-$ and $f_2' \to K^0_SK^0_S$. The mass spectrum of K^+K^- pairs in Fig.9 shows a peak in the f_2' region. The enhancement below the f_2' is probably due to f_2 and a_2 decays into K^+K^- and due to a K^+K^- continuum. The $K^0_SK^0_S$ mass spectrum in Fig.9 shows a f_2' signal above a background of misidentified $K^0_SK^0_S$ pairs (indicated by the dashed curve). In the measured mass range there is little room for other resonance contributions.

The difference between the K^+K^- and the $K^0_SK^0_S$ mass spectra can be explained by an interference between the a_2, f_2, and f_2' resonances [81,82]. The model predicts that the f_2-a_2 interference is destructive in the $K^0\overline{K^0}$ channel and constructive in the K^+K^- channel. Although this is consistent with the data, the uncertainty in the K^+K^- continuum contribution and the limited statistics in the $K^0\overline{K^0}$ channel do not allow proving the validity of the model.

The final result for $\Gamma_{f_2'\gamma\gamma} \cdot B(f_2' \to K\overline{K})$ as obtained by fitting interfering resonances and background terms to the mass spectra is given in Table 2 together with recent results of other experiments. All experiments assumed helicity 2 dominance. The average value is:

$$\Gamma_{f_2'\gamma\gamma} \cdot B(f_2' \to K\overline{K}) = (0.094 \pm 0.023)\ keV.$$

Since the branching ratio for the f_2' decay into $K\overline{K}$ is not yet known the $\gamma\gamma$ width of the f_2' could not be extracted from this result.

Discussion of the results for tensor mesons

The $\gamma\gamma$ widths of the tensor mesons cannot be predicted from first principles. However, interesting SU(3) relations can be tested that can shed some light on the possible mixing with nearby 2^{++} glueballs.

Neglecting λ=0 contributions, the $\gamma\gamma$ width of a tensor meson depends on one coupling constant, $g_{T\gamma\gamma}$, only. In terms of this coupling constant the $\gamma\gamma$ width can be written as [85]

$$\Gamma_{T\gamma\gamma} = \frac{g^2_{T\gamma\gamma}}{4\pi}\frac{m_T^3}{80\mu^2}. \qquad (16)$$

In this formula μ may either be assumed to be a common scale for the tensor meson nonet or may be identified with the mass of the specific meson so that SU(3) relations hold for $\Gamma_{T\gamma\gamma}/m_T$ or $\Gamma_{T\gamma\gamma}/m_T^3$. The tensor meson mixing parameters Θ_T and R_T can then be obtained similarly to the case of the pseudoscalars (see (14)). From the average $\gamma\gamma$ widths in Table 2 one obtains the following mixing parameters (assuming B($f_2' \to K\overline{K}$)= 1):

$$\text{no mass dep.}: \begin{array}{l}\Theta_T = 29.8^\circ \pm 3.8^\circ \\ R_T = 1.00 \pm 0.18\end{array} \qquad \text{cubic mass dep.}: \begin{array}{l}\Theta_T = 26.5^\circ \pm 3.1^\circ \\ R_T = 1.06 \pm 0.15\end{array}$$

The mixing angle Θ_T is close to the value for ideal mixing, Θ_{ideal}= 35.26°, that means f_2' is an almost pure $s\bar{s}$ state. The TASSO collaboration finds the $u\bar{u} + d\bar{d}$ content in the f_2' to be less than 3% at a 95% confidence level (for $0.5 \leq$ B($f_2' \to K\overline{K}$)$\leq$ 1.0) [81].

The fitted value of R_T is consistent with SU(3) nonet symmetry ($R_T \approx$ 1) with and without the cubic mass corrections. As a consequence additional nearby tensor states, such as glueballs, which mix with the $q\bar{q}$ states, are experimentally not required. The tensor mesons appear as a clean example of an ideally mixed SU(3) $q\bar{q}$ multiplet.

No other light tensor meson states were found in $\gamma\gamma$ reactions. In particular, upper limits have been given for the glueball candidate $f_2(1720)$ [old name $\Theta(1690)$], see Table 5.

2.5 Scalar Mesons

The scalar meson multiplet (J^{PC}= 0^{++}) is the least settled of the low-spin $q\bar{q}$ multiplets. Although $q\bar{q}(0^{++})$ states are closely related to the tensor mesons which belong to the same P-wave triplet of $q\bar{q}$ states, the scalar mesons are much less understood. Candidate states are the isovector $a_0(980)$ and the isoscalar $f_0(975)$ [old names: δ and S^*]. For the other possible isoscalar member, the ϵ, even the mass is not established found by some people around 800 MeV and by others around 1300 MeV.

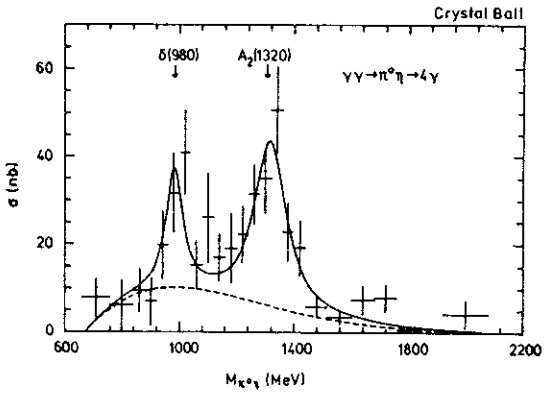

Figure 10: Cross section for $\gamma\gamma \to \eta\pi^0$ [79].

The $a_0(980)$ and $f_0(975)$ resonances: The first measurement of the $\gamma\gamma$ width of a scalar meson comes from the Crystal Ball group at DORIS [79]. The cross section for $\gamma\gamma \to \pi^0\eta$ shows, besides a signal from the $a_2(1320)$, an enhancement in the region of the $a_0(980)$ (Fig.10). Fitting two standard Breit-Wigner curves and a smooth background to the data yields the following result:

$$\Gamma_{a_0\gamma\gamma} \cdot B(a_0 \to \pi^0\eta) = (0.19 \pm 0.07^{+0.10}_{-0.07})\ keV.$$

The branching ratio B($a_0 \to \pi^0\eta$) is unknown but may be the dominant one. If so, the $\gamma\gamma$ width of the a_0 is relatively small compared to most of the predictions for a scalar $q\bar{q}$ state [86]. A small value, however, is expected if the a_0 is a $qq\bar{q}\bar{q}$ state with a dominant pseudoscalar-pseudoscalar decomposition which leads via vector meson dominance to a suppression of the $\gamma\gamma$ coupling [7]

It has been suggested that the a_0 and f_0 states are virtually bound $K\overline{K}$ states or $K\overline{K}$ molecules leading to scalar $K\overline{K}$ enhancements near threshold [8,87]. Figure 11 exhibits the cross section for $\gamma\gamma \to K^0\overline{K}^0$ obtained by the TASSO group [88]. The curve shows the expected P-wave contribution from tensor meson excitations. The small excess near threshold is consistent with S-wave production. Using the Crystal Ball measurement of the $a_0(980)$ and a coupled channel parametrization of the $\pi^0\eta$ and $K\overline{K}$ decay modes [89] one obtains the dotted curve for the a_0 contribution which is, however, too small to explain the measured cross section. In addition, the $f_0(975)$ resonance could contribute up to about 10 nb in the first bin of Fig.11 to be consistent with the JADE upper limit for $\Gamma_{f_0\gamma\gamma}$ in Table 5. Thus it is possible that the measured cross section for $\gamma\gamma \to K^0\overline{K}^0$ near threshold can be explained by a_0 and f_0 resonance formation.

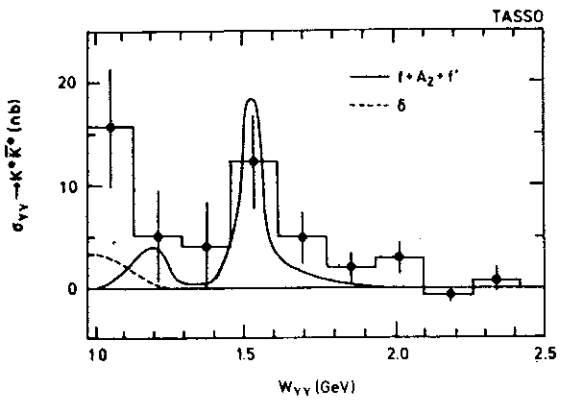

Figure 11: Cross section for $\gamma\gamma \to K^0\overline{K^0}$ [88].

Search for low mass scalar resonances: Several experiments searched for the two-photon formation of a scalar resonance at low mass decaying into pion pairs. Fig.12 shows the differential cross section for $\gamma\gamma \to \pi^+\pi^-$ at pion c.m. angles near 90° in a $W_{\gamma\gamma}$ range from threshold to the $f_2(1270)$ region, as measured by PLUTO [72]. Above $W_{\gamma\gamma} \approx 0.8$ GeV the data are reasonably described by models where the f_2 contribution is coherently added to the continuum background (curves 2 and 3). Between 0.5 GeV and the f_2 region no other resonance contribution is observed. The data even fall below the Born term (curve 4) around 0.6 GeV. However, this dip is not confirmed by other measurements, e.g. [66,73].

The two data points around 400 MeV are about a factor of two higher than the Born cross section. Including a systematic error of about 20% the significance is only about 2 standard deviations. This issue becomes more interesting if one compares the PLUTO results with measurements obtained at the DCI storage ring with the DM1 [90] and DM2 [91] detectors. The $\pi^+\pi^-$ mass spectrum from DM2 is shown in Fig.13. Below $W_{\gamma\gamma} = 0.7$ GeV 2.3 ± 0.4 times more events were found than expected from a residual QED background and the $\pi^+\pi^-$ Born term. Two bins around 400 MeV lie significantly above the full curve (about 4.6 standard deviations), in striking agreement with the shape of the $\pi^+\pi^-$ cross section determined by PLUTO. Quantitatively, however, the excess in the DM2 data appears to be much larger. Describing the enhancement by a broad ϵ resonance results in a mass around 700 MeV. However, it has been argued [92] that current algebra constraints on the cross section require a narrow resonance near threshold to explain the enhancement. Such a resonance would have to be endowed with rather peculiar properties to conform with other experiments.

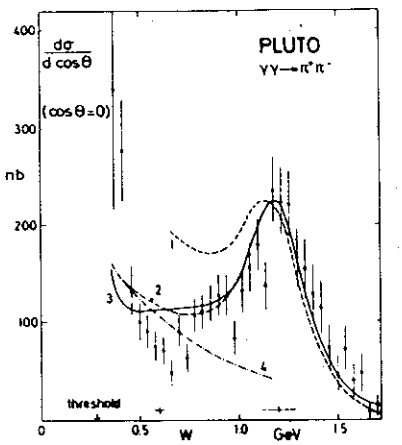

Figure 12: Differential cross section for $\gamma\gamma \to \pi^+\pi^-$ for pion c.m. angles $\Theta = 90°$ [72].

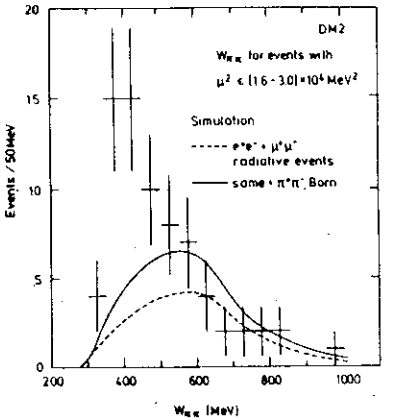

Figure 13: Measured rate of $\gamma\gamma$ production of $\pi^+\pi^-$ pairs [91].

Two-photon production of a $\pi\pi$ resonance should be easier to observe in the $\pi^0\pi^0$ final state because there is no continuum background at the Born level. The Crystal Ball group presented preliminary data on this channel down to the threshold region [43] (Fig.14). Below the $f_2(1270)$ resonance the cross section is rather low and flat, as expected from a $\pi\pi$ coupled channel analysis without resonance contributions [92]. Experimentally, however, a broad resonance in this region cannot be excluded.

Conclusions: All $\gamma\gamma$ widths of scalar mesons seem to be small compared with those of tensor mesons. This gives strong support to the picture that the scalar state $a_0(980)$ and $f_0(975)$ are not 0^{++} $q\bar{q}$ bound states. On the other hand, the measured $\gamma\gamma$ widths can theoretically be explained if these states are $q\bar{q}q\bar{q}$ compounds (Table 3). The smallness of the total a_0 width, however, cannot be reconciled with a bag model $q\bar{q}s\bar{s}$ state that should readily decay into $\eta\pi$. Weakly bound $K\overline{K}$ molecule states may rather be the correct interpretation of these resonances [87].

The enhancement in the $\pi^+\pi^-$ mass spectrum near threshold needs experimental confirmation. It has still to be shown that the explanation by a resonance is consistent with the observed $\pi^0\pi^0$ mass spectrum.

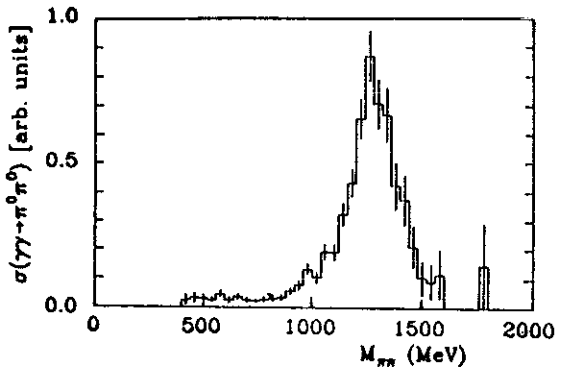

Figure 14: Two-photon production of $\pi^0\pi^0$ pairs for invariant masses from close to threshold to the $f_2(1270)$ region.

Theoretical Model	$\Gamma(a_0 \to \gamma\gamma)$ [keV]	$\Gamma(f_0 \to \gamma\gamma)$ [keV]	Ref.
$(q\bar{q})$ quark model	2.5-3.8	$\frac{25}{9}\Gamma(\delta_0 \to \gamma\gamma)$	[93]
	4.8	$\frac{25}{9}\Gamma(\delta_0 \to \gamma\gamma)$	[94]
	1.1	3.0	[87]
	1.5	4.5	[87]
$q\bar{q}q\bar{q}$ bag model	~ 0.27	~ 0.27	[7]
$K\bar{K}$ molecule	0.6	0.6	[95]
Experiments	$0.19 \pm 0.07^{+0.10}_{-0.07}$ $\overline{B(a_0 \to \eta\pi)}$	< 0.8	[79], [74]

Table 3: Theoretical and experimental results for the $\gamma\gamma$ widths of $a_0(980)$ and $f_0(975)$ (from [87]).

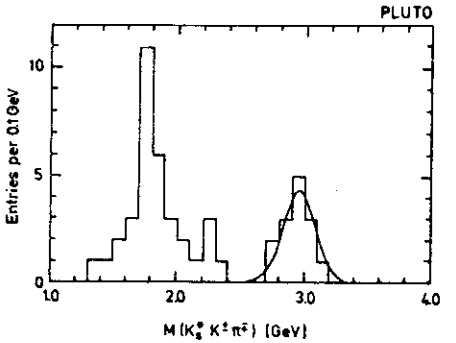

Figure 15: Two-photon production of the $K^0_S K^\pm\pi^\mp$ final state [96]. The solid curve is the distribution expected for the $\eta_c(2980)$.

2.6 Charmonium States

The PLUTO collaboration for the first time measured the two-photon production of the charmonium state η_c [96]. In a data sample corresponding to an integrated luminosity of 45 pb^{-1} they searched for the reaction

$$\gamma\gamma \;\to\; \eta_c \;\to\; K^0_S K^\pm\pi^\mp. \qquad (17)$$

The K^0_S's were observed via their $\pi^+\pi^-$ decay mode and identified by requiring that the $\pi^+\pi^-$ came from a secondary vertex separated from the primary e^+e^- collision point. The charged kaons and pions in reaction (17) were not identified. Therefore, both the $K^+\pi^-$ and the $K^-\pi^+$ assignments were tried leading to two entries per event in the KKπ invariant mass plot of Fig.15. In the η_c region, the difference in the KKπ invariant mass of these two combinations is smaller than the mass resolution of about 100 MeV.

The PLUTO group found 7 events in the η_c region distributed as expected from the detector resolution. The background in the η_c region is assumed to be negligible. From the observed 7 events the PLUTO group obtained for the product of the $\gamma\gamma$ width times the branching ratio into $K^0_S K^\pm\pi^\mp$:

$$\Gamma(\eta_c \to \gamma\gamma) \cdot B(\eta_c \to K^0_S K^\pm\pi^\mp) \;=\; (0.5\,^{+0.2}_{-0.15} \pm 0.1)\; keV.$$

Because of isospin invariance the $K^0_S K^\pm\pi^\mp$ branching ratio is 1/3 of the $K\bar{K}\pi$ branching ratio. These η_c decay modes were studied by the Mark III group in radiative J/ψ decays [97]. Using the branching ratio $B(J/\psi \to \gamma\eta_c) = (1.27 \pm 0.36)\%$ from the Crystal Ball [98] they obtained $B(\eta_c \to K\bar{K}\pi) = (6.1 \pm 2.2)\%$. With this branching ratio the PLUTO measurement yields the $\gamma\gamma$ width:

$$\Gamma(\eta_c \to \gamma\gamma) \;=\; (33 \pm 18)\; keV \quad (PLUTO)$$

State	$\Gamma_{\gamma\gamma}$ [keV]	$\Gamma_{\gamma\gamma} \cdot B(\eta \to K_S K^\pm \pi^\mp)$	Experiment
$\eta_c(2980)$	33 ± 18	$0.5^{+0.2}_{-0.15} \pm 0.1$	PLUTO [96]
	9.8 ± 7.4	$0.15^{+0.11}_{-0.08} \pm 0.05$	MARK II [99], prelim.
		$4.3^{+3.4}_{-3.7} \pm 2.4$	R704 [100]
		< 11 (90% c.l.)	MD-1 [101], prelim.
$\chi_0(3415)$	4.0 ± 2.8 or < 8.0 (90% c.l.)		Crystal Ball [104]
$\chi_2(3555)$	2.8 ± 2.0		Crystal Ball [104]
	$2.9^{+1.3}_{-1.0} \pm 1.7$		R704 [100]

Table 4: Two-photon widths of charmonium states.

Table 4 contains also results on the $\gamma\gamma$ width of the η_c from the Mark II, the R704 and the MD-1 experiments. In the R704 experiment the reaction $p\bar{p} \to \eta_c \to \gamma\gamma$ was observed at the ISR by scattering an antiproton beam off a hydrogen jet target [100]. The MD-1 experiment tried to measure directly the $\gamma\gamma$ width of the η_c in a double-tag experiment by searching for a resonance structure in the total cross section [101]. Such a measurement is independent of branching ratios which introduce large uncertainties in the other results.

Theoretically the $\gamma\gamma$ width of the singlet state η_c can be related to the leptonic width of the triplet state J/ψ. Both depend on the quark wave function $\Psi(0)$ at the origin which, in first approximation, should be equal for the singlet and triplet states:

$$\frac{\Gamma(^1S_0 \to \gamma\gamma)}{\Gamma(^3S_0 \to l^+l^-)} = \frac{3e_q^4|\Psi(0)|^2/m_q^2}{e_q^2|\Psi(0)|^2/m_q^2} = 3e_q^2$$

Using the measured leptonic widths of the J/ψ, ψ' and the Υ yields the following estimates:

$$\begin{aligned} \Gamma_{\eta_c \to \gamma\gamma} &\approx 6.2\ keV \\ \Gamma_{\eta_c' \to \gamma\gamma} &\approx 2.6\ keV \\ \Gamma_{\eta_b \to \gamma\gamma} &\approx 0.4\ keV. \end{aligned} \qquad (18)$$

Similar results were obtained using QCD sum rules [102]. These estimates are based on the assumption that the singlet and triplet wave functions are roughly equal. However, the experimental result that the measured rate of the transition $J/\psi \to \gamma\eta_c$ is much smaller than theoretically expected, may be due to differences in the wave functions. If this is the case the estimates of the $\gamma\gamma$ widths in (18) would become lower [103].

The Crystal Ball and R704 experiments obtained results on the $\gamma\gamma$ widths of

R	X	$\Gamma_{R\gamma\gamma} \cdot B(R \to X)$ [keV]	Experiment	Ref
$\eta(1440)$ formarly ι	$K\bar{K}\pi$	< 2.2 (95% c.l.)	TASSO	[88]
	$K\bar{K}\pi$	< 2.0 (90% c.l.)	Mark II	[50]
	$K\bar{K}\pi$	< 1.6 (95% c.l.)	TPC/$\gamma\gamma$	[107]
	$\rho^0\rho^0$	< 1.0 (95% c.l.)	TASSO	[114]
	$\rho\gamma$	< 1.5 (95% c.l.)	TASSO	[48]
	$\rho\gamma$	< 0.2 (90% c.l.)	Mark II	[50]
$f_2(1720)$ formerly θ	$K\bar{K}$	< 0.28 (95% c.l.)	TASSO	[88]
	$\pi^+\pi^-$	< 0.17 (95% c.l.)	TPC/$\gamma\gamma$	[73]
	K^+K^-	< 0.10 (95% c.l.)	TPC/$\gamma\gamma$	[73]
	$\rho^0\rho^0$	< 0.12 (95% c.l.)	TASSO	[114]
	$\eta\eta$	< 0.3 (95% c.l.)	Crystal Ball	[105]
$f_0(975)$	$\pi\pi$	< 0.8 (95% c.l.)	Crystal Ball	[68]
	all	< 0.8 (95% c.l.)	JADE	[74]
$\epsilon(1300)$	$\pi^+\pi^-$	< 1.5 (95% c.l.) for $1.3 < M < 1.5\ GeV$	TASSO	[67]
$\eta(1275)$	$\eta\pi\pi$	< 0.3 (90% c.l.)	Crystal Ball	[99]
$h(2030)$	$K\bar{K}$	< 0.29 (95% c.l.)	TASSO	[88]
$\xi(2220)$	$K\bar{K}$	< 1.09 (95% c.l.)	TASSO	[88]

Table 5: Upper limits on two-photon resonance couplings.

the P-wave states $\chi_0(3415)$ and $\chi_2(3555)$ (Table 4). Within the errors the ratios of the $\gamma\gamma$ widths and the hadronic widths are consistent with the assumption that the hadronic decays proceed via two gluons. The results are also consistent with a ratio $\Gamma_{\chi_0\gamma\gamma}/\ \Gamma_{\chi_2\gamma\gamma} = 15/4$ expected from spin factors if the wave functions are equal.

2.7 Search for other Resonances

Table 5 contains a list of limits for resonance formation by two photons in various decay channels. For the comparison with theoretical models the following points are of interest:

- The two-photon excitation of the glueball candidates $\eta(1440)$, $f_2(1720)$ and $\zeta(2220)$ is not observed. This qualitatively supports the glueball hypothesis, at

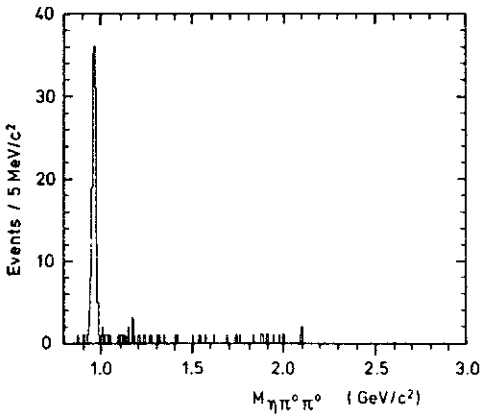

Figure 16: Invariant $\eta\pi^0\pi^0$ mass measured by the Crystal Ball in the 6γ final state [99]. The large peak is due to the $\eta'(958)$.

least in the case of the $\eta(1440)$ and $f_2(1720)$ which are copiously produced in J/ψ radiative decays.

- There is no hint for the two-photon production of a scalar resonance with isospin 0 such as the $f_0(975)$ or the $\epsilon(\sim 1300)$ (Fig.14).

- The $\eta(1275)$ resonance, which is supposed to be a radially excited η, was not seen in the $\eta\pi^0\pi^0$ final state (Fig.16). For this state a relatively large $\gamma\gamma$ width was predicted as discussed in [99].

- While the $KK\pi$ mass spectrum obtained from scattering of quasi-real photons (no tag) shows no indication for an $\eta(1440)$, the same spectrum shows an enhancement around 1420 MeV (Fig.17) if one of the photons is virtual (single tag) [108,109]. It is likely that this enhancement is due to an axial vector state ($J^{PC} = 1^{++}$) which cannot be produced by two real photons. Since the state observed in radiative J/ψ decays is certainly a pseudoscalar, there may be at least two states in the 1440 MeV region decaying into $KK\pi$, one being the $\eta(1440)$ and the other the $f_1(1420)$ seen in hadronic reactions.

The possibility of observing axial vectors and even states with exotic quantum numbers ($J^{PC} = 1^{-+}$) in $\gamma\gamma^*$ processes opens a new field in $\gamma\gamma$ spectroscopy [110]. The TPC/Two Gamma and the Mark II collaborations reported also first evidence for the observation of the $f_1(1285)$ [111].

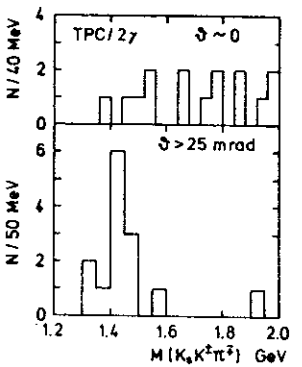

Figure 17: Mass distribution of the $K_S K^{\pm}\pi^{\mp}$ final state produced (a) by two quasi-real photons (no tag) and (b) by one quasi-real and one virtual photon (single tag) [107,108].

2.8 Vector Meson Pair Production

$\rho^0\rho^0$ production

The interest in two-photon production of vector meson pairs,

$$\gamma\gamma \rightarrow VV' \quad (V,V' = \rho,\omega,\phi).$$

has been stimulated by the observation of a huge cross section for the reaction $\gamma\gamma \rightarrow \rho^0\rho^0$ near threshold [112]-[116]. The measurements of four experiments on this reaction are summarized in Fig.18. The cross section is large near the nominal $\rho^0\rho^0$ threshold at about 1.55 GeV and stays high even below the threshold down to $W_{\gamma\gamma} \lesssim 1.3$ GeV. Since the available phase space for $\rho^0\rho^0$ production becomes very small below the nominal threshold the matrix element is rising extremely fast towards smaller $W_{\gamma\gamma}$. The energy dependence of the squared matrix element was estimated by the TASSO group to follow $W_{\gamma\gamma}{}^{-11.4}$ [114].

The two-photon production of $\rho^0\rho^0$ is observed in the four-pion final state

$$\gamma\gamma \rightarrow \rho^0\rho^0 \rightarrow \pi^+\pi^-\pi^+\pi^- \qquad (19)$$

Experimentally, the dominance of the $\rho^0\rho^0$ channel in the $\pi^+\pi^-\pi^+\pi^-$ final state is quite striking. This is demonstrated in Fig.19 for two different c.m. energy ranges of the four-pion system, one below the nominal $\rho^0\rho^0$ threshold and one above. Clear evidence for $\rho^0\rho^0$ production is seen in the correlation plot of the invariant masses of $\pi^+\pi^-$ pairs. Although below the nominal threshold the $\rho^0\rho^0$ peak cannot be reached kinematically the pronounced clustering near the kinematical boundary indicates clearly 'off-shell' $\rho^0\rho^0$ production.

The rapid energy variation of the matrix element for $\rho^0\rho^0$ production near threshold suggests an explanation by resonance formation. A $q\bar{q}$ resonance decaying into $\rho\rho$ has isospin I=0 with a decay branching ratio $\sigma(\rho^0\rho^0) : \sigma(\rho^+\rho^-) =$

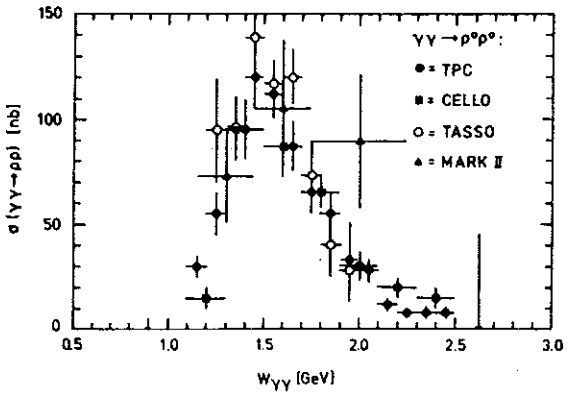

Figure 18: Compilation of the measured cross sections for $\gamma\gamma \to \rho^0\rho^0$ [113]-[116].

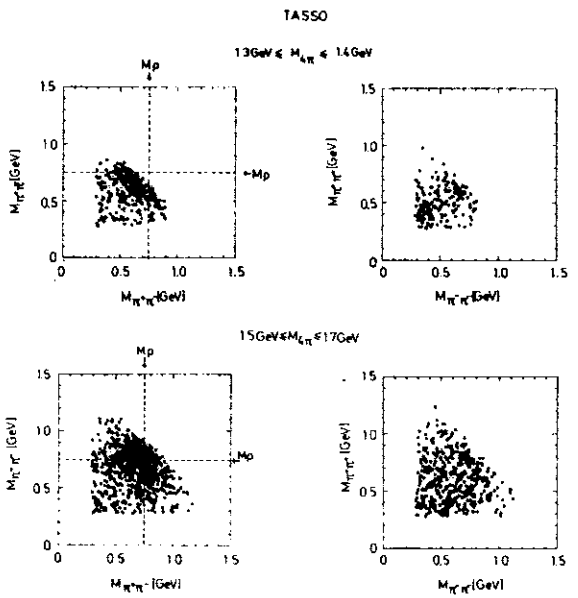

Figure 19: Scatter plot of $\pi\pi$ combinations in events with 4 charged pions in two different $M_{4\pi}$ intervals. The $\rho^0\rho^0$ enhancement is clearly visible in the unlike-sign mass combinations on the lefthand side.

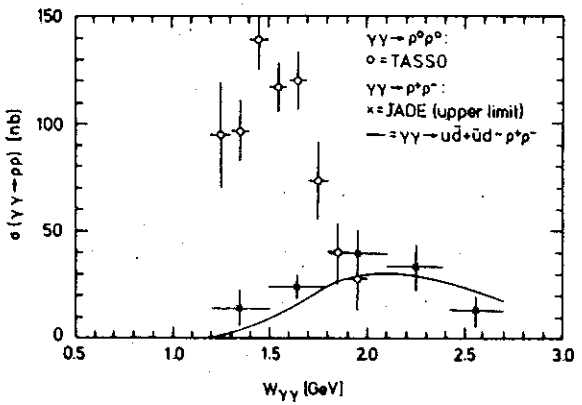

Figure 20: Cross section for $\gamma\gamma \to \pi^+\pi^-\pi^0\pi^0$ measured by JADE [117]. At least one $\pi^+\pi^0 - \pi^-\pi^0$ combination is required to be in the $\rho^+\rho^-$ band. The curve is a theoretical estimate of the $\rho^+\rho^-$ cross section [118]. Also shown is the cross section for $\gamma\gamma \to \rho^0\rho^0$ from TASSO [114].

1 : 2. The JADE group therefore searched for two-photon production of $\rho^+\rho^-$ [117]. Figure 20 shows the cross section for the reaction $\gamma\gamma \to \pi^+\pi^-\pi^0\pi^0$ with the additional requirement that the four-pion invariant mass is close to the $\rho^+\rho^-$ mass peak. Since no significant $\rho^+\rho^-$ signal was observed the data points have to be taken as upper limits for $\sigma(\gamma\gamma \to \rho^+\rho^-)$. Clearly, the $\rho^+\rho^-$ channel does not exhibit a similar threshold enhancement as $\rho^0\rho^0$. Thus it is ruled out that the $\rho^0\rho^0$ cross section near threshold can be explained by the formation of a simple resonance.

Models for vector meson pair production

A resonance interpretation of the $\rho^0\rho^0$ cross section can only be maintained by introducing two or more resonances which interfere differently in the charged and neutral ρ decay channels. The experimental facts can be quite naturally explained by a model with bound four-quark configurations, $qq\overline{qq}$ [9,10]. The spectroscopy of these states was worked out long before two-photon production of $\rho^0\rho^0$ was observed [119]. The spectrum contains nearly degenerate tensor states ($J^P = 2^+$) with isospin I=0 and I=2 which couple strongly to $\rho\rho$. By VDM arguments, they will have relatively large $\gamma\gamma$ widths and their two-photon production will proceed via intermediate ρ's. Decomposing the amplitude for two-photon production of ρ pairs into I=0 and I=2 amplitudes, A_0 and A_2, one finds that A_0 and A_2 enter with

different relative signs for the production of neutral and charged ρ's, respectively:

$$\begin{aligned} A(\gamma\gamma \to \rho^0\rho^0 \to \rho^0\rho^0) &= \tfrac{1}{3}A_0 + \tfrac{2}{3}A_2 \\ A(\gamma\gamma \to \rho^0\rho^0 \to \rho^+\rho^-) &= \tfrac{\sqrt{2}}{3}A_0 - \tfrac{\sqrt{2}}{3}A_2 \end{aligned} \qquad (20)$$

In the four-quark model A_0 and A_2 are in first approximation equal, resulting in a suppression of the $\rho^+\rho^-$ final state. This was firmly predicted as a necessary consequence from the four-quark model before the JADE upper limits on the reaction $\gamma\gamma \to \rho^+\rho^-$ were available [7]. An estimate of the non-resonant $\gamma\gamma \to \rho^+\rho^-$ cross section and the nearby $(\pi^+\pi^0) + (\pi^-\pi^0)$ continuum can be obtained [118] by extrapolating the perturbative QCD calculation of the non-diffractive process $\gamma\gamma \to (u\bar{d}) + (\bar{u}d)$ down to the $\rho\rho$ threshold region, see the curve in Fig.20.

The binding potential of four-quark states is expected to be small. Therefore they should easily fall apart into the $q\bar{q}$ components they are made of (superallowed decays) and as a consequence, they would be very broad and difficult to discover. However, those states lying below the threshold for their superallowed decays may have relatively narrow widths. E.g., the pseudoscalar mesons $a_0(980)$ and $f_0(975)$, just below the $K\bar{K}$ threshold, have been interpreted as four-quark states with superallowed decays into $K\bar{K}$. Similarly the $\rho^0\rho^0$ cross section may be explained by four-quark states just below the nominal $\rho^0\rho^0$ threshold.

Four-quark resonances are also predicted in the $\rho^0\omega$ and $\rho^0\phi$ channels. The cross section for $\gamma\gamma \to \rho^0\omega$ was recently measured by the ARGUS group [120] (Fig.21). The cross section is largest around 1.9 GeV and falls down rather sharply above. The low mass part containes the expected contribution from a_2 formation. The remaining cross section cannot be explained by a threshold enhancement as expected either from the four-quark model [9] or a t-channel factorization model [121,122]. An additional contribution is required around 1.9 GeV.

The TPC/Two-Gamma and the TASSO groups searched for two-photon production of $\rho^0\phi$ [123]. Both groups found no significant signal from this reaction. These measurements were not really at variance with the four-quark model, mainly because there is some freedom in the choice of parameters such as masses and branching ratios into other than the superallowed channels. However, a preliminary upper limit from ARGUS [124] seems to exclude all physically reasonable parameter sets.

The ARGUS group provided also the first measurements of two-photon production of $\omega\omega$ (Fig.22) and $K^{*0}\overline{K^{*0}}$ (Fig.23) [124]. Both reactions show threshold enhancements which are much larger than expected from the four-quark model. Taking VDM as a guide $\omega\omega$ production should be suppressed by a factor 1/81 compared to $\rho^0\rho^0$, i.e. the cross section should be in the 1 to 2 nb range. No satisfactory quantitative explanation for the enhancements in both channels have been given so far.

In a more conservative approach, t-channel exchange mechanisms were proposed to explain the $\rho^0\rho^0$ threshold enhancement [121,122]. These contributions

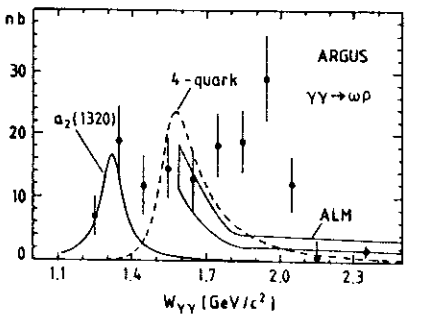

Figure 21: Cross section for $\gamma\gamma \to \rho^0\omega$ measured by ARGUS [120]. The data are compared to the four-quark model [9] and a t-channel factorization model [122]. Shown is also the expected $a_2(1320)$ contribution in this channel.

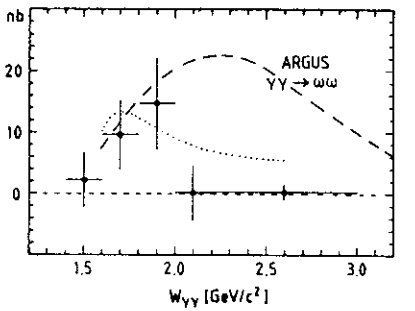

Figure 22: Cross section for $\gamma\gamma \to \omega\omega$ [124] compared to predictions of a t-channel factorization model (dashed curve [122]) and of a one-pion-exchange model (dotted curve [125]). The four-quark model predicts about 1/18 of the $\rho\omega$ cross section (Fig.21) [7].

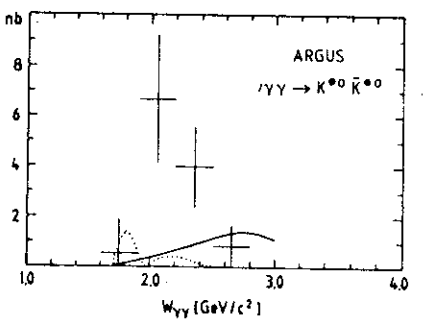

Figure 23: Cross section for $\gamma\gamma \to K^{*0}\overline{K^{*0}}$ [124]. The dotted curve is the four-quark model prediction [7] and the full curve is an estimate of non-resonant background from $\gamma\gamma \to (s\bar{d}) + (\bar{s}d)$ [118].

to the $\gamma\gamma$ cross section have been related to photoproduction and nucleon-nucleon scattering cross sections. However, the extrapolation of the factorized amplitudes from high to low energies in the threshold region is not unambiguous. Nevertheless, these attempts demonstrate that conventional explanations of the large $\rho^0\rho^0$ cross section are not yet ruled out.

Analysis of angular distributions in $\gamma\gamma \to \rho^0\rho^0$

The four-quark model makes the definite prediction that states coupling to vector mesons near threshold have spin-parity 2^+. The TASSO [114] and CELLO [115] collaborations analyzed the angular distributions of the four-pion final state in reaction (19). In the notag case, i.e. if the lepton scattering plane is not measured, the four-pion final state is described by 7 variables. One can choose as variables two $\pi^+\pi^-$ masses, the ρ production angle and two angles for each decaying ρ. For the angular correlation analysis the TASSO group defined the following matrix element for two-photon production of $\rho^0\rho^0$ via a state with spin-parity J^P and $\gamma\gamma$ helicity J_z:

$$g_{\rho\rho}^{J^P J_z} = \frac{1}{\sqrt{2}}\left[BW(12)BW(34)\Psi^{J^P J_z}(12,34) + BW(14)BW(32)\Psi^{J^P J_z}(14,32)\right]$$

In this ansatz the mass dependence is contained in the ρ Breit-Wigner amplitudes BW and the angular correlations in the function $\Psi^{J^P J_z}$. The matrix element is symmetric with respect to the interchange of identical bosons in the final state. The indices 12, 34 and 14, 32 refer to the two possibilities to form $\rho^0\rho^0$ out of the four pions.

In order to obtain the spin-parity decomposition of $\rho^0\rho^0$ production in Fig.24 the TASSO group fitted the four pion final state with a sum of non-interfering spin-parity states ($J^P = 0^+, 0^-, 2^+, 2^-$) and additional contributions from $\rho^0\pi^+\pi^-$ and $\pi^+\pi^-\pi^+\pi^-$ phase space. According to the fits the negative parity states $J^P = 0^-$ and 2^- are not dominant in the investigated $W_{\gamma\gamma}$ range. The $\rho^0\rho^0$ cross section is essentially built up by the positive parity states, with $J^P = 0^+$ dominating in the threshold region.

The dominance of 0^+ in the threshold region is in obvious disagreement with the four-quark model. However, some words of caution have to be added concerning especially the region below the nominal $\rho^0\rho^0$ threshold. The results have been obtained with a special choice of the matrix elements as described above. E.g., effects from final state interactions, which could be strong at low energies were not included. Since the 0^+ and 2^+ angular distributions are very similar within the acceptance (due to the holes in the beam directions) it seems safer to consider only the sum of both contributions. Thus the TASSO analysis proves unambiguosly only that the $\rho^0\rho^0$ channel, if dominated by one spin-parity amplitude, must have positive parity. Experiments with a better acceptance in the forward direction

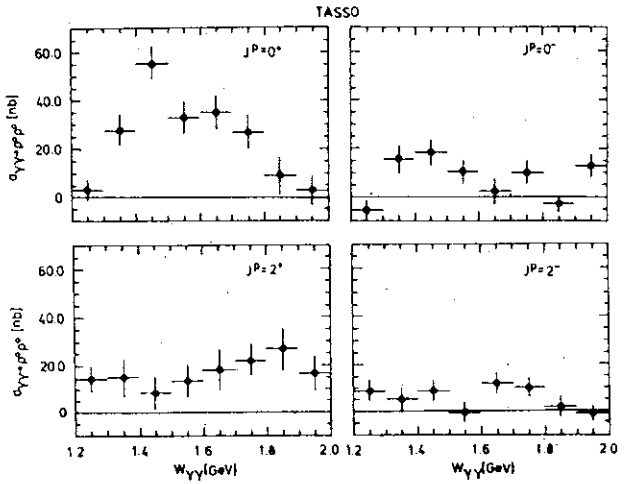

Figure 24: Spin-parity decomposition of the cross section for $\gamma\gamma \to \rho^0\rho^0$ assuming contributions from $J^P = 0^+, 0^-, 2^+(\lambda = 2), 2^-$ [114].

than the TASSO detector should have a better chance to separate 0^+ and 2^+ contributions.

The Cello group made an effort to analyze $\rho^0\rho^0$ production, including the angular distributions, in a more model independent way. They applied acceptance corrections as a function of the four possible $\pi^+\pi^-$ masses. This is an approximation since the final state depends on 7 variables.

With this method the topological cross section for $\gamma\gamma \to \pi^+\pi^-\pi^+\pi^-$ has been determined independent of the individual subprocesses contributing to this final state (Fig.25). The $\rho^0\rho^0$ cross section, also shown in Fig.25, was determined by assuming, as in the TASSO analysis, that the four pion final state can be described by a sum of non-interfering contributions from $\rho^0\rho^0$, $\rho^0\pi^+\pi^-$ and $\pi^+\pi^-\pi^+\pi^-$ phase space production (Fig.25). Besides a prominent threshold enhancement in the $\rho^0\rho^0$ channel CELLO also finds sizeable $\rho^0\pi^+\pi^-$ and $\pi^+\pi^-\pi^+\pi^-$ phase space production. In contrast to $\rho^0\rho^0$ production the two latter final states behave smoothly in the measured $W_{\gamma\gamma}$ range.

Analyzing the angular distributions of the $\rho^0\rho^0$ channel the CELLO group studied the spin density matrix elements of the ρ's as a function of the ρ production angle θ_ρ. The spin density matrix was evaluated in the helicity system of each ρ, i.e. using as the quantization axis the direction of flight of the ρ's. Combining the data in a $W_{\gamma\gamma}$ range from 1.3 to 2.3 GeV the CELLO group finds that for $|cos\theta_\rho| < 0.8$

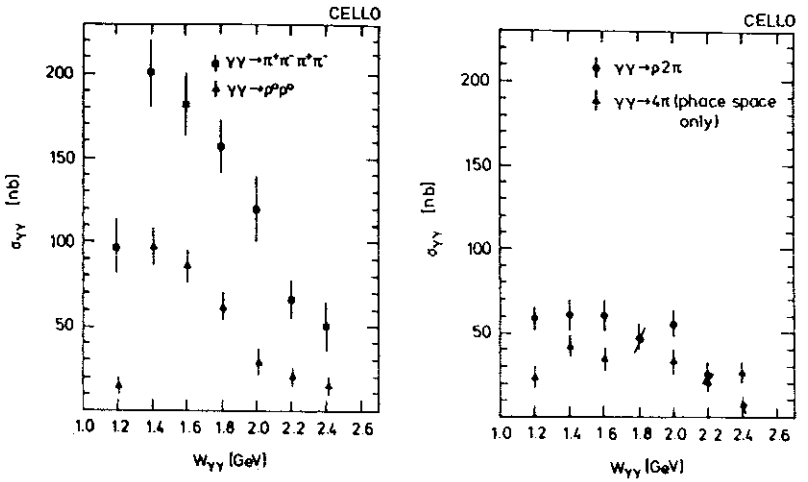

Figure 25: Cross section for $\gamma\gamma \to \pi^+\pi^-\pi^+\pi^-$ including all four pion final states (squares) and seperately for $\gamma\gamma \to \rho^0\rho^0$, $\gamma\gamma \to \rho^0\pi^+\pi^-$ and $\gamma\gamma \to \pi^+\pi^-\pi^+\pi^-$ (phase space only) [115].

no helicity state is preferred, while in the forward direction, $|cos\theta_\rho| > 0.8$, the helicities ± 1 of the ρ's dominate.

It can be concluded that the data are consistent with a helicity conserving process as in diffractive scattering. However, this analysis does not exclude $J^P = 2^+$, $J_z = 2$ resonance formation.

Summary of vector meson pair production

Summarizing our discussion of two-photon production of vector meson pairs following points should be emphasized:

- The cross section of $\rho^0\rho^0$ production exhibits a strong threshold enhancement with an energy dependence of the squared matrix element following approximately $W_{\gamma\gamma}{}^{-11}$. The $\rho^+\rho^-$ production near threshold is smaller by at least one order of magnitude.

- The four-quark model explains the large difference between the $\rho^0\rho^0$ and $\rho^+\rho^-$ cross sections as an interference effect between $I = 0$ and $I = 2$ resonances in a natural way. However, more conventional approaches cannot yet be ruled out.

- The observed angular distributions in the $\rho^0\rho^0$ final state are consistent with positive parity. The spin-parity $J^P = 2^+$ state required by the four-quark model

is not established. Crucial tests for the existence of four-quark resonances will be provided by refined spin-parity analyses of the final states $\rho^0\rho^0$ and $\rho^0\omega$.

- The small experimental upper limits on $\rho^0\phi$ production cause serious problems for the four-quark model.

- The two-photon production of $\rho\omega$, $\omega\omega$ and $K^{*0}\overline{K^{*0}}$ is apparently more complex as to be accounted for by any single model.

The $I = 2$ $\rho\rho$ resonance predicted by the four-quark model can also be searched for in hadron-hadron interactions, e.g. $pp \to \rho^+\rho^+nn$ [9].

3 The Total Cross Section for Hadron Production by Two Photons

3.1 Introduction

Hadron production in $\gamma\gamma$ collisions proceeds through a superposition of several mechanisms. After a high energy photon has split into a $q\bar{q}$ pair with small relative transverse momentum, the lifetime of this state is long enough to allow for its binding to a vector meson. The cross section for the subsequent vector-meson vector-meson collisions, Fig.26a, will carry all the standard characteristics of strong

Figure 26: a) VDM mechanism for hadron production by two photons and b) by direct quark exchange.

interaction processes. Other microscopic mechanisms with different characteristics might also contribute to the $\gamma\gamma$ cross section. In particular hadron production at large transverse momenta proceeds through short-lived $q\bar{q}$ states for which the dominating diagram is shown in Fig.26b. Mixing between a) and b) complicates the picture even more.

With our experience from other photon - hadron reactions we expect that hadron production by two quasi-real photons proceeds mainly via vector meson - vector meson scattering (Fig.26a). With the probability $\alpha\pi/\gamma_V^2$ for a photon to turn into a vector meson one gets the VDM relation

$$\sigma(\gamma\gamma \to hadrons) = \sum_{V,V'} \frac{\alpha\pi}{\gamma_V^2}\frac{\alpha\pi}{\gamma_{V'}^2}\sigma(VV' \to hadrons) \qquad (21)$$

$$\frac{\alpha\pi}{\gamma_\rho^2} = 2.80\cdot 10^{-3};\ \frac{\alpha\pi}{\gamma_\omega^2} = 0.30\cdot 10^{-3};\ \frac{\alpha\pi}{\gamma_\phi^2} = 0.36\cdot 10^{-3}.$$

The $W_{\gamma\gamma}$ dependence of the two-photon cross section for hadron production can be predicted in the framework of the Regge model [13]. Using the factorization hypothesis the two-photon cross section is related to measured hadron - hadron and photon - hadron cross sections,

$$\sigma_{\gamma\gamma} = (240 + \frac{270\ GeV}{W_{\gamma\gamma}})\ nb \quad \text{(Regge exchange)}. \qquad (22)$$

The constant term corresponds to pomeron exchange and the $1/W_{\gamma\gamma}$ term to f_2 and a_2 exchange. The second term should be dual to s-channel resonance production at low $W_{\gamma\gamma}$.

The direct quark exchange mechanism (Fig.26b) is expected to add only little to the total cross section, though it may well be dominant in kinematical regions involving high momentum transfers. In lowest order the $W_{\gamma\gamma}$ dependence of this contribution is described by the scaling law

$$\sigma_{\gamma\gamma} \sim \frac{1}{W_{\gamma\gamma}^2} \quad \text{(quark exchange)}. \qquad (23)$$

While this mechanism will lead at large angles to hard scattering phenomena like high p_T hadron and jet production, the VDM cross section is dominated by peripheral processes leading to hadron production with limited transverse momenta with respect to the $\gamma\gamma$ direction. The typical p_T dependence in hadronic reactions is

$$\frac{d\sigma}{dp_T^2} \sim e^{-6p_T} \qquad (p_T\ in\ GeV). \qquad (24)$$

3.2 Experimental Methods

The experimental determination of the total two-photon cross section turns out to be more difficult than, e.g., the measurement of exclusive final states. That is mainly because the trigger efficiencies depend strongly on the topology of the final state which is a priori unknown. Thus modelling the hadronic final state is the most important task in measurements of the total cross section.

In such models the dominant VDM part is represented by a limited p_T phase space model with a p_T dependence similar to (24). The average charged multiplicity, which can be assumed to have a logarithmic $W_{\gamma\gamma}$ dependence, the ratio of charged to neutral particle production and the p_T slope are usually adjusted to the data. However, often one may be forced to make some assumptions about the input parameters because the correlations between the model parameters may be too strong otherwise (see also the discussion in [117]).

In the notag and single-tag mode an additional complication arises from the fact that the $W_{\gamma\gamma}$ distribution of the measured events has to be inferred from the, in general, incompletely observed hadrons. The invariant mass of the observed hadrons ($= W_{vis}$) is generally smaller than the true $W_{\gamma\gamma}$. In the double-tag mode the $W_{\gamma\gamma}$ value of an event can in principle be inferred from the tagging kinematics. However, the resolution, in particular for low $W_{\gamma\gamma}$ is often not sufficient so that also in this case some unfolding of the $W_{\gamma\gamma}$ distribution may be necessary.

The basic quantity to be measured is the total cross section for real photons, i.e. one has to restrict the experiment to real (or quasi-real) photons or one has to make an extrapolation. Both approaches have been tried in different experiments. In notag experiments essentially a real photon cross section is measured but one has to cope with the problem of one-photon annihilation background. The other possibility, double-tag at 0°, is only possible in specialized detectors. Here one has

to fight the background from bremsstrahlung and small angle Bhabha scattering hitting the tagging devices. The method most often used is tagging at finite angles and extrapolation to the real-photon case.

While for unpolarized real photons only the cross section term σ_{TT} in (5) remains, for photons tagged at finite angles the structure of the cross section becomes quite complicated. The task of disentangling all terms has not been attacked yet, and it appears to be too difficult at the moment. Instead, the cross section can be simplified by assuming that the longitudinal part of untagged photons can be neglected. Hence, in the single-tag case the following effective cross section is measured:

$$\sigma^{eff}_{\gamma\gamma}(W_{\gamma\gamma}, Q_1^2) \;=\; \sigma_{TT}(W_{\gamma\gamma}, Q_1^2, 0) \;+\; \epsilon \cdot \sigma_{LT}(W_{\gamma\gamma}, Q_1^2, 0) \qquad (25)$$

where Q_1^2 refers to the tagged photon. In most cases the polarization parameter ϵ is close to 1.

To extrapolate (25) to the real photon cross section a model for the Q^2 dependence of $\sigma^{eff}_{\gamma\gamma}$ is needed. Using the generalized VDM model (GVDM) [126] the following Q^2 dependence was suggested [127]:

$$F^{GVDM}(Q^2) \;=\; \sum_{V=\rho,\omega,\phi} r_V \frac{1+Q^2/4m_V^2}{(1+Q^2/m_V^2)^2} \;+\; \frac{0.22}{1+Q^2/m_0^2} \qquad (26)$$

$$r_\rho = 0.65,\; r_\omega = 0.08,\; r_\phi = 0.05,\; m_0 = 1.4\ GeV.$$

This expression accounts for the Q^2 behavior of σ_{LT} by the term $Q^2/4m_V^2$. Contributions from higher mass vector mesons and from the continuum are approximated by the last term in the sum. At low and medium Q^2 GVDM seems to describe the data better than, e.g., a simple ρ pole form factor (see Fig.27).

3.3 The Total Cross Section at Low Q^2

Figure 28 summarizes our present knowledge on the $W_{\gamma\gamma}$ dependence of the two-photon total cross section. Earlier measurements (see e.g. [117]) are probably superseded by these latest results. The plots a) and b) in Fig.28 show cross sections obtained by the PLUTO [129] and PEP-9 [128] groups by tagging at low Q^2. PLUTO required a single- tag with $< Q^2 >$=0.44 GeV^2 and PEP-9 a double-tag with $< Q^2 >$=0.3 GeV^2. In both plots the scales on the left side give the effective cross section for the average Q^2 of the tagged photons. The scales on the right side present the values extrapolated to Q^2=0 by means of the $W_{\gamma\gamma}$ independent GVDM formula (26). Figure 28c shows preliminary results from an experiment which avoided the extrapolation to Q^2=0. The measurements are made by the MD-1 group at the VEPP-4 storage ring in a double-tag experiment [130]. The MD-1 detector has a tagging acceptance down to 0°, corresponding to nearly real photons.

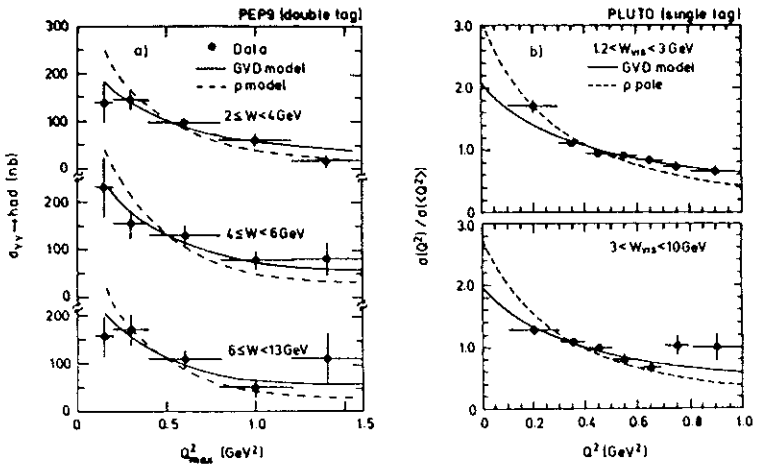

Figure 27: Q^2 dependence of $\sigma(\gamma\gamma \to hadrons)$ at small Q^2 for different W_{vis} ranges. The data are from PEP-9 [128] and PLUTO [129]. The double-tag data in a) are plotted versus the larger of the two Q^2 values.

All measurements consistently approach a constant cross section at large $W_{\gamma\gamma}$ which may be somewhat higher than the prediction (22):

$$\sigma_{\gamma\gamma}(W_{\gamma\gamma} \to \infty) \;\approx\; 300\ nb \qquad \text{(exp.)}. \qquad (27)$$

At low $W_{\gamma\gamma}$ the situation is experimentally not yet settled. While the PEP-9 data are consistent with a constant cross section between 2 and 20 GeV the other measurements develop a slope which can be described by a $1/W_{\gamma\gamma}$ term and which seems to be even larger than predicted by (22). A $1/W_{\gamma\gamma}{}^2$ term, however, is not required by any measurement. The PLUTO and MD-1 data are well reproduced by the model [131] (AMM). In this model the factorization ansatz is not only employed for real but also for virtual photoproduction data. This leads to a Q^2 behavior which is $W_{\gamma\gamma}$ dependent so that in Fig.28 the model can only be compared to the actually measured, effective cross section. An even better description of the PLUTO data is achieved by the model of [132] which differs from the previous models in that it uses forward elastic scattering amplitudes as input and relates them to the total cross sections via the optical theorem. The differences between the models are most pronounced at low $W_{\gamma\gamma}$ where the measurements are most difficult and the systematic uncertainties largest. Therefore it appears premature to judge the quality of the models on the basis of the available data.

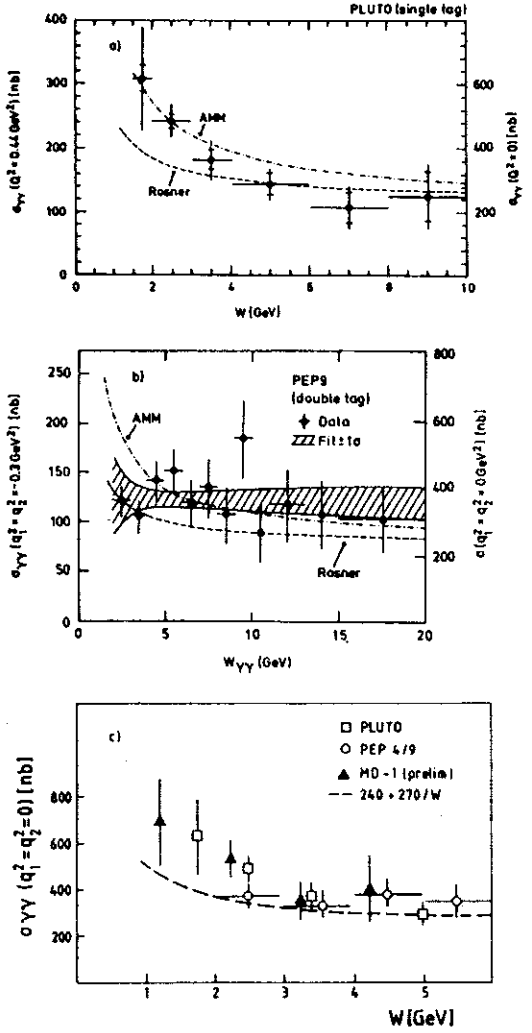

Figure 28: $W_{\gamma\gamma}$ dependence of $\sigma(\gamma\gamma \rightarrow hadrons)$ at small Q^2: a) PLUTO (single tag); b) TPC/Two-Gamma (double tag); c) MD-1 (0^- double tag). The scales on the right side of a) and b) are an extrapolation to Q^2=0 using the GVDM formula.

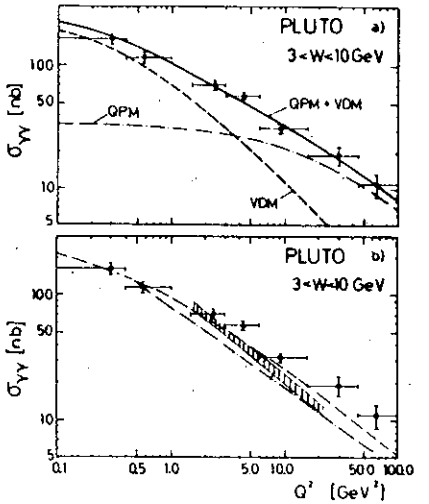

Figure 29: Large Q^2 behavior of $\sigma(\gamma\gamma \rightarrow hadrons)$. The curves in b) are from [134] (dashed), [135] (dashed-dotted) and [131] (shaded).

3.4 The Total Cross Section at large Q^2

The PLUTO group determined the two-photon total cross section for Q^2 values up to 100 GeV^2 in a single tag experiment [133]. Figure 29a shows the Q^2 dependence of the effective cross section averaged over the $W_{\gamma\gamma}$ range from 3 to 10 GeV. At high Q^2 the GVDM curve (labelled VDM) clearly falls off much steeper than the data. The quark-parton model (QPM) curve, i.e. the contribution of the Born diagram (Fig.26a) with an "effective light quark mass" of 300 MeV, has a less steep Q^2 dependence but does not describe the data at low Q^2 . The sum of both, however, fits the data surprisingly well over the whole Q^2 range.

In Fig.29b the PLUTO data are compared to two predictions using the extended vector meson dominance model (EVDM) [134,135] and the factorization model [131] mentioned before. The EVDM describes the photon as a superposition of an infinite number of vector meson states. The Q^2 dependence of deep-inelastic ep data and e^+e^- one-photon annihilation data have been successfully modelled by EVDM. In these cases the model can be connected to QPM by a duality relation. In two-photon reactions this duality seems not to hold. None of the curves in Fig.29b describes the data over the whole Q^2 range. This failure indicates that the pointlike coupling of the two photons cannot be simulated by hadronic mechanisms even if an infinite number of vector meson states is excited. This issue has been discussed in more detail in [136]. The role of the pointlike coupling of the photons, related to asymptotic-freedom in quantum chromodynamics, becomes more obvious when the cross section is described in terms of the photon structure functions as will be discussed in the next section.

4 The Photon Structure Functions

Quantum chromodynamics is based on high energy e^+e^- collider experiments besides deep inelastic lepton-nucleon scattering and large-p_T phenomena in hadron-hadron colliders. The observation of 3-jet topologies at PETRA energies provides the most direct evidence for the existence of gluons. Hadronic jets, however, are fuzzy objects and their structure is theoretically ill-understood. The problems encountered in numerical solutions of QCD when spontaneous quark-pair creation is incorporated, indicate that the dynamical built-up of jets will very likely not be solved in the near future. This renders the measurements of the quark-gluon coupling constant α_s by means of final state analyses in e^+e^- annihilation a difficult task. The determination of α_s from the QCD correction to the total cross section is a theoretically much cleaner method. However, since the correction is small, this method suffers from experimental calibration uncertainties.

Deep inelastic electron-photon scattering offers a complementary method to investigate QCD in e^+e^- collisions. This process has had a long theoretical history [2] - [6] before first measurements were reported [137]. The physical interest in the analysis of the photon structure function is related to the following key points:

- The structure function rises linearly with $\log Q^2$ in leading order QCD [3]. The slope is predicted by QCD [4,138,139]. Relative to the quark parton model prediction it is altered asymptotically to O(1) by gluon bremsstrahlung [4]. This linear rise is a consequence of asymptotic freedom for large Q^2. Gluon bremsstrahlung with a fixed coupling constant would result in an asymptotically scale-invariant photon structure function, not rising with Q^2 anymore for x above zero [140].

- In next-to-leading order [6] the absolute size of all moments of F_2^γ with N>2 is asymptotically fixed by the QCD parameter Λ. A spurious singularity at N=2 is not expected to spread to large N values [5] as can be inferred from electron scattering on off-shell photons that is completely calculable perturbatively [141] (Higher orders can only be calculated for still larger N values [142] since the non-perturbative remnants of the structure function have to fall off faster than the perturbative component).

When this QCD analysis is applied to medium range Q^2 values, supplementary assumptions on the residual non-perturbative part of the structure function are needed. These assumptions are beyond the realm of perturbative QCD calculations and must therefore be subject to experimental scrutiny. The $e\gamma$ experiments carried out till now, in fact provide a consistent picture. Increasing statistics of forthcoming analyses should hopefully pacify the (natural) theoretical controversy [143,144] on the validity of those mild assumptions.

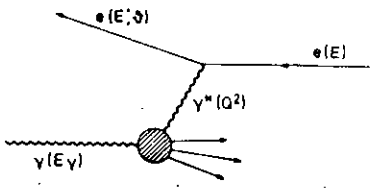

Figure 30: Kinematics in deep- inelastic $e\gamma$ scattering

4.1 Definition of the Photon Structure Functions

The cross section for deep-inelastic electron scattering off a photon target (Fig.30) is parametrized by two structure functions [2,145] :

$$\frac{d\sigma}{dxdy} = \frac{16\pi\alpha^2 EE_\gamma}{Q^4}\left[(1-y)F_2(x,Q^2) + y^2 xF_1(x,Q^2)\right]. \tag{28}$$

F_1 and F_2 are proportional to the cross sections for transversely and longitudinally polarized virtual photons

$$F_1 = F_T \tag{29}$$
$$F_2 = 2xF_T + F_L$$

The momentum transfer $q^2 = -Q^2$ and the energy tranfer $\nu = qp_\gamma$ can be expressed in terms of the energy of the target photon E_γ, the electron energies E, E' before and after the collision and the scattering angle ϑ in the laboratory system:

$$Q^2 = 4EE'\sin^2\frac{\vartheta}{2} \tag{30}$$

$$\nu = 2E_\gamma(E - E'\cos^2\frac{\vartheta}{2})$$

The invariant final-state hadron energy W is determined by ν and Q^2

$$W^2 = 2\nu - Q^2$$

and the Bjorken variable x and y are related to these observables by

$$x = \frac{Q^2}{2\nu} = \frac{Q^2}{Q^2 + W^2} \tag{31}$$

$$y = \frac{\nu}{kp_\gamma} = 1 - \frac{E}{E'}\cos^2\frac{\vartheta}{2}$$

The coefficient y^2x in (28) is very small under normal experimental conditions so that only $F_2(x,Q^2)$ can be measured.

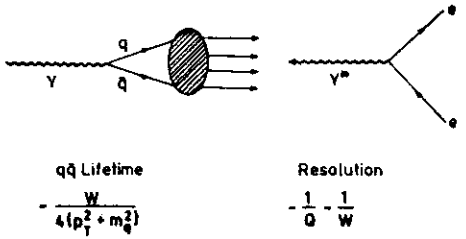

Figure 31: Space-time picture of deep-inelastic $e\gamma$ scattering

4.2 QCD Prediction of the Structure Functions

The theory of the photon structure functions had been gradually developed over a decade before deep-inelastic electron-photon scattering became experimentally accessible at the high-energy e^+e^- colliders PETRA and PEP. The important qualitative features of the experimental results conform with the theoretial predictions - a non-trivial test of QCD. Higher statistics, however, is certainly needed to improve the accuracy of the data, necessary to scrutinize the theoretical assumptions when the Λ parameter is extracted from the absolute size of the structure function F_2.

Setting the stage: The quark-parton model

The space-time analysis of electron-photon scattering [146] reveals the complex nature of this reaction. Depending on the transverse momentum of the quark in the photon splitting process, two different components can be distinguished (Fig.31).

- For small transverse momenta $< O(\Lambda)$, the lifetime of the quark-antiquark pair is long and the overlap with the low-lying resonances ρ, ω, ϕ is large. This defines the VDM component of the photon. Adopting counting rule arguments and attributing half of the vector-meson momentum to quarks, the quark density is taken to be $\approx \frac{1}{2}(1-x)/x$. This parametrization is backed up nicely by measurements of quark and gluon densities in pions [147]. Adding up the light-quark contributions (ρ and ω coherently) results in the following estimate of the VDM components of the photon structure function [140,148]:

$$F_2^{\rm VDM}(x, Q^2 \sim 10\,{\rm GeV}^2) = \alpha(0.20 \pm 0.05)(1-x). \qquad (32)$$

This form applies to $Q^2 \sim 10\,{\rm GeV}^2$. The VDM component decreases with rising Q^2 for $x \geq 0.2$ similarily to the nucleon structure function.

- If the transverse momentum of the quark in the photon splitting process is large, $> O(\Lambda)$, the lifetime of the $q\bar{q}$ state becomes so short that the pair cannot couple to a vector meson anymore and the virtual photon is absorbed directly by one of the primary quarks. Neglecting gluon bremsstrahlung, this direct component is given in the parton approach by [3]:

$$F_2^{\rm PART} = \frac{\alpha < e^4 >}{\pi} x\left[x^2 + (1-x)^2\right] \log Q^2 \qquad (33)$$

$$F_L^{\rm PART} = \frac{4\alpha < e^4 >}{\pi} x^2(1-x) \qquad (34)$$

where $< e^4 > = 3\sum e^4$, the sum running over all quark flavors. The leading part of F_2 is linear in $\log Q^2$, while F_L is asymptotically finite and scale invariant. This is due to the unlimited transverse momentum in the splitting $\gamma \to q\bar{q}$, leading to

$$F_2^{\rm PART} \sim \int^{Q^2} \frac{dp_T^2}{p_T^2} \qquad \text{and} \qquad F_L \sim \int^{Q^2} \frac{dp_T^2}{p_T^2} \cdot \left(\frac{p_T^2}{Q^2}\right)$$

due to helicity conservation. The lower limit, apart from being $O(\Lambda^2)$, is not well defined in the present intuitive approach since the sharp division of the transverse momentum spectrum into a purely perturbative and a purely nonperturbative domain oversimplifies the physical reality. The normalization problem in (33) can unambiguously be solved if use is made of the operator product expansion of the currents and the renormalization group equations for the moments of the structure functions.

The contribution of heavy quarks to the photon structure function is well described by the quark-parton model. The production process extends only over a distance of the order of the Compton wave length of the heavy quark and gluon bremsstrahlung is suppressed, so that the zeroth order QCD calculation is adequate. In the PETRA/PEP energy range only charm quarks give a sizable contribution [149] as presented in Fig.32:

$$\begin{aligned} F_2^c &= \frac{3\alpha e_c^4}{\pi}\left\{ vx\left[4x(1-x)(2-\frac{m^2}{Q^2}) - 1\right] + \right. \\ &\left. \left[x^2 + (1-x)^2 + \frac{4m^2}{Q^2}x(1-3x) - \frac{8m^4}{Q^4}x^2\right] \log\frac{1+v}{1-v}\right\} \qquad (35) \\ F_L^c &= \frac{12\alpha e_c^4}{\pi}\left\{ vx^2(1-x) - \frac{2m^2}{Q^2}x^3 \log\frac{1+v}{1-v}\right\}, \end{aligned}$$

v denotes the quark velocity in the c.m. system. The Coulombic gluon rescattering corrections rendering F_2^c non-zero at threshold are restricted to a small domain near $x \leq Q^2/(Q^2+4m^2)$. The production of b quarks is doubly suppressed by the higher mass as well as the reduced electric charge, $e_b^4/e_c^4 = 1/16$.

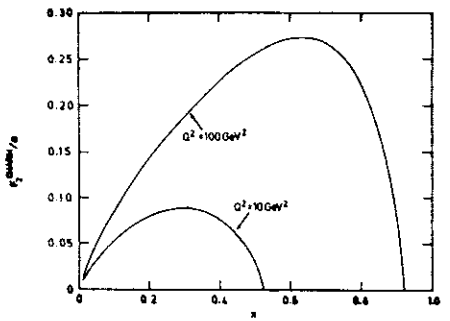

Figure 32: Charm contribution to the photon structure function.

Leading order QCD

After switching on perturbative gluon radiation (Fig.33), three mechanisms compete with each other to build up the structure function F_2^γ in the leading order. With rising Q^2,

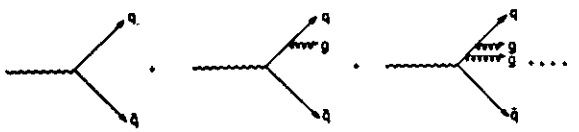

Figure 33: Changing the quark spectrum by perturbative gluon bremsstrahlung.

- the number of quarks rises at the position x due to the increasing $\gamma \to q\bar{q}$ splitting probability;

- at $x \geq 0.4$ quarks are lost due to increasing gluon radiation (the quarks accumulate at small x);

- gluon radiation is damped as a consequence of the logarithmically decreasing coupling constant.

The net effect, after solving the Altarelli-Parisi equations asymptotically for quark and gluon densities ($t = \log \frac{Q^2}{\Lambda^2}$)

$$\begin{aligned} \frac{\partial q}{\partial t} &= \frac{\partial q^{\mathrm{BORN}}}{\partial t} + \frac{\alpha_s}{2\pi}\left[P_{qq} * q + P_{qg} * g\right] \\ \frac{\partial g}{\partial t} &= \frac{\alpha_s}{2\pi}\left[P_{gq} * q + P_{gg} * g\right] \end{aligned} \tag{36}$$

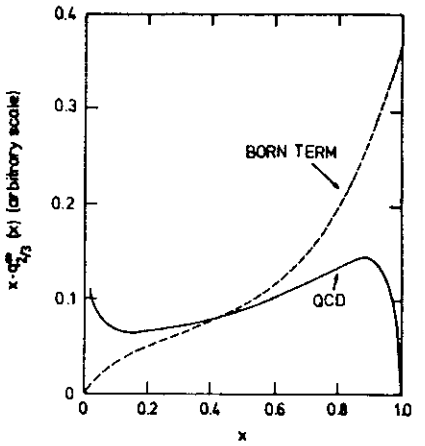

Figure 34: $O(1)$ change of the photon structure function when perturbative gluon bremsstrahlung is switched on, exemplified for the u-quark spectrum.

is a structure function that keeps rising linearly in $\log Q^2/\Lambda^2$ but with an $O(1)$ change of the coefficient (Fig.34) [4,138,139]:

$$\begin{aligned} q(x,Q^2) &= d(x)^{\mathrm{BORN}} \log Q^2 \\ &\to d(x) \log Q^2 \end{aligned} \tag{37}$$

(QCD corrections to F_L turn out to be numerically small).

The kinematical increase of the gluon bremsstrahlung with Q^2 is just balanced in QCD by the decrease of the running coupling constant, resulting in a uniform rise of F_2^γ with $\log Q^2$. This is a characteristic consequence of asymptotic freedom that can be illuminated by confronting QCD to a toy model in which the coupling constant α_s is frozen at $Q_0^2 = 5\,\mathrm{GeV}^2$ with $\Lambda = 200\,\mathrm{MeV}$. In such a case, gluon bremsstrahlung moves the increasing number of quarks in the $\gamma \to q\bar{q}$ splitting process all down to small x values. For finite $x > 0$ the structure function becomes asymptotically scale-invariant at a magnitude of order α/α_s [140]. This is illustrated in Fig.35 for the moment $\int dx\, x^2 F_2(x,Q^2)$. As expected a large lever arm in Q^2 is needed, stretching to the upper range where LEP200 will be operating [150], to find the deviation of such a model from canonical QCD with a running coupling constant.

QCD in next-to-leading order

The physically intuitive ideas described in the first subsection are cast into a rigorous field-theoretic framework by turning on the machinery of the operator product expansion and renormalization group equations. This analysis has been

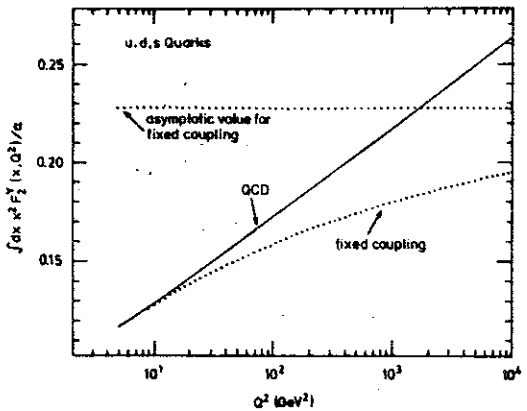

Figure 35: Q^2 evolution of the photon structure function in QCD confronted with a fixed-coupling model.

completed to leading- and next-to-leading orders [6,5] in which the dependence of the absolute scale of the structure function on the QCD parameter Λ is properly defined. The solutions of the renormalization group equations for the moments of the structure functions require, however, too many poorly known experimental input data as to be rigorously exploitable. Instead, elements of the intuitive ideas described earlier are necessary to allow, for example, a determination of Λ.

Defining the moments of the structure function as

$$F_2^N(Q^2) = \int_0^1 dx x^{N-2} F_2(x,Q^2),$$

light-cone expansion plus renormalization group treatment in leading- and next-to-leading order result in the following representation:

$$\begin{aligned} F_2^N(Q^2) \;=\; & \sum_{i=\pm NS} A_N^i(\mu^2) \left[\frac{\alpha_s(Q^2)}{\alpha_s(\mu^2)}\right]^{d_N^i} \\ & + \frac{1}{\alpha_s(Q^2)} \sum_i \frac{a_N^i}{d_N^i+1} \left\{ 1 - \left[\frac{\alpha_s(Q^2)}{\alpha_s(\mu^2)}\right]^{d_N^i+1} \right\} \\ & + \sum_i \frac{b_N^i}{d_N^i} \left\{ 1 - \left[\frac{\alpha_s(Q^2)}{\alpha_s(\mu^2)}\right]^{d_N^i} \right\} + c_N. \end{aligned} \qquad (38)$$

μ is the renormalization point in the perturbative regime; d_N^i are the one-loop anomalous dimensions; a_N^i, b_N^i and c_N are numbers calculated in one- and two-loop approximations. In the $\overline{\rm MS}$ renormalization scheme α_s is given up to next-to-leading order by

$$\alpha_s = \frac{4\pi}{\beta_0 \log \frac{Q^2}{\Lambda^2_{\overline{\rm MS}}} + \frac{\beta_1}{\beta_0} \log\log \frac{Q^2}{\Lambda^2_{\overline{\rm MS}}} + \ldots}.$$

$$\beta_0 = 11 - \frac{2}{3}N_F \quad \text{and} \quad \beta_1 = 102 - \frac{38}{3}N_F.$$

The quantities $A_N^i(\mu^2)$ in (38) are the photonic matrix elements of quark and gluon operators, incorporating the yet uncalculable long-distance regime. The first sum is well-known from deep-inelastic lepton-nucleon scattering. The last two sums, however, are special for photon targets and they follow from the mixing of quark/gluon and photon operators. All the d_N^i powers of α_s can be mapped into the first term so that, after reparametrization

$$F_2^N(Q^2) = \frac{1}{\alpha_s(Q^2)} \sum_i \frac{a_N^i}{d_N^i+1} + \sum_i \frac{b_N^i}{d_N^i} + c_N + \sum_i \hat{A}_N^i \left[\alpha_s(Q^2)\right]^{d_N^i}. \qquad (39)$$

The $\hat{A}_N^i$ in this form are independent of any renormalization point. The first three terms are recognized as the pointlike components, the last sum as the hadronic component of the photon structure function. They are separately convention independent, i.e. they each fulfill the renormalization group equations and do not depend on the renormalization scheme.

Since the anomalous dimensions d_N^i are positive for all $N > 2$, the hadronic term in the most elegant representation (39) vanishes for $Q^2 \to \infty$, and the structure function is asymptotically determined solely by the pointlike component. The shape of the structure function is therefore predicted by QCD perturbation theory in this limit and the absolute size measures the Λ parameter directly. However, this crystal-clear picture is spoiled by a singularity in the pointlike component for $N = 2$ where d_N^- vanishes, inducing a negative spike for $x \to 0$. The singularity is mapped into the hadronic component when (38) is transformed into (39) and $\hat{A}_N^-$ becomes very large for N close to 2. Eventhough both singularities regularize each other, they require a careful treatment of the hadronic remnant.

The most straightforward experimental evaluation of one of the equivalent representations (38) or (39) would be the accurate measurement of the structure function at four different Q^2 values, determining the three long-distance parameters $\hat{A}_N^i$ and the scale parameter $\Lambda_{\overline{\rm MS}}$. However, data of the required precision to extract $\Lambda_{\overline{\rm MS}}$ in such a program are not available yet, nor can they be expected in the near future.

Two alternative scenarios have therefore been elaborated to cope with these problems:

- After inventing a parametrization of quark and gluon densities at moderate Q^2, the Q^2 evolution of the structure function can be calculated in a way completely analogous to deep-inelastic scattering on nucleon targets [143]. Starting from (38) with an ansatz for $A_N^i(\mu^2 \approx 1\,\mathrm{GeV}^2)$ one finds that QCD provides a fairly model-independent prediction of the slope of the structure function in $\log Q^2$. The sensitivity to Λ, however, is lost since, up to small corrections, the increment $\Delta F_2 \propto \log Q^2/\mu^2$ does not depend on Λ in leading order. Such a conventional approach does not try to exploit the special role of a photonic target so that no qualitatively new insight into QCD can be gained.

- In a different approach [5] that does not merely copy well-known theoretical patterns in deep-inelastic lepton-nucleon scattering, the singularity in the pointlike part of the structure function is isolated and cancelled against a pole term with a properly fixed residue in $\hat{A}_N^i$. The non-perturbative remnants of the expansion about the pole are summarized in a free parameter λ and a well-behaved regular piece

$$\frac{b_N^-}{d_N^-} = \frac{\tilde{b}^-}{N-2} + b_N^{-\,\mathrm{REG}} \tag{40}$$

$$A_N^- = -\frac{\tilde{b}^-}{N-2}\lambda^{d_N^-} + A_N^{-\,\mathrm{REG}}. \tag{41}$$

Based on the physically intuitive ideas of the first subsection, the regular part $A_N^{-\,\mathrm{REG}}$, together with $A_N^{+,\mathrm{NS\,REG}}$, can naturally be identified with the VDM part $F_2^{\mathrm{VDM}} = \alpha H(1-x)$ properly evolved from $Q_0^2 = O(1\,\mathrm{GeV}^2)$ on. This results in the following representation of the Nth moment of the structure function

$$\begin{aligned} F_2^N(Q^2) \;=\; & \frac{1}{\alpha_s(Q^2)} \sum_{i=\pm\mathrm{NS}} \frac{a_N^i}{d_N^i + 1} \\ & \sum_{i=+\mathrm{NS}} \frac{b_N^i}{d_N^i} + \left\{ \frac{\tilde{b}_N^-}{N-2}\left[1 - \left(\lambda\alpha_s(Q^2)\right)^{d_N^-}\right] + b_N^{-\,\mathrm{REG}} \right\} \\ & + F_2^N(Q^2)^{\mathrm{VDM}}. \end{aligned} \tag{42}$$

Before turning to the experimental analysis, a few remarks ought to be added:

- The structure function is not affected by the regularization procedure beyond $x \sim 0.2$, see Fig.36. The large x region should therefore be an ideal place for the measurement of Λ since the regularized, truly hadronic component of the photon structure function dies out $\propto (1-x)$ and gets more and more suppressed for rising Q^2. The λ parameter and H, parametrizing the strength of the VDM part, are strongly correlated, yet with moderate impact on $\Lambda_{\overline{\mathrm{MS}}}$.

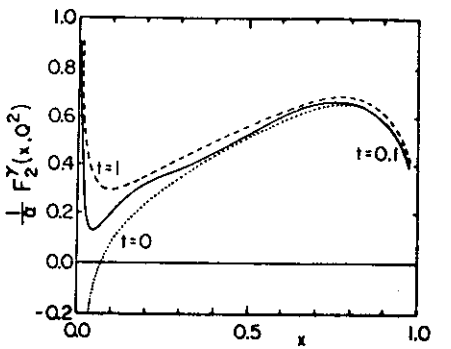

Figure 36: Sensitivity of the photon structure function to the regularization parameter $t = \lambda\alpha_s$ in the approach of [5].

- Singularities occuring beyond the next-to-leading order move quickly to larger N values [142]. Under the same reasonable assumptions on the regularization parameter as above, the corrections are again confined to the small x range $\lesssim 0.15$ and negligible above [151].

Summarizing these points, it is obvious that a reasonable scheme, adequate to the special properties of a photonic target in deep-inelastic scattering, does exist that should allow us to extract the Λ parameter from the photon structure function. Once the parameters are fixed, the scheme predicts the shape and the magnitude of $F_2^\gamma(x,Q^2)$ for all Q^2 in the perturbative regime according to (42) so that the technical assumptions on the regularization procedure can thoroughly be scrutinized in high statistics experiments.

4.3 Experimental Results

The experimental analysis of the photon structure function has moved out of the pioneering phase and more detailed investigations have been carried out recently [152] - [156]. The chapter cannot be considered closed though, since high statistics measurements of the structure function carried out seperately at moderate and large momentum transfer are lacking. Such quality data are indispensable to test the validity of the representation (42) upon which all determinations of Λ are based.

The procedure to determine $F_2^\gamma(x,Q^2)$ is similar to the measurement of the total hadronic cross section for two quasi-real photons. The main difference is the large Q^2 of one of the photons determined by the energy loss and the scattering angle of the electron. Both observables also determine the scaling variable y. The Bjorken variable $x = Q^2/(Q^2+W^2)$ requires the measurement of the invariant hadron energy W. W is easier to measure in this case than for on-shell photons. Since the hadronic system has to balance the transverse momentum of the scattered

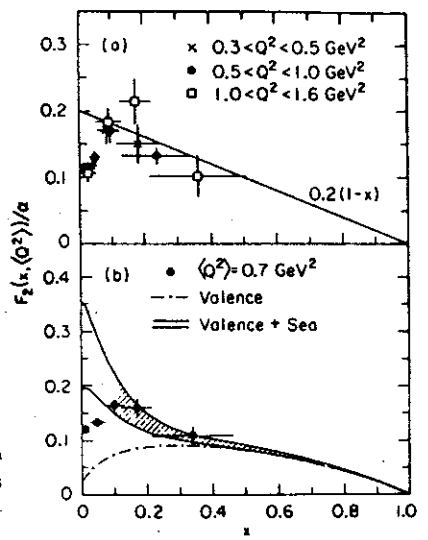

Figure 37: Photon structure function at low Q^2, compared to expectations derived from the pion structure function. Data from [156].

electron, it gets an appreciable boost towards the central detector, which increases the trigger and particle detection efficiency. Due to this transverse boost the measured hadronic mass W_{vis} is fairly close ($\sim$ 70 % on average) to the true mass W. After correcting the data for the effect of resolution and particle losses by Monte Carlo unfolding techniques [158] the physical values of $F_2^\gamma(x,Q^2)$ can be extracted.

Building up the pointlike component

For low Q^2, the cross section for $e\gamma \to eX$ is expected to behave like electron scattering on a hadronic target. The corresponding structure function should therefore drop at large x. For rising Q^2, the shape of the structure function is reversed by the pointlike component so that a rapid growth of the structure function with Q^2 at large x should be observed.

This qualitative effect has in fact been observed by the TPC/Two-Gamma Collaboration at PEP [156]. For low Q^2 the shape is nicely compatible with the qualitative theoretical expectation $F_2^\gamma/\alpha = 0.2(1-x)$, shown in Fig.37a, and also with a recent measurement of the pion structure function [147] shown in Fig.37b that gave $0.22x^{0.41}(1-x)^{0.95}$ for the valence part and $(0.25 \pm 0.09)(1-x)^{8.4}$ for the sea part. Down to the range $x < 0.1$ the pion structure function must be extrapolated so that large uncertainties in any fit procedure are anticipated.

The rapid growth of the structure function with Q^2 at large x is clearly demon-

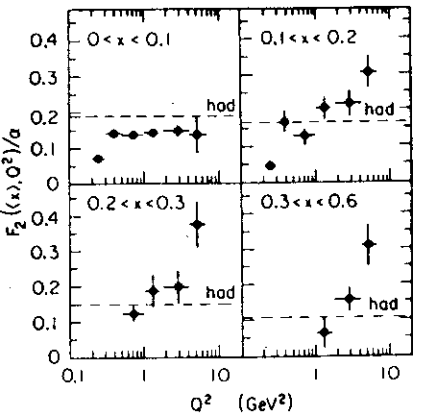

Figure 38: Building up the pointlike component for rising Q^2. Data from [156].

strated in Fig.38. While at small x the growth in the scaling region $Q^2 \geq 0.5\,\mathrm{GeV}^2$ is modest, the structure function increases much faster at large x. This signals the built-up of the pointlike component which is most pronounced in the large x domain.

Both these results conform with our qualitative physical expectations. They are corroborated by studying the final state topology. At low x and low Q^2 the transverse momentum spectrum of the hadrons with respect to the $\gamma\gamma$ axis contains a substantial (or even dominating) hadronic component while at high x, high Q^2 the spectrum is overwhelmingly dominated by the pointlike component, modelled by $\gamma\gamma \to q\bar{q}$ plus quark fragmentation.

Logarithmic growth

Once higher-twist effects of order $m_{q\,eff}^2/Q^2(W^2) \sim 0.1\ \mathrm{GeV}^2/Q^2(W^2)$ for photon targets have died out, QCD predicts a logarithmic growth of the structure function (even in the most conservative approach). This is born out by the experimental analysis if the structure function averaged over the intervall $0.3 \leq x \leq 0.8$, charm subtracted, is plotted versus $\log Q^2$ in a range up to $Q^2 = 200\ \mathrm{GeV}^2$, Fig.39. This figure is a direct consequence of the small quark-gluon coupling in QCD at $Q^2 \geq 2\,\mathrm{GeV}^2$ for which asymptotic freedom is the only known natural explanation in any field-theoretic approach. Non-observation of the logarithmic growth would have ruled out QCD as a field theory of strong interactions. Growth as well as absolute size are compatible with a superposition of a hadronic and a pointlike contribution to the structure function with a scale set by $\Lambda_{\overline{MS}} \sim 200\,\mathrm{MeV}$.

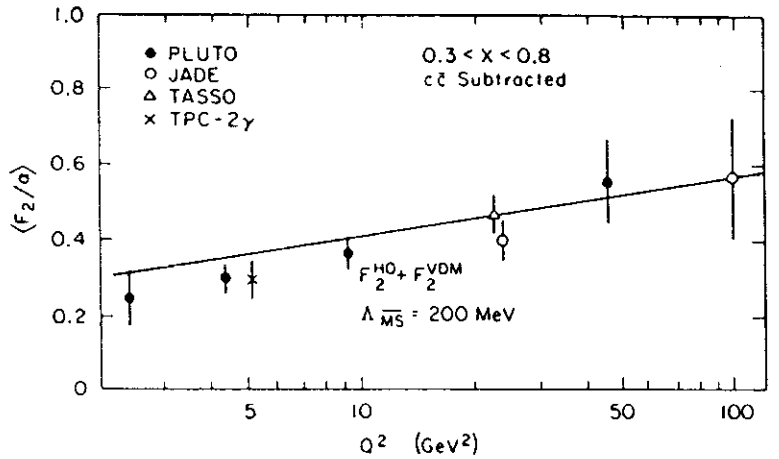

Figure 39: Q^2 evolution of the photon structure function for light quarks compared to the QCD prediction (from [159]).

Shape and size of the structure function, Λ parameter

The properly regularized asymptotic form of the structure function (42) offers a unique opportunity to measure the QCD parameter Λ if the determination is complemented by careful experimental cross checks. Given this regularization scheme, the sensitivity to $\Lambda_{\overline{MS}}$ is demonstrated in Fig.40 for a PLUTO measurement. A statistical error as small as 50 MeV appears feasible when the results of various experiments are combined.

The structure function has been measured by the PLUTO, CELLO, JADE and TASSO Collaborations at PETRA and by the TPC/Two-Gamma Collaboration at PEP for various values of Q^2 ([152] - [157]). Results are presented in Fig.41 in a sequence of rising average Q^2. Within error bars the asymptotic form in next-to-leading order of the structure function appears to conform with the data points. For the sake of clarity only fits including higher-order QCD corrections are shown in the figures (a reader interested in a broader discussion might consult the original papers). The results of detailed fits are collected in Table 6. As expected, part of the VDM contribution could be mapped into the non-perturbative parameter λ, paraphrased as $t = \lambda\alpha_s$. The physical picture reflected in Table 6 appears consistent. An overall fit of the $\Lambda_{\overline{MS}}$ parameter [159] yields the average value

$$\Lambda_{\overline{MS}} = 195^{+60}_{-40}\,\mathrm{MeV} \qquad (43)$$

in good agreement with Λ values obtained in deep inelastic lepton-nucleon scat-

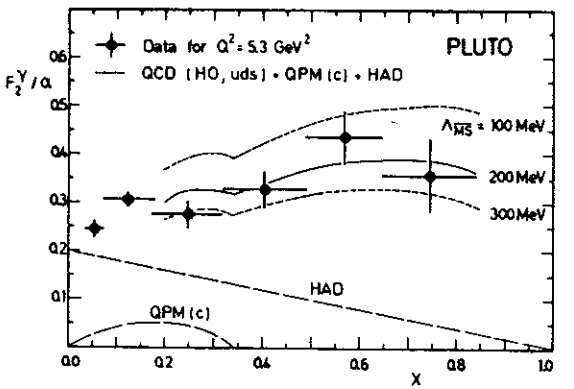

Figure 40: Sensitivity of the photon structure function to a change of $\Lambda_{\overline{MS}}$ [152]. The regularization scheme of [5] was adopted.

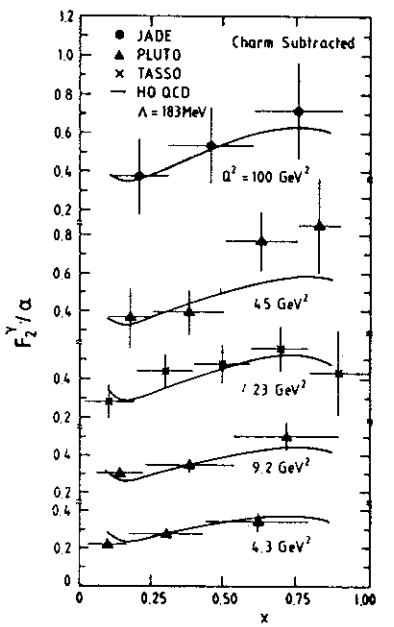

Figure 41: Experimental analysis of the photon structure function for various Q^2 ranges, compared to the (regularized) QCD predictions (from [160]).

Experiment	$Q^2(\mathrm{GeV}^2)$	VDM	t	$\Lambda_{\overline{\mathrm{MS}}}$
TPC/$\gamma\gamma$	5.1	$0.2(1-x)$	fitted $0.03 \pm .01$	257 ± 92
TASSO	7-70	$0.2(1-x)$	0	140^{+190}_{-60}
PLUTO	3-100	fitted	fitted 2.2	183^{+80}_{-54}
JADE	10-220	$0.2(1-x)$	1	250 ± 90

Table 6: $\Lambda_{\overline{\mathrm{MS}}}$ measurements in $e\gamma$ scattering.

tering, $\Lambda_{\overline{\mathrm{MS}}} = 186 \pm 60$ MeV [161], and from radiative Υ and Υ' decays [162]. Nevertheless, a drastic reduction of the error bars and the confrontation of the parametrization (42) for one set of parameters with data taken at various Q^2, is mandatory before this chapter can be closed finally. The measurement of this fundamental scale parameter should be considered a most important task for experiments continuing at the upgraded PEP and at LEP.

5 Hard Scattering Processes in Two-Photon Interactions

5.1 The Leading Two Jet Process

The production of hadrons at large transverse momenta in $\gamma\gamma$ collisions is a short-distance process [12]. Due to asymptotic freedom in QCD, the reaction amplitudes can be systematically expanded in the quark-gluon coupling constant. In lowest order the two-photon production of hadrons in e^+e^- reactions proceeds via the subprocess $\gamma\gamma \to q\bar{q}$ (Fig.42), with the differential cross section ($\hat{s}, \hat{t}, \hat{u}$ are the Mandelstam variables for the process):

$$\frac{d\sigma}{d\hat{t}}(\gamma\gamma \to q\bar{q}) = e_q^4 \frac{2\pi\alpha^2}{\hat{s}^2} \frac{\hat{t}^2 + \hat{u}^2}{\hat{t}\hat{u}}. \tag{44}$$

The quarks subsequently fragment into hadrons leading at high enough energies to distinct two-jet topologies.

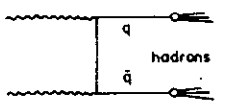

Figure 42: Born diagram for the two-photon production of hadrons via a quark-antiquark pair.

However, short distance processes with direct quark exchange between the photons show only up at large transverse momenta of the quarks. As already discussed in Sect.3, the dominant contributions to the $\gamma\gamma$ total cross section come from non-perturbative processes in which hadrons are predominantly produced with limited transverse momenta, see (24). The Born diagram (Fig.42) is expected to dominate the hadronic two-photon cross section if the quarks are produced with large transverse momenta relative to the incoming photons. In this case the large p_T behavior of the quarks, as well as of the hadrons emerging from the quarks, should become [163]:

$$\frac{d\sigma}{dp_T^2} \sim \frac{1}{p_t^4}. \tag{45}$$

This power law becomes observable only if p_T is large enough so that all other contributions which drop faster can be neglected. On the other hand p_T should be small compared to the kinematical limit, i.e. $x_T = 2p_T/\sqrt{s}$ should not be close to 1 ($\sqrt{s}$ is the total e^+e^- energy). The p_T^2 distribution of inclusive hadrons produced in $\gamma\gamma$ interactions, Fig.43, clearly shows the exponential behavior at low p_T turn over into a power law behavior at about 1 GeV. Thus in $\gamma\gamma$ reactions hard scattering effects appear to become visible at much lower energies and transverse momenta than observed in hadronic reactions. These $\gamma\gamma$ reactions seem to offer an almost

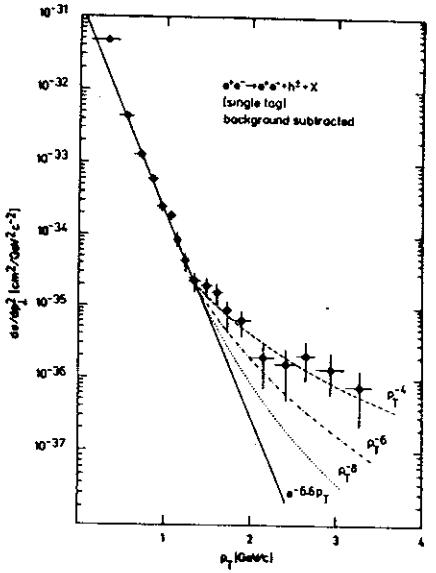

Figure 43: Transverse momentum distribution of inclusive hadron production by two photons measured by TASSO [164]. The exponential dependence at low p_T approaches a p_T^{-4} behavior above about 1 GeV. ISR data on inclusive pion production in pp reactions show, at similar c.m. energies, an approximate p_t^{-12} law [165].

unique possibility to study the basic hard scattering processes of the constituents of matter in a rather clean way and already at relatively low energies [12].

In analogy to the definition of R in one-photon annihilation processes, $R_{\gamma\gamma}$ is defined as the ratio of the cross section for the two-photon production of hadrons to that of muon pairs,

$$R_{\gamma\gamma} = \frac{\sigma(e^+e^- \rightarrow e^+e^- + hadrons)}{\sigma(e^+e^- \rightarrow e^+e^- + \mu^+\mu^-)}. \qquad (46)$$

Hadron production via the lowest order process (Fig.42) yields for four quark flavors and three colors:

$$R_{\gamma\gamma} = 3\sum_q e_q^4 = \frac{34}{27} \qquad \text{for } q = u, d, s, c. \qquad (47)$$

Even in the absence of QCD corrections this is only correct in a kinematical region where the quark masses can be neglected which is the case at large transverse momenta. In this region also the QCD corrections should be small.

Comparing experimental results for $R_{\gamma\gamma}$ to the lowest order expression (47) is only sensible in the large p_T region. The p_T dependence of jet production in lowest

order is obtained by convoluting the subprocess cross section (44) for $\gamma\gamma \rightarrow q\bar{q}$ with the two-photon flux and integrating over the longitudinal quark momenta. Using the equivalent photon approximation this yields [166]:

$$\frac{d\sigma}{dp_T^2}(e^+e^- \rightarrow e^+e^- q\bar{q} \rightarrow e^+e^- + 2jets) = R_{\gamma\gamma}\,\eta^2\frac{\alpha^2\pi}{p_T^4}D(x_T) \qquad (48)$$

$$\text{with } \eta = \frac{\alpha}{2\pi} log\frac{s}{4m_e^2}.$$

For medium x_T values ($x_T \approx 0.2$) this expression has an approximate p_T^{-4} behavior since at medium x_T the function $D(x_T)$ is roughly flat [166]. A typical experimental range for the analysis of large-p_T jets is $0.1 \leq x_T \leq 0.3$.

After fragmentation of the quarks into hadrons the p_T distribution for inclusively produced hadrons is found to have the same form (48) but with a different function describing the hadron x_T dependence [166]. For single hadrons the x_T dependence becomes somewhat steeper towards x_T=1, but there is still a medium x_T range where the approximate p_T^{-4} power law is maintained.

5.2 Other Hard Scattering Processes and QCD Corrections

At the Born level only the electromagnetic couplings of quarks to photons are relevant. The Born process, however, could be obscured by large QCD corrections and by non-perturbative remnants of small angle scattering. It is therefore necessary to determine the kinematical range where those corrections are small.

Multi-jet cross sections

Beyond the Born approximation the parton structure of the photon as measured in deep-inelastic electron-photon scattering plays an important role. The structure functions are given by the flux of quarks and gluons within photons. Examples for leading diagrams taking into account the parton content of the photon are shown in Fig.44.

Three-jet topologies arise from the diagrams a) and b) where a photon scatters off the parton content of the other photon ($\gamma q \rightarrow qg$ and $\gamma g \rightarrow q\bar{q}$). Diagram c) gives an example for a four-jet topology ($gg \rightarrow q\bar{q}$). The multi-jet diagrams a) to c) have one or two additional jets made up by the fragments of the photons besides the two high-p_T jets. These fragments preferentially travel down the beam pipe ('beam pipe jets') which makes it experimentally difficult to separate these configurations from the Born process. The multi-jet cross sections asymptotically lead also to a p_T^{-4} power law since the α_s dependence for the gluon-quark couplings cancels against the $1/\alpha_s(p_T^2)$ behavior of the photon structure function [167]. At

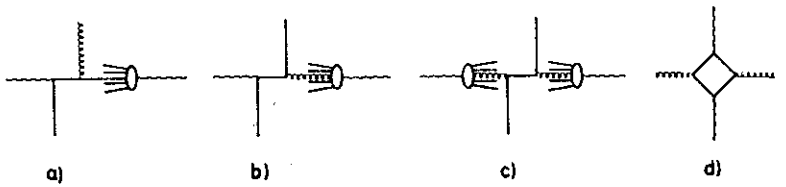

Figure 44: Some leading QCD diagrams contributing to jet production by two photons in addition to the Born diagram. The blobs indicate the splitting of the photon into partons.

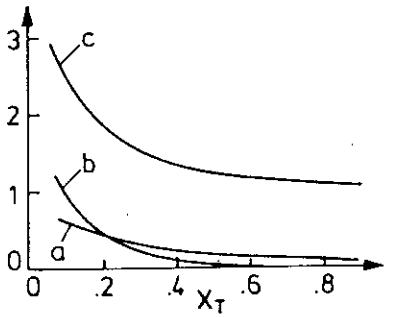

Figure 45: Relative contributions to $\frac{d\sigma}{dp_T^2}(e^+e^- \to e^+e^- + \text{jet} + X)$: a) 3-jet/2-jet; b) 4-jet/2-jet; c) (2+3+4)-jet/2-jet [168].

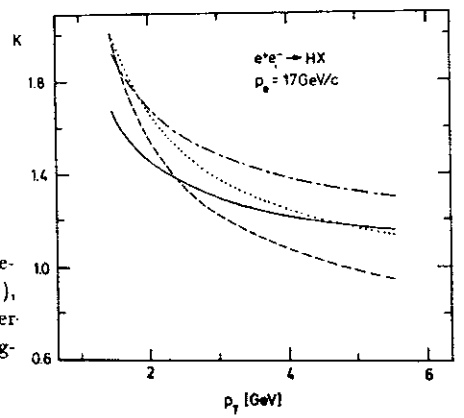

Figure 46: QCD correction to the zeroth order jet cross section (K-factor), taken from [170]. The curves differ in the assumptions for the gluon fragmentation as explained in [170].

finite energies, however, the distribution of the available $\gamma\gamma$ energy amongst more than two jets leads to a reduction of the multi-jet contribution at large p_T.

The relative contributions of the perturbatively calculable scattering processes to the inclusive jet cross section are shown in Fig.45 [168]. Converting the x_T scale in this plot to a p_T scale at $\sqrt{s}$= 35 GeV, which is a typical e^+e^- energy at PETRA, the multi-jet contributions are larger than the Born 2-jet cross section below $p_T \approx$ 3 GeV. At p_T=5 GeV (x_T=0.3), about the highest p_T value for which data are available, the multi-jet cross section still contributes about 50% of the 2-jet cross section.

Two-gluon jet final states in $\gamma\gamma$ collisions can be produced in 2nd order QCD through a quark loop, Fig.44d. The cross section for this subprocess is expected to be an order of magnitude smaller than that for quark jets, but the effect could be enhanced by using longitudinal polarized beams [169].

Besides the perturbatively calculated contributions one has also to take account of those processes were either one or both photons interact as a virtual vector meson. This contribution has recently been reevaluated using the latest photoproduction-data [170].

QCD corrections to the Born diagram

A comparison of the measured jet cross section to the leading QCD contributions requires the control of the higher order corrections. Calculations have been done for either jet [171,172] or single hadron cross sections [173,170].

The evaluation of QCD corrections to the inclusive jet cross section turns out to be rather problematic. To handle gluon bremsstrahlung either an *a priori* unknown cut-off parameter [171] has to be introduced, or Sterman-Weinberg parameters ϵ and δ which define a jet by the energy fraction ϵ within an angular cone with opening angle δ [172]. Since in $\gamma\gamma$ reactions the total $\gamma\gamma$ energy is not known in general and thus the fraction of the energy contained in a jet, these corrections are difficult to apply.

To bypass these problems, the authors of [173,170] calculated the $O(\alpha_s)$ corrections to the inclusive single hadron cross section rather than to the jet cross section. The K-factor, i.e. the ratio of the fully QCD corrected to the zeroth order Born cross section, is found to be relatively small. In Fig.46 the p_T dependence of the K-factor is shown for different assumptions on the gluon fragmentation. As we will discuss below the small corrections to the Born term are at variance with the data. We will return to this point after the experimental results are presented.

5.3 Experimental Methods

The investigation of high-p_T phenomena in two-photon reactions requires sufficiently high $\gamma\gamma$ fluxes at energies where jet formation becomes observable. Such

$\gamma\gamma$ fluxes became only available at the PETRA and PEP storage rings. While at these machines low energy $\gamma\gamma$ physics is always plagued with trigger inefficiencies, this is no specific problem for the investigation of jet topologies and hadrons with large p_T. The penalty to be payed is a serious background from one-photon annihilation processes. In a notag experiment the cut in $W_{\gamma\gamma}$ has to be delicately balanced between the need of having $W_{\gamma\gamma}$ large enough to isolate jet events and at the same time small enough not to be swamped by one-photon events. The remaining annihilation background has to be subtracted by means of simulation programs. In a typical notag analysis of hard scattering processes $W_{\gamma\gamma}$ is restricted to a range between about 4 and 12 GeV.

Even under the single tag condition one cannot completely avoid the annihilation background because either hadrons or converted bremsstrahlung photons can fake a tag in a forward detector. Since in the case of converted bremsstrahlung photons the hadronic system is boosted into the direction opposite to the tag, which is not necessarily so for $\gamma\gamma$ events, one can find quite effective cuts reducing this background.

At PETRA/PEP energies the jet topologies in two-photon events are less pronounced and thus more difficult to analyze than in one-photon events. The reasons are the lower c.m. energy, the in general non-collinear jet topology and the fact that in multi-jet events some of the available energy disappears in the beam pipe. All this makes the analysis in general more dependent on specific models, and most of the results are given in terms of ratios between measured rates and expected rates from a model including detector effects. For example, PLUTO defines $\tilde{R}_{\gamma\gamma}$ as the ratio of the measured jet rate to that predicted by a model based on the Born diagram [174]. The model uses the QED cross section for quark pair production with constituent quark masses (above $p_T \approx$ 1 GeV the model becomes insensitive to the assumed quark mass). The hadronization of the quarks is described by standard fragmentation programs as used also in one-photon annihilation analyses. Feeding finally everything through a detector simulation program makes the model comparable to the data. Results are usually presented in terms of variables which have the measured uncorrected values (in this example the measured jet-p_T value).

Various procedures have been applied to analyze jet topologies. If dominance of two-jet configurations can be expected one may apply a thrust analysis which divides an event into two jets. Thrust can be defined in the $\gamma\gamma$ c.m. system with respect to a unique event axis or in the laboratory system by maximizing the sum of the thrust values along two in general different jet axes. Inspection of the thrust distributions as well as of the average momenta parallel and perpendicular to the thrust axis (Fig.47) allows testing whether the considered event indeed has the assumed two-jet topology. In a more general approach one allows for an arbitrary number of jets in an event by searching for clusters of hadrons. There are different ways to find clusters [175,176] and within each method the definition of what is a

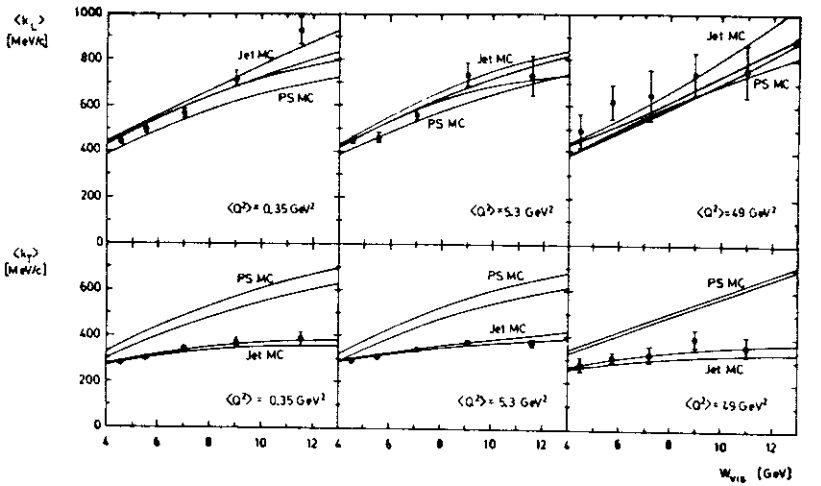

Figure 47: Distribution of the average particle momenta perpendicular and parallel to the thrust axis [174].

jet can be adjusted to the actual problem using the proper feed back from a Monte Carlo simulation.

5.4 Experimental Results on Hard Scattering Reactions

The first analyses of hard scattering processes in two-photon reactions were published by the JADE and TASSO groups [177,164]. Both groups used the single tag method with $< Q^2 > \approx$ 0.3 GeV^2 of the tagged photon. Fig.43 shows the transverse momentum distribution dN/dp_t^2 plotted versus p_T for single hadrons as measured by TASSO. At low p_T the distribution exhibits the exponential fall-off expected if photon-photon scattering is vector meson dominated, i.e. if it behaves like hadron-hadron scattering. However, already around $p_T \approx$ 1.5 GeV the slope levels off and becomes compatible with a p_T^{-4} behavior. This early onset of hard scattering signatures is clearly different from hadron-hadron scattering and must be interpreted as evidence for the pointlike coupling of the photons to the constituents of hadrons. At similar c.m. energies hadronic reactions exhibit a much steeper slope even at larger p_T.

Analyzing the data in terms of two-jet events, JADE and TASSO compared the measured jet cross section to the prediction from the Born approximation for $\gamma\gamma \rightarrow q\bar{q}$. As evident from Fig.48 for the JADE results, the cross section lies consistently higher than the Born cross section (by about a factor 2 above $p_T^{jet} \approx$ 2

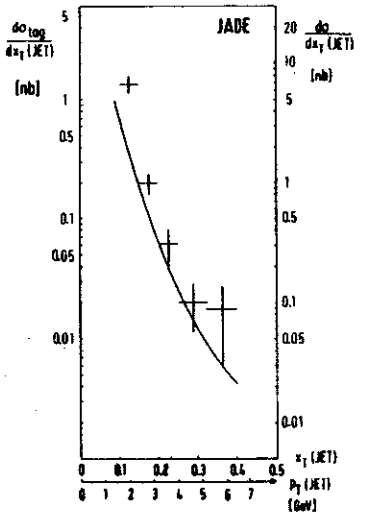

Figure 48: Transverse momentum dependence of jets produced in two-photon collisions as measured in a single-tag experiment with $Q^2 \approx 0.3$ GeV^2 [177].

GeV), while the shape at large p_T^{jet} seems to agree with the prediction. A similar result was obtained by the TASSO group.

Integer quark charges?

These measurements initiated some speculations [178] that the two-jet cross section might be a signal for integer quark charges. The Han-Nambu version of the integer charge quark (ICQ) model [179] yields a $R_{\gamma\gamma}$ value of 10/3 which is 3 times larger than for fractional charged quarks (FCQ). This original form of the ICQ model has not built in the local gauge invariance inferred from the color group. In a locally gauge invariant version of the ICQ model (referred to as 'gauged ICQ') photons and gluons can both have electric and color charges, $SU(3)_{colour}$ is a broken symmetry and the gluons acquire masses [180]. In this model the charge of a quark is partly screened and the effective charge seen by a photon can be written as (m_g is the gluon mass):

$$Q_{eff}(Q^2) \;=\; Q_0 \;+\; \frac{m_g^2}{m_g^2 + Q^2}\; Q_8. \qquad (49)$$

The charge Q_0 is also seen by the normal color singlet photon in the FCQ, while the color octet part of the photon, the characteristic feature of the ICQ, is damped at large Q^2 by a gluon propagator term. In this theory the striking difference between the FCQ and the ICQ is revealed only at $Q^2 \approx 0$.

Because of this prediction and despite of the considerably larger experimental difficulties, several groups analyzed notag data with Q^2 values close to zero [181,182,183].

The TASSO group analyzed inclusive hadron production in the notag mode [181]. Fig.49 shows the p_T^2 distribution of charged hadrons after subtraction of the estimated VDM contribution which was modelled with an exponential p_T dependence. In the p_T range from 1.5 to 3.0 GeV the data are higher than the Born term by about a factor 4.

Thus these experimental results are in qualitative agreement with the 'gauged ICQ' model. On the other hand, higher order corrections to the two-jet cross section and other QCD contributions, like multi-jet production and higher twist effects, are expected to modify the pure Born term. As discussed in Sect.5.2 these corrections have been calculated for single hadron p_T distributions and were found to be relatively small [173,170]. An estimate of the sum of the corrected Born term and all other perturbative QCD contributions obtained from [170] is included in Fig.49 [184]. The data are still much higher than the sum of all QCD contributions.

If this excess was really due to integer quark charges the events should have the two-jet topology expected for the Born process. As part of an extensive study of the p_T and Q^2 dependence of jet production the PLUTO group investigated also the topology of events produced by two quasi-real photons [182]. Using a thrust algorithm each event was divided into two jets. Fig.50 shows a plot of $\bar{R}_{\gamma\gamma}$, the ratio of the observed number of jets to those expected from the Born process, as a function of the transverse momenta of the jets. The large excess at small p_T^{jet} is naturally explained by a VMD model. However, above ~2 GeV where the Born term is expected to dominate, there remains an excess unexplained by either model. The thrust distribution of large p_T jets, however, shows that the average thrust is smaller than expected from the Born process alone. In Fig.51 the $\bar{R}_{\gamma\gamma}$ distribution is plotted only for events with a thrust value exceeding 0.9. The observed high thrust jet rate in the region $2 < p_T^{jet} < 6$ yields $\bar{R}_{\gamma\gamma} = 1.2 \pm 0.3$ [182]. Hence the 'naive' Han-Nambu model of integrally charged quarks ($\bar{R}_{\gamma\gamma}$=2.65) is ruled out by more than 4 standard deviations. In the framework of the gauged ICQ model this result can be converted into a limit for the gluon mass [182]:

$$m_g \;<\; 5\ M\varepsilon V\ (95\%\ c.l.).$$

Results on high energy Compton scattering and on the production of two prompt photons in pion-nucleon scattering also strongly support the conventional model of fractionally charged quarks [185].

Thus the ICQ model is not likely to be the correct explanation for the excess of jets or single hadrons with large p_T which, according to the PLUTO results, are produced in less jetty events than expected from the Born process. Possible other explanations for the excess will be discussed below.

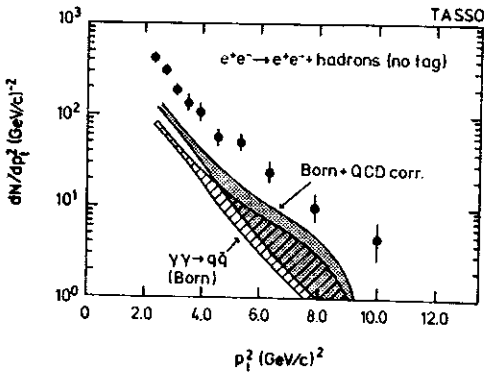

Figure 49: Transverse momentum distribution of charged hadrons measured in a notag experiment with $Q^2 \approx 0$ [181]. The standard VDM contribution with an exponential p_T dependence is subtracted. The data are compared to the lowest-order process for hadron production (hatched area) and to the sum of all perturbatively calculable processes (shaded area); the bands include uncertainties due to fragmentation effects.

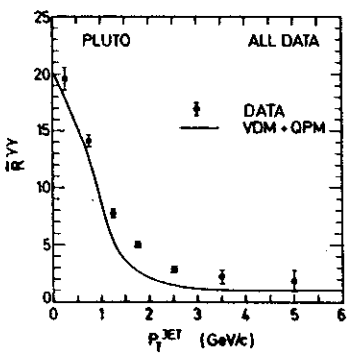

Figure 50: The ratio of the observed number of jets to those predicted by a Born model versus p_T^{jet} for notag data [182]. The data are compared to an incoherent sum of the Born term and a VDM model.

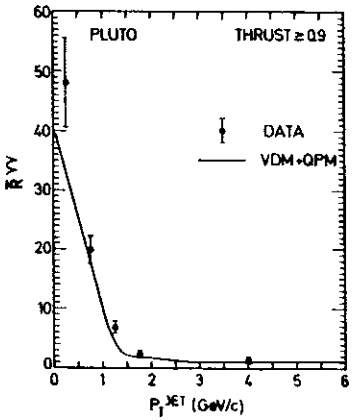

Figure 51: The same plot as in Fig.50 but including only events with a thrust value larger than 0.9.

Q^2 dependence of jet production

The PLUTO group also investigated the p_T and Q^2 dependence of jet production [174,182]. The results are shown in a comprehensive form in Fig.52 where $\bar{R}_{\gamma\gamma}$ is plotted versus p_T^{jet} for different Q^2 values ranging from $Q^2 \approx 0$ to $Q^2 = 49$ GeV^2. In this analysis the jets are defined by a thrust algorithm forcing all events into two-jet topologies. Figure 47 demonstrates that the events are indeed consistent with a two-jet structure.

For small Q^2 the value $\bar{R}_{\gamma\gamma}=1$, which means quantitative agreement with the Born approximation, is approached from above. However, as we had already discussed before, it appears that in the investigated p_T range this value is not reached. For the largest Q^2 values, $Q^2 \geq 10\ GeV^2$, jet production is consistent with the Born term over the whole p_T^{jet} range.

The excess at small p_T^{jet} can be explained by a VDM contribution shown as the shaded band in the picture. The data are well reproduced if the VDM is simulated by two-jet events with jet directions peaking along the directions of the incoming photons. This is achieved by generating quark pairs according to $d\sigma/dp_T^2 \sim \exp(-5p_T^2)$ and fragmenting the quarks using the Field-Feynman scheme [186]. The VDM cross section was assumed to be constant in $W_{\gamma\gamma}$ and the Q^2 dependence was described by a GVDM form factor (see Sect.3). This model was found to be in good agreement with the data. As an example, the different relative VDM contributions at low and high Q^2 can nicely be revealed by plotting the angular distribution of the jets with respect to the $\gamma\gamma$ direction (in the $\gamma\gamma$ c.m. system), Fig.53 [187]. At low Q^2 the distribution is peaked in the forward direction as expected from a 'hadronic' Monte Carlo simulation. In the high Q^2 range the distribution becomes flatter and approaches the shape predicted by the simulation of the 'pointlike' Born term.

In the PLUTO analysis the events were forced into 2-jet topologies. According to Fig.47 the bulk of the events is indeed consistent with 2-jet final states. However, since most of the events have a VDM origin one would like to know if this is true in all kinematical regions. Of particular interest is the question whether the excess of events found at large (or medium) p_T^{jet} and low Q^2 is associated with jet-like events. The thrust distribution of the jets with $p_T^{jet} > 2$ GeV is shown in Fig.54a,b for two Q^2 ranges. Compared to a simulation of the Born process the distribution is shifted towards smaller thrust values, i.e. the events are more spherical. The shift is largest for small Q^2; for $Q^2 > 10$ GeV^2 the thrust distribution is consistent with the Born prediction (Fig.54c).

Explanations for the large-p_T excess at low Q^2

The PLUTO group has found out that the event topologies and the p_T^{jet} distributions can be qualitatively described by adding multi-jet contributions. Multi-jet

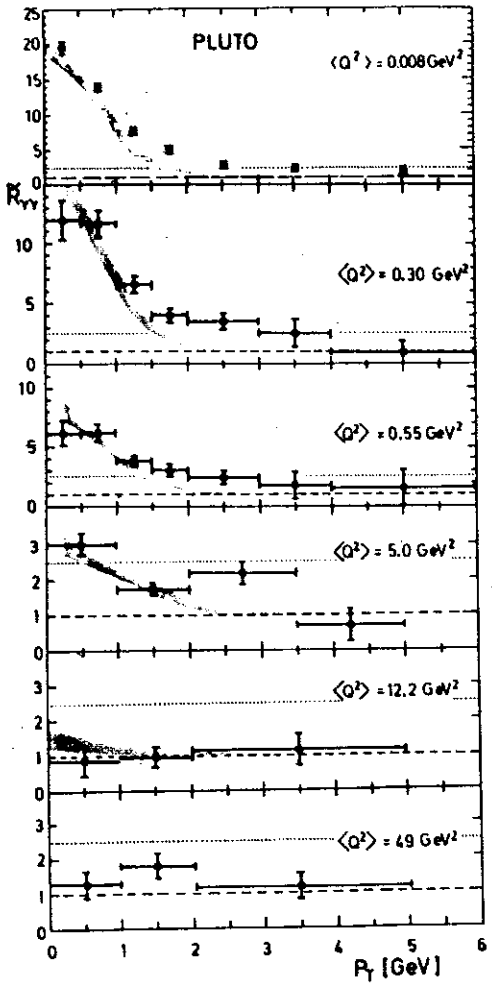

Figure 52: $\bar{R}_{\gamma\gamma}$ versus p_T^{jet} for different average Q^2 values [174]. The estimated contribution from VDM is indicated by the shaded band. Shown are also the Born predictions for fractional (dashed) and for integer (dotted) quark charges.

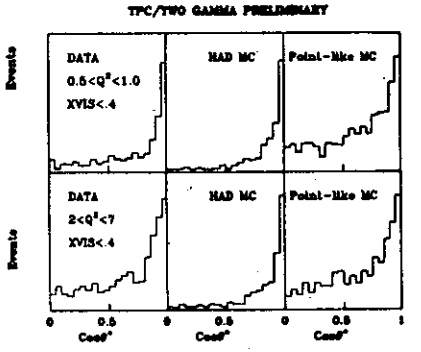

Figure 53: Angular distributions of jet directions for two Q^2 values. The data are compared to Monte Carlo simulations of hadronic (VDM) and point-like photon-photon scattering [187].

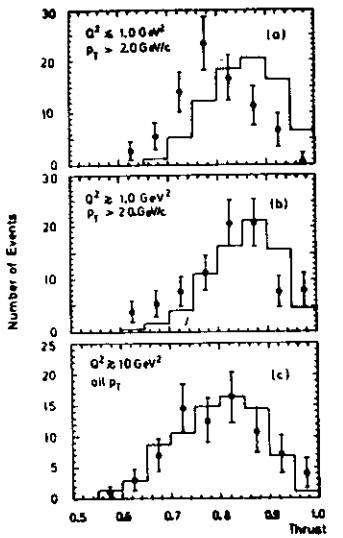

Figure 54: Thrust distributions for (a) low-Q^2 and (b) high-Q^2 events with $p_T^{jet} > 2$ GeV and (c) for events $Q^2 > 10$ GeV^2 [174]. The data are compared to the Born prediction which is in (a) and (b) normalized to the data.

events are predicted by QCD as discussed in Sect.5.2. Since each jet gets a smaller fraction of the available energy such events look more spherical. However, no theoretical prescription for the absolute normalization of this additional contribution had been employed.

In fact, a large admixture of perturbative multi-jet final states may not be easy to reconcile with the theoretical analysis of QCD corrections for single hadrons produced at high p_T which were found to be small [170,173]. In [170] it was suggested instead that the excess in the high p_T tail of inclusive hadrons may be explained by a modification of the VDM contribution. This contribution was estimated by relating the two-photon cross section to γp and pp scattering data assuming VDM and quark model relations. The result is a p_T spectrum which does not fall all the way exponentially but which develops a power law tail at large p_T. Assuming in addition an average intrinsic p_T for the quarks of 0.35 GeV, which is in good agreement with photoproduction data, this tail is enhanced considerably. It might thus be concluded that the hadronic component of the photon is probably not negligible in the p_T range covered in the inclusive p_T spectrum of Fig.49. The sum of the perturbative QCD contributions and the VDM estimate can be higher than the simple Born term by a factor of 2.6 at p_T^2= 6 GeV^2 and by a factor of 2 at p_T^2= 10 GeV^2 [170].

These investigations suggest that in processes involving two real photons the experiments did not reach a domain which is simply described by the Born approximation. The same estimates show that even in the p_T range which can be reached at LEP the non-perturbative effects are not small. At LEP energies, however, the jet topologies of the pointlike contributions may be recognized more readily.

Charm production in two-photon reactions

At the Born level $R_{\gamma\gamma}$ depends on the 4th power of the quark charges and thus only 2/3 charged quarks make a significant contribution. Therefore the events with high-p_T hadrons would mainly be built up by u and c quark jets if the Born process is the dominant source for these events. As can be inferred from hadronic scattering and from photoproduction data the VDM mechanism is expected to yield a very small number of events containing charm (<1% [188]). Hence, studying inclusive charm production offers another test of the Born contribution to the observed hadronic cross section (for theoretical estimates of exclusive final states see [118]).

The JADE group observed charm production in single-tag two-photon events [189]. As usual [190] $D^{*\pm}$ mesons were identified by exploiting the small Q-value of the decay $D^* \rightarrow D^0\pi$ which yields a very good resolution for the D^*-D^0 mass difference. The signal contains, after background subtraction, $19 \pm 7 \pm 2$ D^* mesons in the investigated data sample. This has to be compared to the 5.2 ± 2.4 D^*'s predicted by a simulation of the Born process. The relatively large number of events containing charmed quarks underlines the importance of the pointlike coupling of

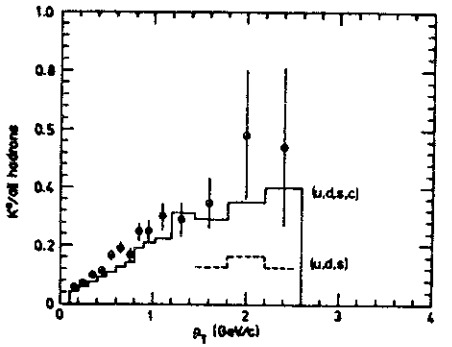

Figure 55: Ratio of K^0 to charged hadron production measured by Mark II [191]. The data are compared to models with and without charm production.

the photons to the quark charges.

The Mark II group analyzed the yield of kaons as a signature for charm decays [191]. Fig.55 shows the ratio of K_S^0 production to the production of all hadrons as a function of p_T. A comparison to the Monte Carlo simulations with and without charm production indicates the importance of the charm contribution in explaining the measurement. Within the statistical and systematic uncertainties of the Monte Carlo simulation the data agree with the model including charm. Although the data are slightly higher than the prediction there is certainly no indication for an excessive charm production.

Clearly a more extensive study of charm production in two-photon reactions would be useful for a systematic understanding of the processes contributing to the cross sections at large p_T.

Summary

Signatures for hard scattering phenomena in two-photon reactions have been observed by analyzing the transverse momentum distributions of single hadrons and of jets. At low transverse momenta the VDM component of the photons produces jets which are collimated in the forward direction. Typically at p_T values around 1.5 GeV the pointlike component of the photon becomes visible as inferred from a flattening of the tail of the p_T distribution. As p_T increases the data approach the Born prediction for two-photon production of jets from above.

At low Q^2 the Born level does not seem to be reached yet at large p_T, neither for jets nor for single hadrons. The excess is found to be due to events with a less jetty topology. The topology of these events can be qualitatively described by a contribution of multi-jet events as expected from QCD though detailed theoretical

investigations rather suggest remnant VDM contributions as the source of these excess events. On the other hand, large-thrust events are consistent with the Born approximation assuming fractionally charged quarks. This rules out integer charge quark models. For the gauged version of this model the effective gluon mass is constraint to be less than 5 MeV.

At large Q^2 the jet cross section approaches the Born prediction for all p_T. This conforms with the observed dominance of the pointlike photon piece in the photon structure function.

The contribution of the Born process to the two-photon cross section can also be tested by measuring charm production. From the hadronic component of the photon one expects only a very small contribution to the charm production cross section. First results suggest abundant charm production confirming the importance of the pointlike couplings of the photons to the constituents of matter.

6 Exclusive Hadron Production at Large Angles

The exclusive production of hadron pairs in $\gamma\gamma$ collisions at high energies and large angles [11] involves short and long distance interactions at the same time. The creation of quark and antiquark pairs at large transverse momenta with respect to the $\gamma\gamma$ axis extends only over femto-distances while mesons and baryons form at the fermi scale. In contrast to inclusive short-distance processes the probability amplitude for hadron formation from quarks, however, does affect the cross section so that these exclusive $\gamma\gamma$ reactions exhibit the interesting interplay between short and long distances in QCD. They offer a unique test of the theory of strong interactions.

The theoretical predictions can be divided into two categories. Scaling laws and asymptotic helicity selection rules can easily be derived from the basic structure of the short-distance diagrams involved. Angular distributions and absolute normalization of the cross section, on the other hand, depend on the meson and baryon wave functions. These reactions can thus provide more detailed insight into the quark dynamics within hadrons than the computation of purely static hadron properties can offer. Both machineries of strong interaction physics at large distances, the ITEP sum rule approach as well as the lattice formulation of QCD, have been applied to analyse these wave functions.

Experimental analysis have been performed at PEP and PETRA for pion/kaon production as well as baryonic final states [192]-r1911. The overall picture in the former case appears compatible with the theoretical QCD predictions though data are demanded at energies farther beyond the resonance region [196]. The comparison of the baryon yields with the QCD predictions suffers from the steep fall-off of the cross section at high energies so that no satisfactory conclusion can be drawn so far.

6.1 Theoretical Set-Up

The scattering amplitude for exclusive meson pair production at large angles [11]

$$\gamma\gamma \to M\overline{M} \tag{50}$$

(and similary for baryon production) factorizes into a hard scattering amplitude T_H and soft hadronic wave functions $\Phi(x_i)$ that cannot be calculated in perturbation theory. This is visualized in the generic diagrams shown in Fig.56. The large angle high energy subprocess $\gamma\gamma \to q\bar{q}$ extends only over the short distance $O(1/\sqrt{s}\sin\vartheta)$, and the gluon lifetime and travel distance are short as well. The creation of two parallel quarks and antiquarks $q\bar{q}'$ and $q'\bar{q}$ is thus completed at the distance $O(1/\sqrt{s}\sin\vartheta)$ so that QCD perturbation theory is applicable to this short-distance part of the process. The long-distance part is described by the probability amplitude $\Phi_M(x, p_T)$ for finding a $q\bar{q}'$ pair in the meson M. x denotes the

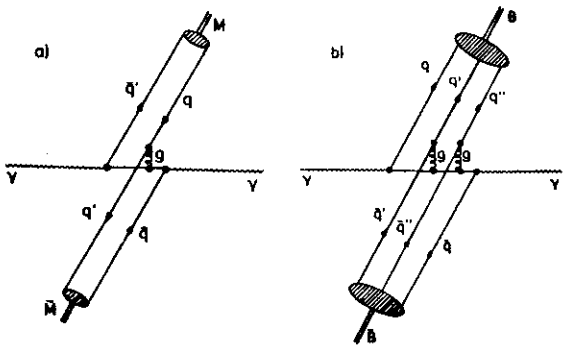

Figure 56: Wide-angle meson (a) and baryon (b) pair production at high energies in $\gamma\gamma$ collisions (generic diagrams).

fractional longitudinal momenta of the constituents with transverse momenta less than p_T. The scattering amplitude is a convolution of the short distance amplitude with the distribution amplitudes

$$\mathcal{M} = \int dxdy\Phi_M^*(x,p_T)T_H(x,y,p_T)\Phi_M(y,p_T). \tag{51}$$

The hard scattering amplitudes can be computed by standard perturbation rules though the analysis becomes herculean when baryons are involved since the number of diagrams is huge. As important examples we note the lowest order amplitudes for helicity zero quark-antiquark pairs

$$\left.\begin{matrix} T_{++} \\ T_{--} \end{matrix}\right\} = \frac{16\pi\alpha_s}{3\hat{s}}\frac{32\pi\alpha}{x(1-x)y(1-y)}\left[\frac{(e_1-e_2)^2a}{1-\cos^2\vartheta}\right] \tag{52}$$

$$\left.\begin{matrix} T_{+-} \\ T_{-+} \end{matrix}\right\} = \frac{16\pi\alpha_s}{3\hat{s}}\frac{32\pi\alpha}{x(1-x)y(1-y)}\left[\frac{(e_1-e_2)^2(1-a)}{1-\cos^2\vartheta}\right.$$
$$\left. + \frac{e_1e_2a\left[y(1-y)+x(1-x)\right]}{a^2-b^2\cos^2\vartheta} + \frac{(e_1^2-e_2^2)(x-y)}{2}\right] \tag{53}$$

where $a, b = (1-x)(1-y) \pm xy$. The subscripts refer to photon helicities; e_1, e_2 are the quark charges and ϑ is the c.m. scattering angle.

The normalization of the quark distribution amplitude Φ is fixed by a sum rule

$$\int_0^1 dx\Phi_M(x,p_T) = \frac{f_M}{\sqrt{3}} \tag{54}$$

in the case of mesons; f_M is the leptonic decay constant of M. The form of Φ_M is fixed for $p_T \to \infty$ by the asymptotic solution of an evolution equation, $\Phi_M(x, p_T \to \infty) \to \sqrt{3}f_M x(1-x)$. At medium energies, the wave function must be computed by means of non-perturbative QCD methods. While lattice computations of the wave functions are steadily progressing [197], the exploitation of ITEP sum rules is well matured, resulting in the unexpected form [198]

$$\Phi_M^{CZ}(x,p_T) \approx 5\sqrt{3}f_M x(1-x)(2x-1)^2. \tag{55}$$

This wave function corresponds to an asymmetric distribution of the quarks, even with a hole in the middle at $x = \frac{1}{2}$. Results are often compared with those derived from a wave function in which the constituents share the longitudinal momentum equally,

$$\Phi_M^{WB}(x,p_T) = \frac{f_M}{2\sqrt{3}}\delta(x-\frac{1}{2}) \tag{56}$$

physically reminiscent of a weak-binding approximation. For baryons the distributions have been extracted from QCD sum rules or, they are based on the weak-binding approximation, the normalization fixed by $J/\psi \to p\bar{p}$ and nucleon form factors [199].

6.2 QCD Predictions

Fundamental predictions of QCD perturbation theory are the scaling laws for wide-angle scattering amplitudes [200] (see [201] for a pioneering discussion of scaling phenomena):

$$\mathcal{M} \sim \frac{1}{p_T^{n-4}}f(\cos\vartheta) \tag{57}$$

n is the total number of quanta involved in the process. For $\gamma\gamma \to M\bar{M}$ (with two photon, two quarks and two antiquarks) $n = 6$ so that the amplitude behaves as $\mathcal{M} \sim 1/p_T^2$. Similarly we have for baryon production $n = 2+3+3 = 8$, hence $\mathcal{M} \sim 1/p_T^4$. These dimensional counting rules are slightly modified if the running of the coupling constant $\alpha_s(p_T^2)$ and the logarithmic p_T^2 evolution of the wave function are taken into account. Ignoring these logarithmic corrections the following power laws for the fall off of the cross sections at fixed angle are predicted

$$\frac{d\sigma}{dt} = \frac{1}{\hat{s}^4}\ g'(\cos\vartheta) \quad \text{for } \gamma\gamma \to M\bar{M} \tag{58}$$

$$\frac{d\sigma}{dt} = \frac{1}{\hat{s}^6}\ g''(\cos\vartheta) \quad \text{for } \gamma\gamma \to B\bar{B}. \tag{59}$$

Quantum chromodynamics is chirally invariant in the perturbative sector since the light quark masses can be neglected in short distance processes and (minimal) QCD and QED vector couplings are γ_5 invariant. As chiral invariance induces

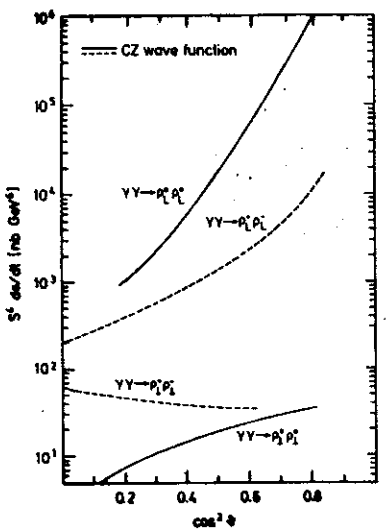

Figure 57: Cross section for wide-angle pion-pair production in $\gamma\gamma$ collisions.

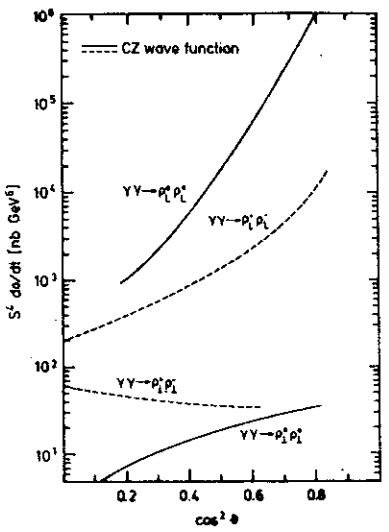

Figure 58: Cross sections for wide-angle ρ pair production in $\gamma\gamma$ collisions.

helicity conservation for massless fermionic constituents, the hadronic particles and their antiparticles are produced with opposite helicities [11].

The cross sections for $\gamma\gamma \to \pi^+\pi^-$ and $\gamma\gamma \to \pi^0\pi^0$ are presented in Fig.57 for WB and CZ wave functions. Charged pion production is practically independent of the choice of the wave function. In fact, the cross section can be expressed by the (measured) pion form factor at large s to a very high accuracy [11]

$$\frac{\frac{d\sigma}{dt}(\gamma\gamma \to \pi^+\pi^-)}{\frac{d\sigma}{dt}(\gamma\gamma \to \mu^+\mu^-)} \approx \frac{4|F_\pi(\hat{s})|^2}{1-\cos^4\vartheta}. \tag{60}$$

Measuring this ratio therefore tests the basic theoretical concept of the QCD approach, the factorization of the scattering amplitude into a short-distance part and the long-distance pion wave function. The differential cross section for neutral pion production in contrast, is strongly affected by the choice of the wave function. In the weak-binding approximation, π^0 production is isotropic while the CZ choice predicts a strong angular dependence, similar to charged pions. In any case, neutral pion production is suppressed by about one order of magnitude compared to charged pions. This is physically plausible to the extent that photon couplings to neutral systems are expected to be suppressed relative to charged systems by destructive interference effects on the constituent level.

Helicity	Process	Cross Section
$h=0$	$\gamma\gamma \to K^+K^-$	$2\frac{d\sigma}{dt}(\gamma\gamma \to \pi^+\pi^-)$
	$\gamma\gamma \to K^0\overline{K^0}$	$0.3\frac{d\sigma}{dt}(\gamma\gamma \to \pi^0\pi^0)$
	$\gamma\gamma \to \pi\eta$	$0.1(\frac{f_\eta}{f_\pi})^2\frac{d\sigma}{dt}(\gamma\gamma \to \pi^0\pi^0)$
	$\gamma\gamma \to \eta\eta$	$0.4(\frac{f_\eta}{f_\pi})^4\frac{d\sigma}{dt}(\gamma\gamma \to \pi^0\pi^0)$
	$\gamma\gamma \to \rho^0\omega$	$0.4\frac{d\sigma}{dt}(\gamma\gamma \to \rho^0\rho^0)$
	$\gamma\gamma \to \omega\omega$	$1.1\frac{d\sigma}{dt}(\gamma\gamma \to \rho^0\rho^0)$
	$\gamma\gamma \to \phi\phi$	$0.2\frac{d\sigma}{dt}(\gamma\gamma \to \rho^0\rho^0)$
$h=\pm 1$	$\gamma\gamma \to \rho^0\omega$	$0.4\frac{d\sigma}{dt}(\gamma\gamma \to \rho^0\rho^0)$
	$\gamma\gamma \to \omega\omega$	$\frac{d\sigma}{dt}(\gamma\gamma \to \rho^0\rho^0)$
	$\gamma\gamma \to \phi\phi$	$0.2\frac{d\sigma}{dt}(\gamma\gamma \to \rho^0\rho^0)$

Table 7: Relations for wide-angle high-energy cross sections of $\gamma\gamma$ annihilation into two helicity 0 (h=0) or helicity ± 1 (h=$\pm$1) mesons. $\eta-\eta'$ mixing is neglected and $f_\eta \sim f_\pi = 93\ MeV$. The ϕ is assumed to be an $s\bar{s}$ state. (From [11], modified).

The predictions for ρ pair production are shown for CZ wave functions in Fig.58. For charged ρ's and transversely polarized neutral ρ's the diagrams contributing to the scattering amplitudes are the same as those for pions. Longitudinally polarized ρ^0's, however, can be produced by diffractive diagrams through multiple gluon exchange [202]. They modify the result substantially.

Cross sections for other pseudoscalar and vector mesons are summarized in Table 7. They differ only by electric charge factors and the leptonic decay constants. In particular

$$\frac{\frac{d\sigma}{dt}(\gamma\gamma \to K^+K^-)}{\frac{d\sigma}{dt}(\gamma\gamma \to \pi^+\pi^-)} = \left(\frac{f_K}{f_\pi}\right)^2. \tag{61}$$

The flavor singlet η' requires a special analysis due to its possible gluon content in the wave function [203].

Baryon-antibaryon production differs from the meson case in several important technical points [199]. The number of diagrams grows enormously requiring computer algorithms to arrive at error free analytic results. The overall-normalization must either be derived from $J/\psi \to p\bar{p}$ or from form factor calculations. Results for various choices of wave functions have been presented in [199]. The main problem for exclusive two-photon processes involving baryons, however, comes from the steep fall-off of the cross section with energy, $d\sigma(\gamma\gamma \to B\overline{B})/dt \sim W_\gamma^{-12}$, making it very difficult to investigate the cross section experimentally in a range where asymptotic formulae can be utilized.

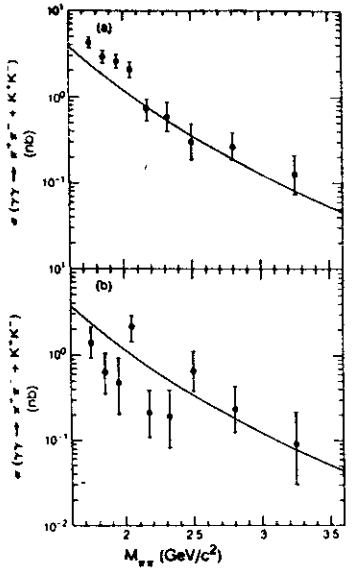

Figure 59: Comparison of $\gamma\gamma \to \pi^+\pi^- + K^+K^-$ meson pair production data [192] with the QCD prediction [11]. a) $|cos\vartheta| < 0.3$; b) $0.3 < |cos\vartheta| < 0.5$.

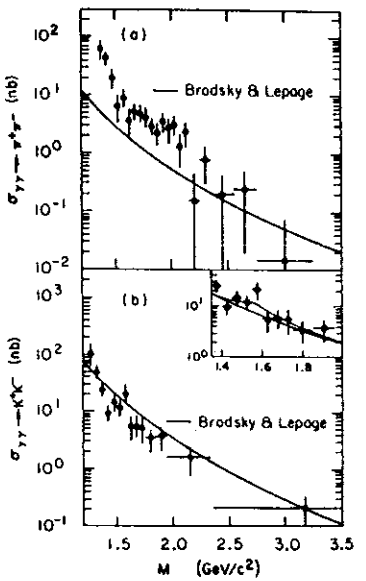

Figure 60: Comparison of (a) $\gamma\gamma \to \pi^+\pi^-$ and (b) $\gamma\gamma \to K^+K^-$ [193] meson pair production with the QCD prediction [11].

6.3 Experimental Confrontation

The MARK II Collaboration [192] and the TPC/Two-Gamma group [193] have analyzed meson production in the energy range up to ~ 3 GeV $\gamma\gamma$ energy. MARK II presented the cross section for a sample of charged hadron pairs, Fig.59, while TPC/Two-Gamma separated charged pions from kaons, Fig.60. In view of the fact that the shape of the energy dependence as well as the absolute normalization had been predicted theoretically without any adjustable parameter, the comparison with the data looks very encouraging. Nevertheless, more precise data are necessary above the resonance region at high energies to scrutinize the theoretical picture. Future experimental analyses in fact can extend the energy range up to 5 GeV [196] – beyond any doubts on the applicability of QCD perturbation theory.

Baryon production has been measured by the TASSO and JADE Collaboration [194,195], Fig.61. The energy range for $\gamma\gamma \to p\bar{p}$ is limited to ≤ 3.1 GeV leaving only about 500 MeV kinetic energy per particle in the system. Detailed

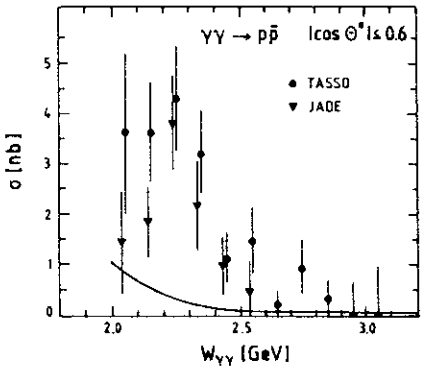

Figure 61: Cross section measurements for $\gamma\gamma \to p\bar{p}$ [194,195]. The curve is the extrapolation of a QCD calculation [199] to low energies.

comparisons with asymptotic calculations seem difficult to justify in such a case. The data are rather located in the twilight zone between threshold and asymptotia that is notoriously difficult to illuminate theoretically.

Acknowledgments

We thank our collaborators and friends for numerous discussions on the material presented in this report. In particular we are very grateful to Ch. Berger, S.J. Brodsky and T.F. Walsh.

References

[1] M. Gell-Mann, Elementary Particle Physics, Schladming, 1972.

[2] T.F. Walsh, Phys. Lett. 36B (1971) 121;
S.J. Brodsky, T. Kinoshita and H. Terazawa, Phys. Rev. Lett. 27 (1971) 280.

[3] T.F. Walsh and P. Zerwas, Phys. Lett. 44B (1973) 195;
R.L. Kingsley, Nucl. Phys. B60 (1973) 45.

[4] E. Witten, Nucl. Phys. B120 (1977) 189.

[5] I. Antoniadis and G. Grunberg, Nucl. Phys. B213 (1983) 445.

[6] W.A. Bardeen and A.J. Buras, Phys. Rev. D20 (1979) 166; D21 (1980) 2041E;
D.W. Duke and J.F. Owens, Phys. Rev. D22 (1980) 2280.

[7] N.N. Achasov, S.A. Devyanin and G.N. Shestakov, Phys. Lett. 108B (1982) 134; Z. Phys. C16 (1982) 55.

[8] J. Weinstein and M. Isgur, Phys. Rev. D27 (1983) 588.

[9] N.N. Achasov, S.A. Devyanin and G.N. Shestakov, Z. Phys. C27 (1985) 99.

[10] B.A. Li and K.F. Liu, Phys. Rev. D30 (1984) 613.

[11] S.J. Brodsky and G. Peter Lepage, Phys. Rev. D24 (1981) 1808.

[12] S.J. Brodsky, T.A. DeGrand, J.F. Gunion and J.H. Weis, Phys. Rev. D19 (1979) 1418.

[13] J.L. Rosner, Brookhaven Report CRISP 7126 (1971).

[14] F.M. Renard, Phys. Lett. 126B (1983) 59;
J.H. Kühn and P.M. Zerwas, Phys. Lett. 142B (1984) 221.

[15] TPC/Two-Gamma Coll., H. Aihara et al., Phys. Rev Lett. 57 (1986) 3245.

[16] H. Terazawa, Rev. Mod. Phys. 45 (1973) 615;
V.M. Budnev, I.F. Ginzburg, G.V. Meledin and V.G. Serbo, Phys. Rep. 15 (1975) 181;
H. Kolanoski, Two Photon Physics at e^+e^- Storage Rings, Springer Verlag, Berlin, 1984;
Ch. Berger and W. Wagner, Phys. Rep. 136 (1987) 1.

[17] F. Low, Phys. Rev. 120 (1960) 582.

[18] P. Kessler, Nuovo Cim. 17 (1960) 809

[19] J. Field, Nucl. Phys. B168 (1980) 477; B176 (1980) 545E.

[20] V.M. Budnev et al. in [16].

[21] G. Bonneau, M. Gourdin and F. Martin, Nucl.Phys. B54 (1973) 573.

[22] Ch. Berger, Proceedings of the International Conference on Experimentation at LEP (1980).

[23] PLUTO Collaboration, PETRA Proposal PRC 79/06.

[24] D. Caldwell et al., PEP Proposal 9, Proposal for PEP Forward Detector Facility (1976).

[25] H.J. Besch et al., Phys. Lett. 81B (1979) 79.

[26] A.S. Artamonov et al., Novosibirsk Preprint 84-97 (1984).

[27] A. Courau et al., Phys. Lett. 96B (1980) 402.

[28] L.D.Landau, Sov. Phys. Dok. 60 (1948) 207;
C.N. Yang, Phys. Rev. 77 (1950) 242.

[29] M. Poppe, Intern. Journ. Mod. Phys. A1 (1986) 545.

[30] S.L. Adler, Phys.Rev. 177 (1969) 2426;
J.S. Bell and L.Jackiw, Nuovo Cimento 60A (1969) 47.

[31] Y. Kitazawa, Phys. Lett. 151B (1985) 165.

[32] Particle Data Group, M. Aguilar-Benitez et al., Phys. Lett. 170B (1986) 1.

[33] S. Cooper, Note on the η Width to Two Photons, in [32].

[34] S.L. Cartwright, Proceedings of the VIth Intern. Conf. on Physics in Collision, Chicago (1986).

[35] H.W. Atherton et al., Phys. Lett. 158B (1985) 81.

[36] M.Y. Han and Y. Nambu, Phys. Rev. 139 (1965) B1006.

[37] H. Primakoff, Phys. Rev. 81 (1951) 899.

[38] C. Bemporad et al., Phys. Lett. 25B (1967) 380.

[39] A. Browman et al., Phys. Rev. Lett. 32 (1974) 1067.

[40] A. Weinstein et al., Phys. Rev. D28 (1983) 2896.

[41] JADE Coll., W. Bartel et al., Phys. Lett. 160B (1985) 421.

[42] TPC/Two-Gamma Coll., H. Aihara et al., Phys. Rev. D33 (1986) 844.

[43] D. Williams (Crystal Ball Coll.), Proceedings of the XXIII Intern. Conf. on High Energy Physics, Berkeley (1986).

[44] D.M. Binnie et al., Phys. Lett. 83B (1979) 141.

[45] G. S. Abrams et al., Phys. Rev. Lett. 43 (1979) 477.

[46] CELLO Coll., H.-J. Behrend et al., Phys. Lett. 114B (1982) 378; Phys. Lett. 125B (1983) 518.

[47] JADE Coll., W. Bartel et al., Phys. Lett. 113B (1982) 190.

[48] TASSO Coll., M. Althoff et al., Phys. Lett. 147B (1984) 487.

[49] PLUTO Coll., Ch. Berger et al., Phys. Lett. 142B (1984) 125.

[50] G. Gidal, Proceedings of the Multiparticle Conf., Kiryat-Anavim (1985).

[51] TPC/Two-Gamma Coll., H. Aihara et al., Phys. Rev. D35 (1987) 2650.

[52] A. Rittenberg, Thesis, UCRL-18863, Berkeley 1969 (unpublished).

[53] J. Field and J.E. Olsson, private communication.

[54] V.I. Telnov, private communication.

[55] W.D. Apel et al., Sov. Jour. Nucl. Phys. 30 (1979) 189.

[56] Mark III Coll., R.M. Baltrusaitis et al., Phys. Rev. D32 (1985) 2883;
A. Seiden, Proceedings of the Intern. Workshop on Photon-Photon Collisions, Paris (1986).

[57] B. Shen, Proceedings of the Intern. Workshop on Photon-Photon Collisions, Paris (1986).
[58] H. Suura, T.F. Walsh and B.-L. Young, Lett. Nuovo Cim. 4 (1972) 505.
[59] M.S. Chanowitz, Phys. Rev. Lett. 44 (1980) 59.
[60] B. Schrempp-Otto, F. Schrempp and T. Walsh, Phys. Lett. 36B (1971) 463.
[61] P. Grassberger and R. Kögerler, Nucl. Phys. B106 (1976) 451.
[62] G.M. Radutskij, Sov. Jour. Nucl. Phys. 8 (1969) 65;
B. Renner, Nucl. Phys. B30 (1971) 634;
A. Bramon and M. Greco, Lett. Nuovo Cim. 2 (1971) 522;
G. Schierholz and K. Sundermeyer, Nucl. Phys. B40 (1972) 125;
V.N. Novikov and S.I. Eidelmann, Sov. Jour. Nucl. Phys. 21 (1969) 65;
J. Babcock and J.L. Rosner, Phys. Rev. D14 (1976) 1286;
V.M. Budnev and A.E. Kaloshin, Phys. Lett. 86B (1979) 351.
[63] J. Smith, J.A.M. Vermaseren, G. Grammer, Phys. Rev. D15 (1977) 3280;
J.A.M. Vermaseren, Program write-up, unpublished.;
F.A. Berends, P.H. Daverfeldt and R. Kleiss, Nucl. Phys. B253 (1985) 441.
[64] G. Mennessier, Z. Phys. C16 (1983) 241.
[65] PLUTO Coll., Ch. Berger et al., Phys. Lett. 94B (1980) 254.
[66] Mark II Coll., A. Roussarie et al., Phys. Lett. 105B (1981) 304.
[67] TASSO Coll., R. Brandelik et al., Z. Phys. C10 (1981) 117.
[68] Crystal Ball Coll., C. Edwards et al., Phys. Lett. 110B (1982) 82.
[69] CELLO Coll., H.-J. Behrend et al., Z. Phys. C23 (1984) 223.
[70] DELCO Coll., A. Courau et al., Phys. Lett. 147B (1984) 227.
[71] Mark II Coll., J.R. Smith et al., Phys. Rev. D30 (1984) 851.
[72] PLUTO Coll., Ch. Berger et al., Z. Phys. C26 (1984) 199.
[73] TPC/Two-Gamma Coll., H. Aihara et al., Phys. Rev. Lett. 57 (1986) 404.
[74] J.E. Olsson, Proceedings of the $\gamma\gamma$ Workshop, Aachen (1983).
[75] G. Köpp, T. Walsh and P. Zerwas, Nucl. Phys. B70 (1974) 461.
[76] H. Krasemann and J.A.M. Vermaseren, Nucl. Phys. B184 (1981) 269.
[77] Crystal Ball (SPEAR) Coll., C. Edwards et al., Phys. Lett. 110B (1982) 82.
[78] PLUTO Coll., Ch. Berger et al., Phys. Lett. 149B (1984) 427.
[79] Crystal Ball (DORIS) Coll., D. Antreasyan et al., Phys. Rev. D33 (1986) 1847.
[80] TASSO Coll., M. Althoff et al., Z. Phys. C31 (1986) 537.
[81] TASSO Coll., M. Althoff et al., Phys. Lett. 121B (1983) 216.
[82] D. Faiman, H.J. Lipkin and H.R. Rubinstein, Phys. Lett. 59B (1975) 269
[83] R. Johnson, Thesis, SLAC-Report 294 (unpublished).
[84] G. Gidal, Proceedings of the Intern. Workshop on Photon-Photon Collisions, Paris (1986).

[85] P. Singer, Phys. Lett. 124B (1983) 531.
[86] A. Bramon and M. Greco, Lett. Nuovo Cim.2 (1971) 522;
S.B. Berger and B.T. Feld, Phys. Rev. D8 (1973) 3875;
J. Babcock and J.L. Rosner, Phys. Rev. D14 (1976) 1286;
G.K. Greenhut and G.W. Intemann, Phys. Rev. D18 (1978) 231;
V.M. Budnev and A.E. Kaloshin, Phys. Lett. 86B (1979) 351.
[87] T. Barnes, Proceedings of the Intern. Workshop on Photon-Photon Collisions, Paris (1986).
[88] TASSO Coll., M. Althoff et al., Z. Phys. C29 (1985) 189.
[89] S.M. Flatté, Phys. Lett. 63B (1976) 224.
[90] A. Courau et al., Nucl. Phys. B271 (1986) 1.
[91] Z. Ajaltouni et al., Paper contributed to the Int. Symposium on Lepton Photon Interaction, Kyoto, 1985.
[92] G. Mennessier and Tran N. Truong, Phys. Lett. 177B (1986) 195;
D. Morgan and M.R. Pennington, Preprint RAL-87-020
[93] S.B. Berger and B.T. Field, Phys. Rev. D8 (1973) 3875.
[94] V.M. Budnev and A.E. Kaloshin, Phys. Lett. 86B (1979) 351.
[95] T. Barnes, Phys.Lett. 165B (1985) 434.
[96] PLUTO Coll., Ch. Berger et al., Phys. Lett. 167B (1986) 120.
[97] Mark III Coll., R.M. Baltrusaitis et al., Phys. Rev. D33 (1986) 629.
[98] J.E. Gaiser et al., Phys. Rev. D34 (1986) 711.
[99] S. Cooper, Proceedings of the XXIII Intern. Conf. on High Energy Physics, Berkeley (1986).
[100] R704 Coll., C. Baglin et al., Phys. Lett. 187B (1987) 191.
[101] MD1 Coll., A.E. Blinov et al., Novosibirsk preprint 86-107 (1986).
[102] M.A. Shifman, A.I. Vainshtein, M.B. Voloshin and V.I. Zakharov, Phys. Lett. 77B (1978) 80;
R. Kirschner and A. Schiller, Z. Phys. C16 (1982) 141;
T.M. Aliev, Yad. Fiz. 37 (1983) 403.
[103] L.J. Reinders, H.R. Rubinstein and S. Yazaki, Phys. Lett. 113B (1982) 411.
[104] R.A. Lee, Thesis Stanford University; SLAC-282 UC-34D (1985).
[105] K. Wacker, Proceedings of the XVIIIth Recontre de Moriond, La Plagne, France, March 13-19, 1983.
[106] D.L Burke, Proceedings of the XXIst Intern. Conference on High Energy Physics, Paris, 1982.
[107] TPC/Two-Gamma Coll., H. Aihara et al., Phys. Rev. Lett. 57 (1986) 51.
[108] TPC/Two-Gamma Coll., H. Aihara et al., Phys. Rev. Lett. 57 (1986) 2500.
[109] Mark II Coll., G. Gidal et al., preprint LBL-22691 (1987).
[110] F.M. Renard, Nuovo Cim. 80A (1984) 1.

[111] J.-E. Olsson, talk given at the Int. Symposium on Lepton and Photon Interactions, Hamburg(1987);
Mark II Coll., G. Gidal et al., preprint LBL-22960 (1987).
[112] TASSO Coll., M. Althoff et al., Phys. Lett. 97B (1980) 488.
[113] D.L. Burke et al., Phys. Lett. 103B (1981) 153.
[114] TASSO Coll., M. Althoff et al., Z. Phys. C16 (1982) 13.
[115] CELLO Coll., H.-J. Behrend et al., Z. Phys. C21 (1984) 205.
[116] TPC/Two-Gamma Coll., J.G. Layter et al., contribution to the Intern. Conf. on High Energy Physics, Leipzig (1984).
[117] H.Kolanoski, Proceedings of the $\gamma\gamma$ -Workshop, Aachen, 1983.
[118] S.J. Brodsky, G. Köpp and P.M. Zerwas, Phys. Rev. Lett. 58 (1987) 443.
[119] R.L. Jaffe, Phys. Rev. D15 (1977) 267 abd 281;
R.L. Jaffe and K. Johnson, Phys. Lett 60B (1976) 201.
[120] ARGUS Coll., H. Albrecht et al., DESY 87-048 (1987).
[121] G. Alexander, U. Maor and P.G. Williams, Phys. Rev. D26 (1982) 1198.
[122] G. Alexander, A. Levy and U. Maor, Z. Phys. C30 (1986) 65.
[123] TPC/Two-Gamma Coll., H. Aihara et al., Phys. Rev. Lett. 54 (1985) 2564;
TASSO Coll., M. Althoff et al., Z. Phys. C32 (1986) 11.
[124] A. Nilsson (ARGUS Coll.), presented at of the Intern. Europhysics Conf. on High Energy Physics, Uppsala (1987).
[125] N.N. Achasov, V.A. Karnakov and G.N. Shestakov, Novosibirsk preprint TPh-No 7(151), 1987.
[126] J.J. Sakurai and D. Schildknecht, Phys. Lett. 40B (1972) 121.
[127] I.F. Ginzburg and V.G. Serbo, Phys. Lett. 109B (1982) 231.
[128] D. Bintinger et al., Phys. Rev. Lett. 54 (1985) 763.
[129] PLUTO Coll., Ch. Berger et al., Phys. Lett. 149B (1984) 421.
[130] A.E. Blinov et al., Novosibirsk preprint 85-95.
[131] G. Alexander, U. Maor and C. Milstene, Phys. Lett. 131B (1983) 224.
[132] A. Levy, Phys. Lett. 177B (1986) 106.
[133] PLUTO Coll., Ch. Berger et al., Z. Phys. C26 (1984) 353.
[134] E. Etim and E. Masso, Z. Phys. C18 (1983) 117.
[135] U. Maor and E. Gotsman, Phys. Rev. D28 (1983) 2149.
[136] G. Knies, Proceedings of the $\gamma\gamma$ Workshop, Lake Tahoe (1984).
[137] PLUTO Coll., Ch. Berger et al., Phys. Lett. 107B (1981) 168.
[138] C.H. Llewellyn Smith, Phys. Lett. 79B (1978) 83;
W.R. Frazer and J.F. Gunion, Phys. Rev. D20 (1979) 147;
R.J. DeWitt et al., Phys. Rev. D19 (1979) 2046.
[139] C. Peterson, T.F. Walsh and P. Zerwas, Nucl. Phys. B147 (1980) 424.

[140] C. Peterson, T.F. Walsh and P. Zerwas, Nucl. Phys. B229 (1983) 445.
[141] T. Uematsu and T.F. Walsh, Nucl. Phys. B199 (1982) 93.
[142] G. Rossi, Phys. Rev. D29 (1984) 852.
[143] M. Glück and E. Reya, Phys. Rev. D28 (1983) 2743);
M. Drees, M. Glück, K. Grassi and E. Reya, Z. Phys. C27 (1985) 587.
[144] J.H. Field, F. Kapusta and L. Poggioli, Phys. Lett. 181B (1986) 362.
[145] P. Zerwas, Phys. Rev. D10 (1974) 1485.
[146] P. Zerwas, Proceedings of the Int. Symposium on Multiparticle Dynamics, Lund (1984).
[147] J. Badier et al., Z. Phys. C18 (1983) 281.
[148] W. Wagner, Habilitation Thesis, RTWH Aachen (1983).
[149] C.T. Hill and G.G. Ross, Nucl. Phys. B148 (1979) 373.
[150] A. Cordier and P. Zerwas, Proceedings of the ECFA LEP200 Workshop, Aachen (1986).
[151] I. Antoniadis and L. Marleau, Phys. Lett. 161B (1985) 163;
I. Antoniadis and L. Marleau, Proceedings of the High Energy Physics Conference, Berkeley (1986).
[152] PLUTO Coll., Ch. Berger et al., Phys. Lett. 142B (1984) 111.
[153] JADE Coll., W. Bartel et al., Z. Phys. C24 (1984) 231.
[154] TASSO Coll., M. Althoff et al., Z. Phys. C31 (1986) 527.
[155] PLUTO Coll., Ch. Berger et al., Nucl. Phys. B281 (1987) 365.
[156] TPC/Two-Gamma Coll., H. Aihara et al., Phys. Rev. Lett. 58 (1987) 97;
TPC/Two-Gamma Coll., H. Aihara et al., Z. Phys. C34 (1987) 1.
[157] CELLO Coll., H.-J. Behrend et al., Phys. Lett. 126B (1983) 391.
[158] V. Blobel, DESY Report 84-118 and Proceedings of the CERN Comp. School (1984).
[159] Ch. Berger and W. Wagner, in [16].
[160] W. Wagner, Proceedings of the XXIII Intern. Conf. on High Energy Physics, Berkeley (1986).
[161] F. Sciulli, Proceedings of the Int. Symposium on Lepton and Photon Interactions, Kyoto (1985).
[162] R.D. Schamburger et al., Phys. Lett. 138B (1984) 225.
[163] S.M. Berman, J.D. Bjorken and J.B. Kogut, Phys. Rev. D4 (1971) 3388.
[164] TASSO Coll., R. Brandelik et al., Phys. Lett. 107B (1981) 1290.
[165] G. Giacomelli and M. Jacob, Phys. Rep. 55 (1979) 1.
[166] K. Kajantie and R. Raitio, Nucl. Phys. B159 (1979) 528;
K. Kajantie, Phys. Scripta 29 (1979) 230;
Acta Phys. Austr. Suppl.XXI (1979) 663.
[167] C.H. Llewellyn Smith, Phys. Lett. 79B (1978) 83.

[168] J. Stirling, Proceedings of the $\gamma\gamma$ Workshop, Aachen (1983).
[169] K. Kajantie, Proceedings of the $\gamma\gamma$ Workshop, Paris (1981).
[170] P. Aurenche et al., Z. Phys. C29 (1985) 423.
[171] F.A. Behrends, Z. Kunszt and R. Gastmans, Phys. Lett. 92B (1980) 186; DESY 80-89 (1980).
[172] I. Kang, Oxford preprint 50/82 (1982).
[173] F. Khalafi, P.V. Landshoff and W.J. Stirling, Phys. Lett. 130B (1983) 215.
[174] PLUTO Coll., Ch. Berger et al., Z. Phys. C26 (1984) 191.
[175] H.J. Daum, H. Meyer and J. Bürger, Z. Phys. C8 (1981) 167.
[176] J. Dorfan, Z. Phys. C7 (1981) 349.
[177] JADE Coll., W. Bartel et al., Phys. Lett. 107B (1981) 163.
[178] T. Jayaraman et al., Phys. Lett. 119B (1982) 215;
R.M. Godbole et al., Phys. Lett. 142B (1984) 91.
[179] M.Y. Han and Y. Nambu, Phys. Rev. 139 (1965) B1006.
[180] J.C. Pati and A. Salam, Phys. Rev. D8 (1973) 1240;
Phys. Rev. Lett. 36 (1976) 355.
[181] TASSO Coll., M. Althoff et al., Phys. Lett. 138B (1984) 219.
[182] PLUTO Coll., Ch. Berger et al., Z. Phys. C29 (1985) 499; Z. Phys. C33 (1987) 351.
[183] CELLO Coll., H.-J. Behrend et al., reported by H. Kolanoski, Proceedings of the International Conf. on High Energy Physics, Leipzig (1984).
[184] H. Kolanoski, Proceedings of the Intern. Symposium on Lepton-Photon Interactions Kyotò, 1985.
[185] NA14 Coll., P. Astbury et al., Phys. Lett. 152B (1985) 419;
R806 Coll., C. Kourkoumelis et al., Z. Phys. C16 (1982) 101.
[186] R.D. Field and R.P. Feynman, Nucl. Phys. B137 (1978) 1.
[187] TPC/Two-Gamma Coll., Paper contributed to the Intern. Symposium on Lepton-Photon Interactions 1985, Kyoto, see [184].
[188] D. Aston et al., Phys. Lett. 94B (1980) 113;
J.J. Aubert et al., Nucl. Phys. B213 (1983) 31.
[189] JADE Coll., W. Bartel et al., Phys. Lett. 184B (1987) 288.
[190] G.J. Feldman et al., Phys. Rev. Lett. 38 (1977) 1313.
[191] G. Gidal, Proceedings of the $\gamma\gamma$ Workshop, Paris (1986).
[192] J. Boyer et al., Phys. Rev. Lett. 56 (1986) 207.
[193] TPC/Two-Gamma Coll., H. Aihara et al., Phys. Rev. Lett. 57 (1986) 51
[194] TASSO Coll., R. Brandelik et al., Phys. Lett. 108B (1982) 67;
TASSO Coll., M. Althoff et al., Phys. Lett. 130B (1983) 449;
TASSO Coll., M. Althoff et al., Phys. Lett. 142B (1984) 135.
[195] JADE Coll., W. Bartel et al., Phys. Lett. 174B (1986) 350.

[196] S.J. Brodsky, F. Erne, P.H. Damgaard and P. Zerwas, Proceedings of the ECFA LEP200 Workshop, Aachen (1986).
[197] G. Martinelli and C.T. Sachrajda, Phys. Lett. 190B (1987) 151.
[198] V.L. Chernyak and I.R. Zhitnitsky, Phys. Rep. 112 (1984) 173.
[199] G.R. Farrar, E. Maina and F. Neri, Nucl. Phys. B259 (1985) 702;
J.F. Gunion, D. Millers and K. Sparks, Phys. Rev. D33 (1983) 689;
D. Millers and J.F. Gunion, Phys. Rev. D34 (1986) 2657.
[200] S.J. Brodsky and G.R. Farrar, Phys. Rev. Lett. 31 (1973) 1153;
Phys. Rev. D11 (1975) 1309;
V.A. Matveev, R.M. Muradyan and A.V. Tavkhelidze, Lett. Nuovo Cim. 7 (1973) 719.
[201] H.A. Kastrup, Nucl. Phys. 58 (1964) 561.
[202] V.L. Chernyak and I.R. Zhitnitsky, Nucl. Phys. B222 (1983) 382.
[203] G.W. Atkinson, J. Sucher and K. Tsokos, Phys. Lett. 137B (1984) 407.